Rational Nanocarbon Composites for Novel Sensing and Catalysis

by

David Linn White

B. S., Millersville University, 2015

Submitted to the Graduate Faculty of the

Dietrich School of Arts and Sciences in partial fulfillment

of the requirements for the degree of

Doctor of Philosophy

University of Pittsburgh

2020

UNIVERSITY OF PITTSBURGH

DIETRICH SCHOOL OF ARTS AND SCIENCES

This dissertation was presented

by

David Linn White

It was defended on

October 15, 2020

and approved by

Dr. Jill Millstone, Associate Professor, Department of Chemistry

Dr. Haitao Liu, Associate Professor, Department of Chemistry

Dr. Hong Koo Kim, Professor, Department of Electrical and Computer Engineering

Dissertation Director: Dr. Alexander Star, Professor, Department of Chemistry

Rational Nanocarbon Composites for Novel Sensing and Catalysis

David Linn White, PhD

University of Pittsburgh, 2020

Carbon nanomaterials have extraordinary electrical properties due to their covalent structure which enable a wide range of sensing and catalytic applications. While these structures are impressive on their own, combinations with other materials enable broader extensions of properties and applications. Most functionalization schemes to form composite materials to this date have resulted in degradation of the excellent physical properties. Careful introduction of defects or composite formation is a potential route to avoid loss of outstanding electrical properties and enable a wide range of nanomaterial composites. We first investigated how covalent organic frameworks can be used as a templating strategy to control oxidation while retaining sp^2 conjugation to make holey graphene from single layer graphene. Holey graphene can then be used as a substrate for formation of size-controlled gold and palladium nanoparticles without reducing agent. Composite holey graphene nanoparticle materials exhibit strong electronic coupling between the individual nanomaterials and were leveraged to perform sensing of hydrogen sulfide and hydrogen gases for gold and palladium-based composites, respectively. This covalent organic framework template strategy can be further extended into formation of bulk holey graphene through patterning many graphene sheets at once on highly ordered pyrolytic graphite (HOPG). Once exfoliated, many solution phase reactions with metal salts were explored but silver, gold, copper, and nickel were all shown to form size-controlled nanoparticles in aqueous solution in a concentration dependent manner. So-called graphene nanoparticle compounds showed strong electronic coupling between constituent nanoparticles and nickel-based compounds showed promising activity for oxygen evolution reaction reaching mass current activities of 10,000 mA/mg of Ni at 1.7 V versus reversible hydrogen electrode. The final project leveraged growth mechanics of porous frameworks with nanocarbon materials to combine a copper catecholate based metal organic framework (MOF) grown on single-walled carbon nanotubes (SWCNTs). These composites were used to facilitate a liquid-based field-effect transistor (FET) sensing modality where ionic strength and migration of ions into pores in the presence of homologous series of carbohydrates altered observed current leading to a size selective sensor. The results of this report illustrate how careful control of nanomaterial interfaces can be leveraged for novel sensing and catalysis.

Table of Contents

List of Tables

List of Figures

Preface

I would like to express my deepest appreciation to my research advisor, Professor Alexander Star. His mentorship has enabled me to develop into a robust independent scientist who is capable of building multiple lines of inquiry at once. His scientific insight often pushed me to discover deep intuitions about the physical systems I was studying. The training I received greatly improved my writing, clear scientific communication as well as my appreciation of the political economy of science.

I would additionally like to express gratitude to my committee members Professor Haitao Liu, Professor Jill Millstone, and Professor Hong Koo Kim. The discussions I have had with each committee member made the research I performed more rigorous. Addressing their specific expertise made my research much richer and clearer.

I would like to thank all current and former members of the Star Lab during my time there. Your help in group meetings and discussions is of tremendous value to me. I would like to thank Dr. Seth Burkert for being a true friend and helpful discussion partner to bounce ideas off of. Sean Hwang was also immensely helpful for discussions and being a friend outside of lab to take a break from research. Dr. James Ellis brought a unique viewpoint to discussions which was sorely missed after he graduated. I would also like to thank Phillip Fournier, Greg Morgan, and Michael Chido for being my friends early on in my graduate career. Additionally, I would like to thank Gordon Chiu, James Gaugler, Wanji Seo, Guilherme de Oliveria Silva, Wenting Shao, Long Bian, Xiaoyun He, Zidao Zeng, Zhengru Liu and Christian Gamboa for being pleasant officemates and great colleagues.

I would also like to thank the University of Pittsburgh and the National Science Foundation, for financial support during my studies.

1.0 Introduction

Human development in the past century has first and foremost been pushed forward by the rise of exponential technologies. The necessary characteristic of these technologies is the ability for further developments in the technology to enable better tools to develop the technological frontier. Semiconductor manufacturing takes on this character as most clearly exemplified by Moore's Law.[1] The ability to make circuits denser allows for the computational power to design denser circuits. Nanoscience and technology also take on this characteristic. Development of specific nanostructures can be used to implement new nanostructures.[2] As the length scale of given physical system has a strong effect on the properties of that system, the ability to construct systems across very small scales will open new frontiers of scientific development and ultimately human development.

Nanoscopic phenomena are those which take place on a length scale between 1 and 100 nanometers, where nanometers constitute a billionth of a meter. This length scale reduction drastically increases the ratio of surface to bulk atoms present in each physical system. Surface atoms present in materials are inherently less stable (conversely more reactive) than atoms present in the bulk due to relatively unsatisfied chemical environments.[3, 4] Control over length scale therefore represents tunability in the physical system reactivity which leads to a series of novel physical phenomena not observed in either bulk or atomic length scales.[5-8] Particularly, the tunability[9] in the electronic orbital structure[10] and electronic transport[11] through composites of different materials offers a novel arena to develop new understanding and technologies which can address forthcoming challenges for the human species.

Development of novel electronic devices and nanomaterial interfaces can in particular be used for tunable interactions with molecular systems. In particular, rational modification of existing nanomaterials through synthesis can yield altogether new behavior. One set of cases will focus on using patterning to generate translationally invariant defects to enable band structure manipulations. Another case is focused on using nanomaterials as structure directing agents to facilitate a composite material which synergizes with the structure directing agent to form a wholly new conductive material.

1.1 Graphitic Nanomaterials

Graphitic nanomaterials represent a broad class of carbon allotropes distinguished for their sp^2 bonding character.[12] Nanomaterials are typically categorized according to the remaining length scales which belong in bulk scale, i.e., nanotubes are considered one dimensional due to their longitudinal axis typically being of bulk dimension. Typical representatives of graphitic nanomaterials include fullerenes,[13] carbon nanotubes,[14] and graphene[15] as zero, one, and two dimensional nanomaterials as shown in Figure 1.1. Graphitic nanomaterials are prized for a variety of physical properties imparted by their covalent bonding character including mechanical strength[16, 17] and superior electrical conductivity.[18-20] Electrical conductivity is a particularly important property for the contents of this dissertation and as a central focus of the research laid out here the discussion of graphitic materials will be limited to one- and two-dimensional variants namely carbon nanotubes and graphene.

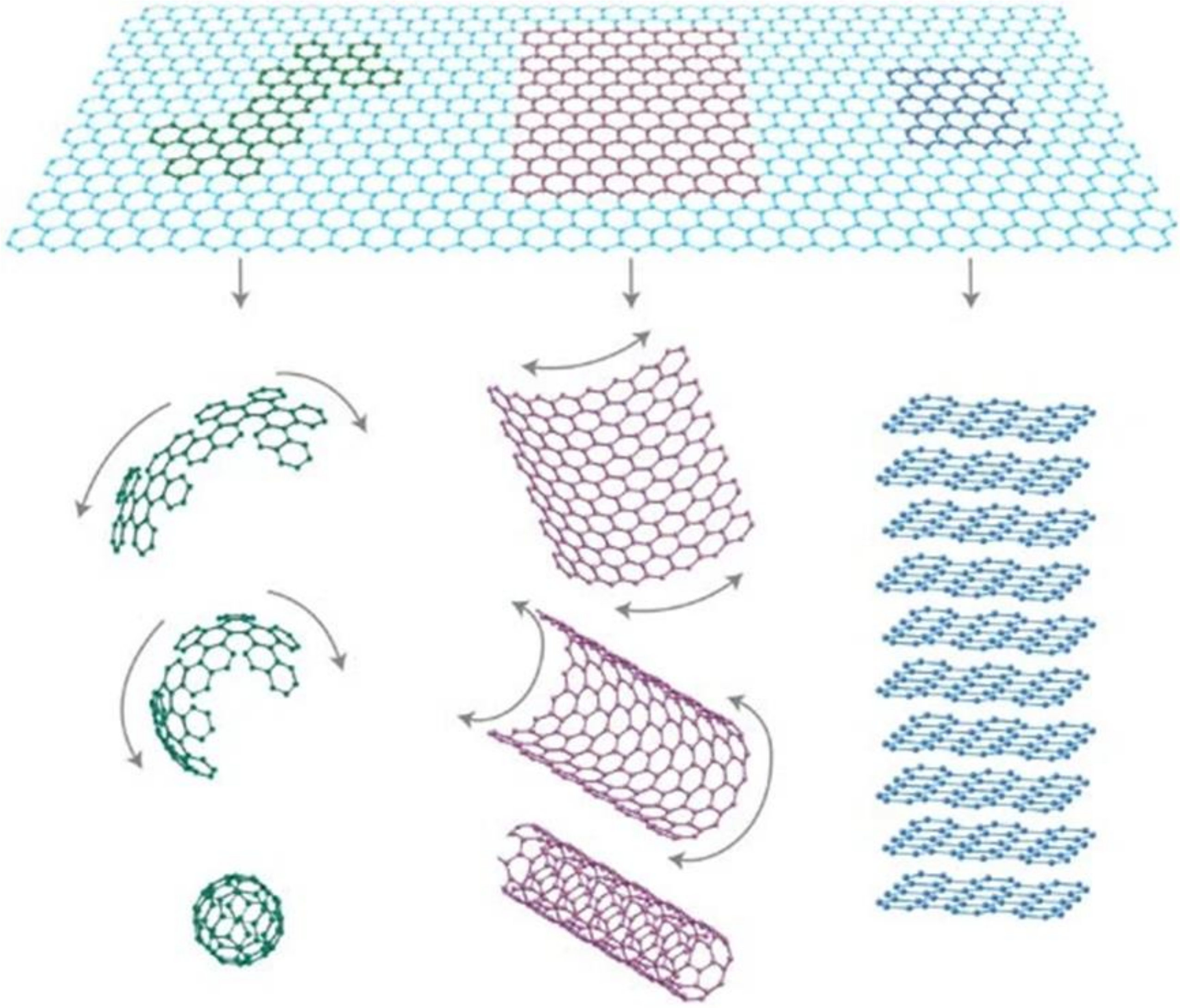

Figure 1.1 Examples of different graphitic nanomaterials including fullerenes (green), single-walled carbon nanotubes (purple) and graphene (light blue). Reprinted with permission from reference. [21] Copyright 2007 Springer Nature

Discussions of graphitic nanomaterials electronic properties are typically conducted by examining the band structure of graphene.[22] Band structures can be considered as the infinite translational extension of molecular orbitals through a symmetry matching condition in the wavefunction.[23] In particular, the relevant molecular orbitals to address are the p_z orbitals which lie above and below the plane of graphene. As these orbitals are all the same character, consideration of their overlap as phase is varied leads to the formation of semimetallic (zero band gap) Dirac cone physics in the first Brillouin zone at the K points. The relevant consideration of the Dirac cone structure is the massless dispersion that the band structure takes near the cone. This massless dispersion is identified by the linear relation between energy and electron momentum near the fermi level. Additionally, the relatively low density of states enables facile doping of the energy through changes in local chemical potential. This brings considerable promise for graphene both in terms of high electron mobility as well as manipulation of the band structure for novel composite formation.

Carbon nanotubes electronic structure can also be formulated through this Dirac cone construction but by imposing additional symmetry conditions which are typically formulated as a chiral vector drawn on top of a graphene sheet as seen in Figure 1.2.[24] The chiral vector, composed of two basis vectors n and m, describes how the nanotube must be rolled up to preserve translational symmetry around the circumference. Imposition of this symmetry condition leads to cutting of Dirac cone into individual sections some of which are metallic while others are semiconducting. Consideration of this wrapping leads to the conclusion that statistically single-walled carbon nanotubes will be 1/3 metallic and 2/3 semiconducting.[25]

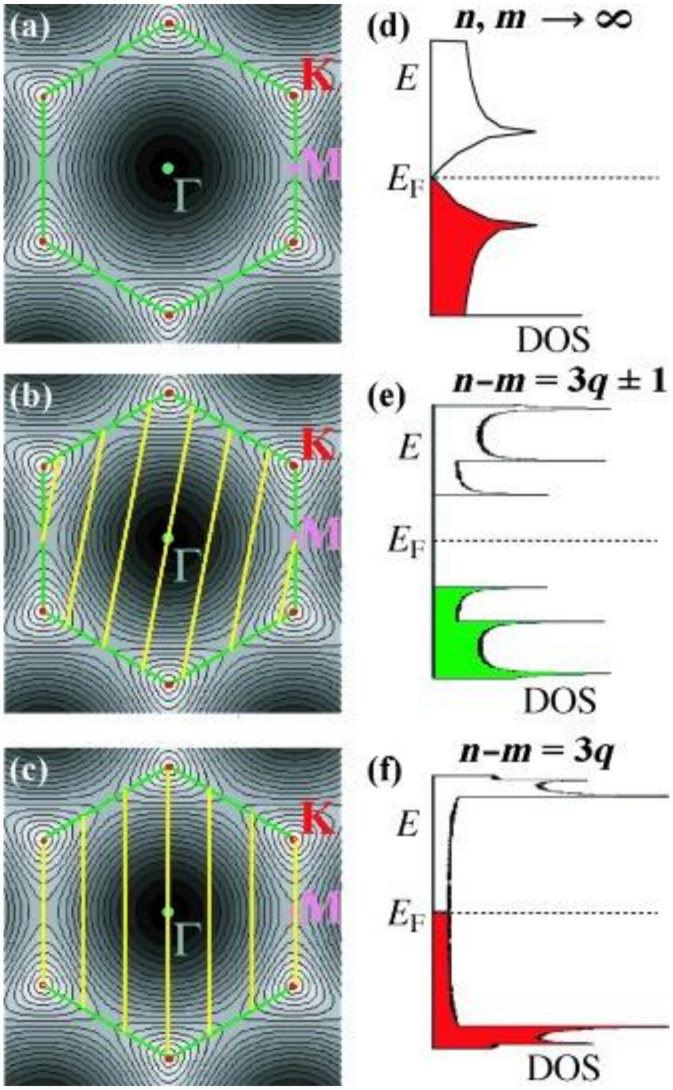

Figure 1.2 Illustrations of band structures and density of states for graphene (top), semiconducting carbon nanotubes (middle), and metallic nanotubes (bottom). N and M criteria refer the basis vectors for the chiral vector. Reprinted with permission from reference.[24] Copyright © 2004 WILEY-VCH Verlag GmbH & Co. KGaA, Weinheim

Both carbon nanotubes and graphene are of interest for sensors due to the all surface nature of their construction. The ability of the surface atoms' chemical potential to be modulated by analytes, which can subsequently be read out as changes in conductance make these materials a powerful platform technology. The wealth of chemistry[26, 27] to modify these structures to enhance the selectivity for particular analytes and improve the sensitivity at lower concentrations is a considerable boon over existing technologies.

Growth of graphitic nanomaterials has typically been conducted through multiple avenues with different relative tradeoffs. Earliest reports of graphene were achieved with mechanical exfoliation via the “scotch tape” method.[15] The primary disadvantage of mechanical exfoliation is the limited control over the achieved lateral size of the resulting single layer sheet and relatively low throughput to achieve large scale quantities of graphene. Advantages of this methodology include the ease of achieving a nanomaterial and the high quality of the resulting graphene dependent on the starting material. In the interest of developing a more scalable methodology, chemical vapor deposition (CVD) was harnessed to achieve larger scale growth of graphene on top of metallic films.[28] Copper, nickel, and their alloys are the most common metals used to facilitate hydrocarbon decomposition to yield the sp^2 carbon lattice. Parameters have been well tuned to achieve centimeter area sized single crystals of graphene recently.[29]

Another primary method to achieve larger scale graphene in solution has been the development of wet chemical oxidation to yield graphene oxide from bulk graphite. The most popular method has been the oxidation of graphite through Hummer’s method, which entails exposure to potassium permanganate and sulfuric acid.[30] This yields a soluble graphene but one which is riddled with oxygenate defects. There have been several improvements to these methods to limit the extent of degradation[31] but the inherent nature of the wet chemical process will induce random defects which destroy the honeycomb lattice and heterogeneously alter the electronic properties. Typical efforts to induce improved electrical properties have utilized reduction via hydrazine or thermal annealing.[32] Achieving controlled oxidation of graphene through non-random defects is one of the central aims of this work.

1.2 Covalent Organic Frameworks

Covalent organic frameworks (COFs) are considered as an extension of organic chemistry from chemical reactions that form small molecules to ones that form polymeric materials.[33, 34] COFs are defined as porous materials with long range order linked through molecular covalent linkages. Induction of this structure is achieved through condensation reactions with well-defined symmetry and rigidity. There are a variety of porous structures that a given covalent organic framework can take on depending on the individual constituents of the framework. Control of the resulting structure can be reliably predicted from the individual linkers which is a hallmark of these systems as demonstrated in Figure 1.3. While both 3-D[35] and 2-D[36] topologies have been formed, this work will primary focus on 2-D structures.

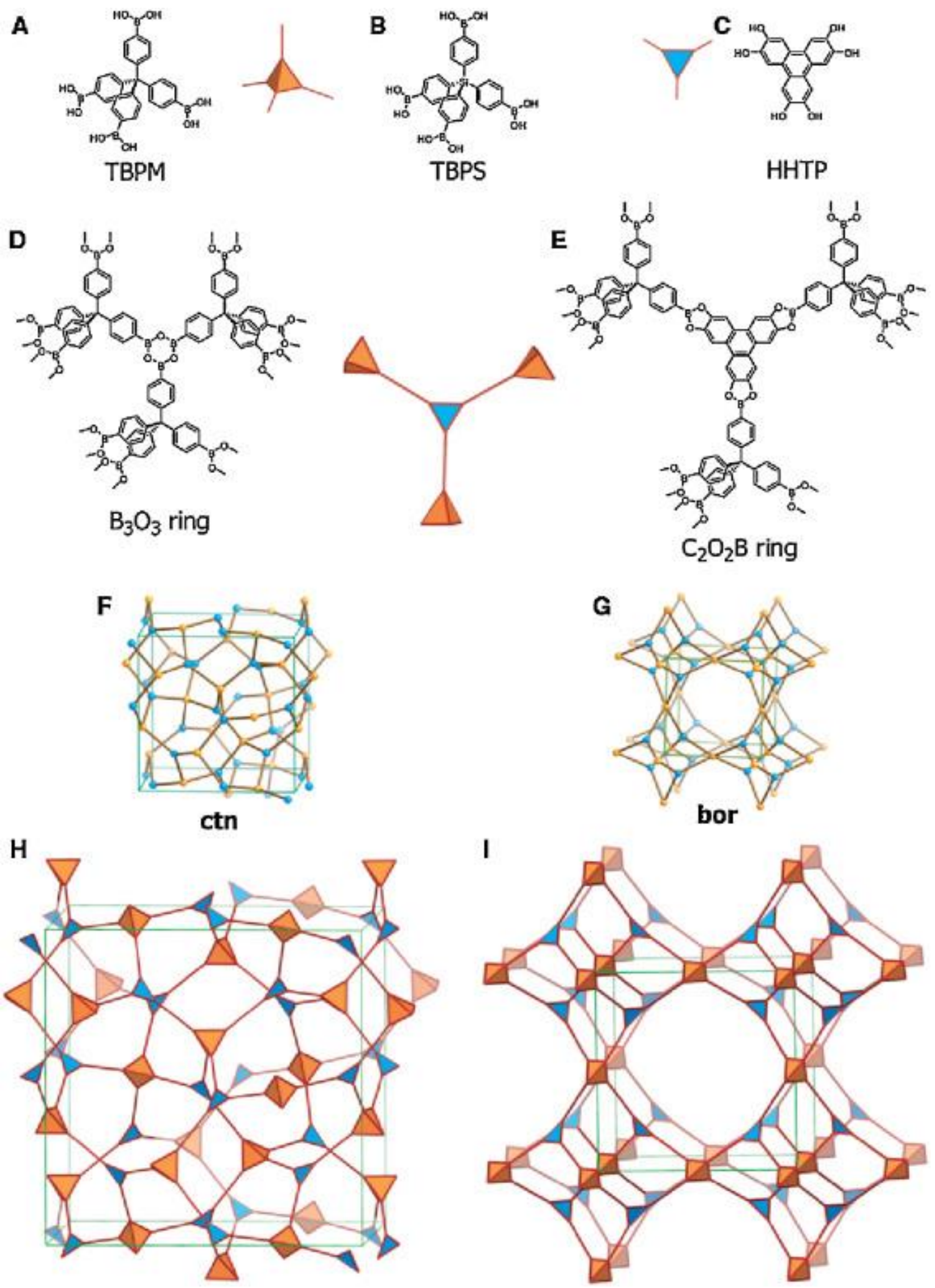

Figure 1.3 Scheme illustrating different covalent linkages leading to two different three dimensional topologies. Reprinted with permission from reference.[37] Copyright 2016 Elsevier

COFs are typically formed using dynamic reversible covalent bonding between rigid linkers to generate an overall crystalline porous structure.[38] Although this has been the primary strategy to date, there have been several recent reports of irreversible bond formation being used to form COFs.[39, 40] The reversibility of the bonding has tended to be important to enable crystal structures to heal from local energetic minima in bonding configuration to a more global energetic thermodynamic minimum, i.e., crystalline structure as opposed to a kinetically preferable structure. A variety of bonding chemistries have been developed including boroxine,[41] boronate ester,[42] Schiff base imines,[43] triazine,[44] and many more. The dynamic nature of the bonding has led to instability of the crystalline structure in response to different chemical environments, such as humidity, acid, base, and other organic solvent systems.[45] In general, more dynamic linkages tend to form larger crystalline domains and vice versa. In general, nucleation and growth dynamics for COFs are often different, some depend on pi-pi stacking to promote larger growth while others are dependent on catalytic reaction conditions to promote growth.[46]

This work is focused on the use of COF-5 which is a boronate ester-based COF with linkages between a ditopic boronic acid-based benzene unit with a tritopic catecholate unit to form an overall 2-D hexagonal morphology with 1-D channel dimensions of 2.7 nm as shown in Figure 1.4. Previous work has shown in response to heterogeneous growth environments, i.e., graphene, COF-5 orients normal with respect to the pi-surface to generate a thin film morphology[47] in contrast to typically insoluble randomly oriented microcrystalline domains homogeneously formed in solvothermal environments.

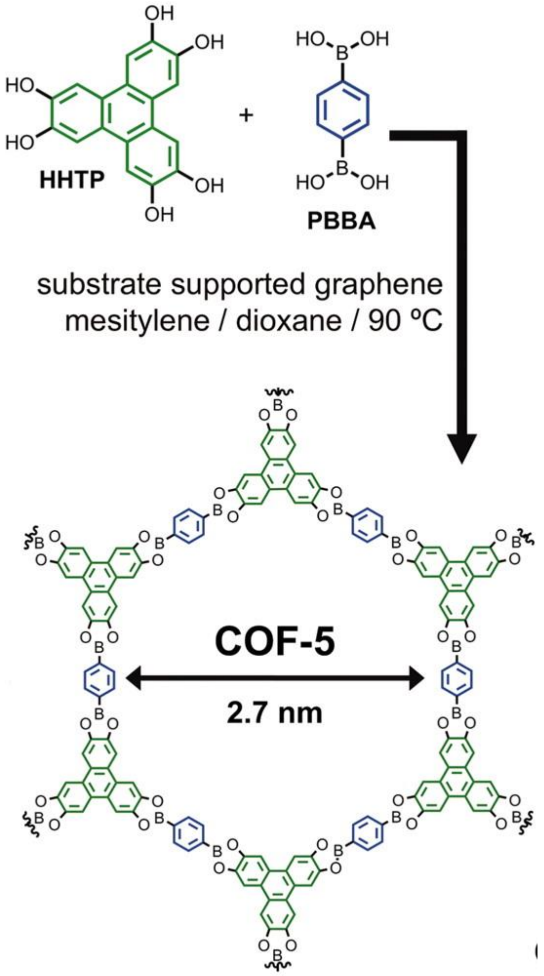

Figure 1.4 Chemical structure of COF-5 and synthetic conditions for growth. Reprinted (adapted) with permission from reference.[47] Copyright © 2011, American Association for the Advancement of Science

Applications of COFs have centered around a variety of applications including gas storage,[48] sensing,[49] and photocatalysis.[50] Predictably, arrangements of pi-pi stacking structures as well as pores are highly favorable for all these applications. Recently there have also been several papers looking at the interfacing of COF to carbon nanomaterials for additional applications including supercapacitors,[51] transistors,[52] and batteries.[53] Utilizing the crystalline structure for a physical etching template was a driving force in the work presented below.

1.3 Metal Organic Frameworks

Metal organic frameworks (MOFs) are a diverse class of organic-inorganic porous crystalline materials with well-defined topology.[54] Similar to COFs, prediction of topology from linker and ligand environment of the metal are defining characteristics for this class of materials as shown in Figure 1.5. The primary distinction is the formation of coordinate bonds as opposed to covalent linkages. Rational prediction of structure is predicated on the knowledge of secondary building units (SBUs) which consist of metal ions or clusters and their preferred coordinative environment based on charge and ligands. Porosity (as assessed by surface area) similar to or superior than COFs can occur in both 2-D as well as 3-D contexts. A variety of bonding chemistries have been used to make MOFs but most commonly carboxylate-metal type linkages dominate the synthesized cases.[55] A particularly popular motif has been catecholate type linkages which can engender an overall square planar or octahedral environment around the metal site.[56, 57]

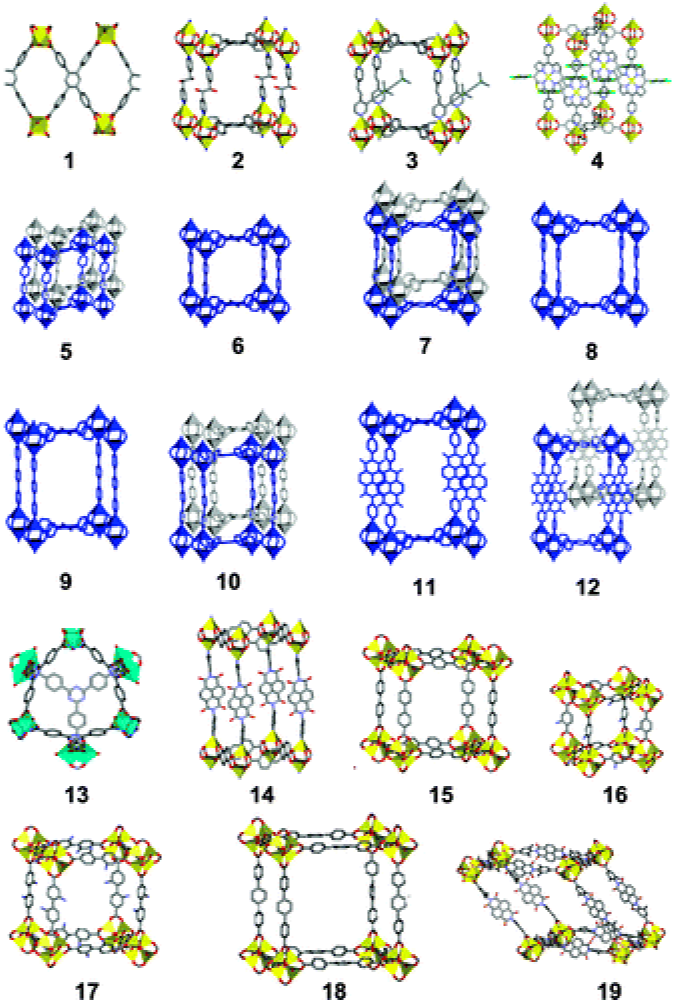

Figure 1.5 Various MOF topologies contingent upon linkage identity and secondary building unit including interpenetrated networks. Reprinted with permission from reference.[58] Copyright © 2010, American Chemical Society

The versatility of the chemical functionalities and topologies that MOFs can take on make them attractive for electronic applications. Unfortunately, due to more ionic type linkages between metal cations and organic molecules, most electronic transport through MOFs has been defined by hopping type transport between distinct molecular orbital as opposed to band type transport observed in completely conjugated systems.[59] Many recent examples of more band like transport have been reported leveraging mixed valence systems and larger pi-systems in the linkers as shown in Figure 1.6.[60-62] While there have been some notable recent examples of high electrical conductivity in systems, most of the reported syntheses MOFs are insulating preventing a large set of applications from being explored.

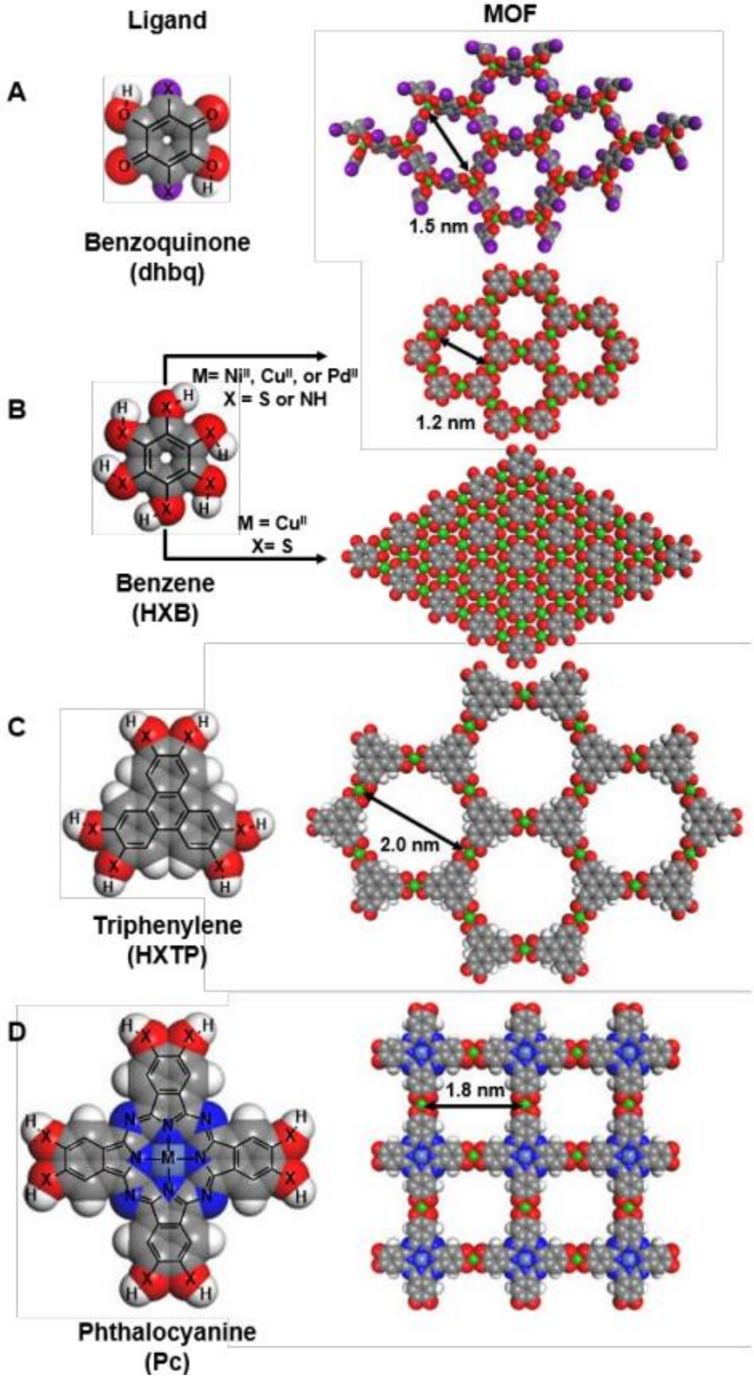

Figure 1.6 Prototypical metals and linkers in the formation of conductive MOF materials. Reprinted with permission from The Royal Society of Chemistry, reference.[62]

A particularly promising application of these systems has been using them as chemiresistors and other chemical sensors. The large structural possibilities, porosity, and chemically tunable of these structures makes them ideal for detection of chemical environments. Integrating electrical conductivity into these materials enables the long-range transmission of chemical events which is otherwise challenging. There is also distinct promise in studying chemical events confined to nanoscopic distances. This highly confined regime is used here to develop size selective sensing in combination with single walled carbon nanotubes.

1.4 Metallic Nanoparticles

Metallic nanoparticles are an archetypal nanomaterial due to their relatively long history as compared to other materials with initial reports stretching backing to ancient Rome.[63] Modern understanding of these phenomena have centered around surface energy considerations for the generation of different nanoparticles and sizes.[64] Considering a bulk metal, each metal atom has a definite translational invariant coordination environment to its respective surrounding atoms dependent on unit cell. This set of interactions is favorable based on valence orbital considerations for the relative environmental considerations. Instead of considering an atom located in the bulk, we could instead consider an atom located at the surface. This surface atom inherently lacks the same coordination environment as compared to the bulk atom due to exposure to the atmosphere or other non-metal atoms. As a result, to minimize the unfamiliar interaction with the non-metallic environment, the surface atoms will contract their bond lengths, altering the orbital interaction with sub-surface atoms, and seek additional ligands to bind to minimize their surface energy. Generally, bulk atoms are more stable than surface atoms as illustrated in Figure 1.7. While this phenomenon can be considered at a surface, one could also consider this occurring at the boundary of a sphere defining the nanoparticle. Therefore, small nanoparticle will be highly unstable due to the relative ratio of surface to bulk atoms.[65] In efforts to stabilize these atoms, other chemistry, here called ligands, can be used to decrease the unfavorable interactions at the surface.

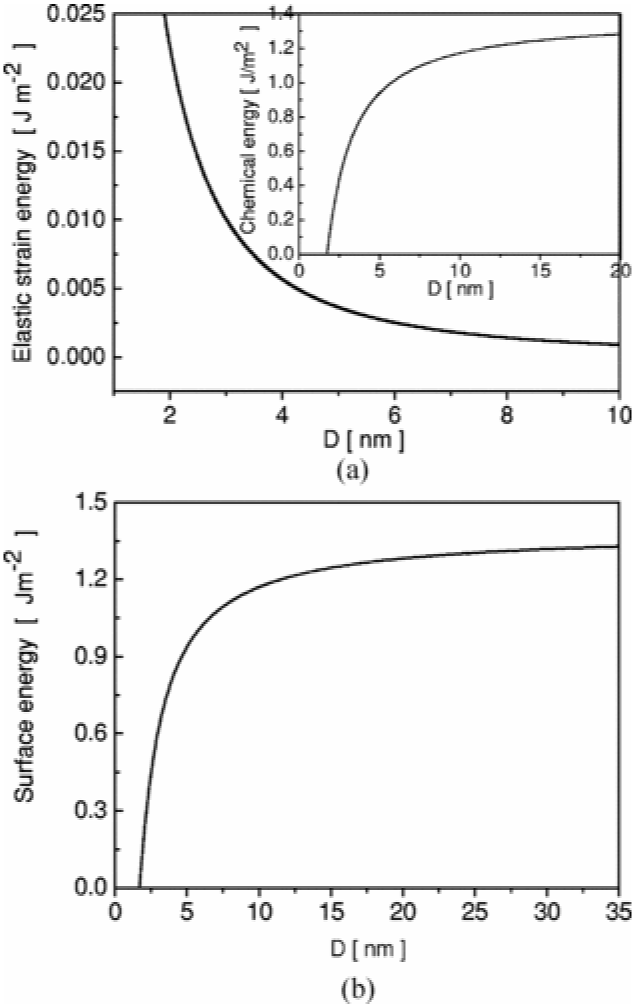

Figure 1.7 Illustrations of changing strain and surface energy with respect to the size of gold nanoparticles. Reprinted with permission from reference.[65] Copyright 2006 American Physical Society

Synthesis of spherical metallic nanoparticles have several routes, but one potential route is through appropriate metal containing precursors combined with a reducing agent and potentially a ligand or surfactants to dictate the size of the resulting nanoparticle. Thermal decomposition of organometallic precursors is another potential route which will not be considered for the purpose of this work. Synthetic considerations can hinge upon pH, solvent environment, respective concentrations of metal precursor, ligands, reducing agent, temperature, and presence of light.[66] Characterization of resulting nanocrystal structure size is typically conducted through transmission electron microscopy as well as dynamic light scattering. In this work we consider using holey graphene as both a ligand and reducing agent to synthesize size-controlled nanoparticles.

1.5 Electronic Sensing Materials and Principles

Many low power sensors are constructed from materials which can conduct electrons. This enables output in response to sensing in terms of an electrical signal. A wide variety of methodologies exist, but most commonly changes in resistance are measured in response to a chemical event, termed a chemiresistor.[67-69] The chemiresistive material is typically semiconducting with surface functional groups that are altered in response to chemical interactions with an analyte. The device architecture typically uses metal electrodes as a source and drain for charge injection into the material with an example as shown in Figure 1.8. By applying a potential bias across the material, current can be measured inversely proportional to resistance of the semiconductive channel material. These devices offer many benefits including simple construction, low cost, low power consumption, and readability of output signal.

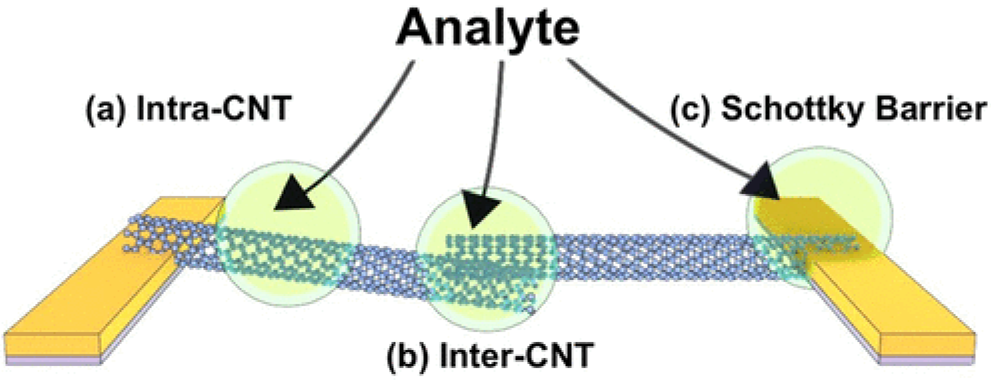

Figure 1.8 Illustration of a carbon nanotube chemiresistive device and potential sensing mechanisms. Reprinted with permission from reference.[70] Copyright 2019 American Chemical Society

Resistive changes may happen through a wide array of potential mechanisms. Direct charge transfer is commonly cited as a mechanism. This doping is caused by charged analytes approaching the surface of the sensor and altering the local chemical potential which in turn changes the resistance of the device. Alternative mechanisms include Schottky barrier modification of the junction of metal and the semiconducting channel.[71] As the analyte interacts at this junction, the relative work function difference of the metal-semiconductor junction is altered which in turn alters the resistance of the materials by enabling more or less charge injection at a given potential bias.

1.5.1 Traditional gas sensing materials

More traditional commercial sensors are based on semiconducting metal oxides.[72] These materials require high temperature to activate surface functional groups as well as decreasing resistivity to enable sufficient signal to be read out of the device as shown in Figure 1.9. High temperatures limit the application of these devices as persistent sensors due to the power consumption requirements. Additionally, they are often constructed of bulk materials which limits their sensitivity as events as the surface of the sensors do not necessarily change the resistance in the bulk of the device.

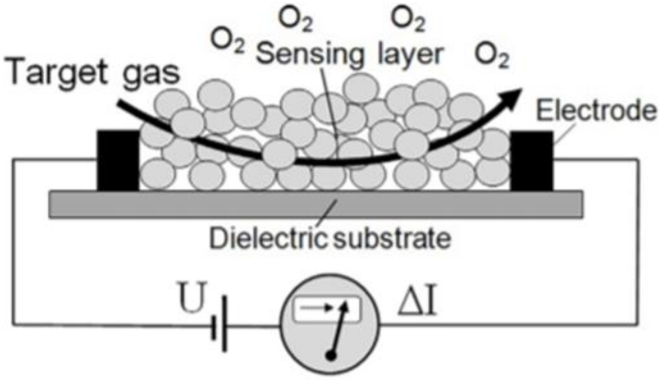

Figure 1.9 Illustration of a typical metal oxide gas sensor. Reprinted with permission from reference.[73] Copyright 2017 Elsevier

1.5.2 Field-effect transistors (FET) as a characterization methodology

More complex electrochemical sensing methodologies can also be employed by monitoring how the devices change in response to chemical environment while also changing the chemical potential of the semiconducting material with an electrical field. This device architecture is typically called as a ChemFET. Field-effect transistors monitor current across a semiconducting junction while an electrical field is varied across the junction. The electrical field alters the electrochemical potential of the carriers inside of the semiconductor allowing for more or less current to flow based on the band structure of the semiconducting material. FET techniques can be executed both with solid state and liquid capacitive structures as shown in Figure 1.10.

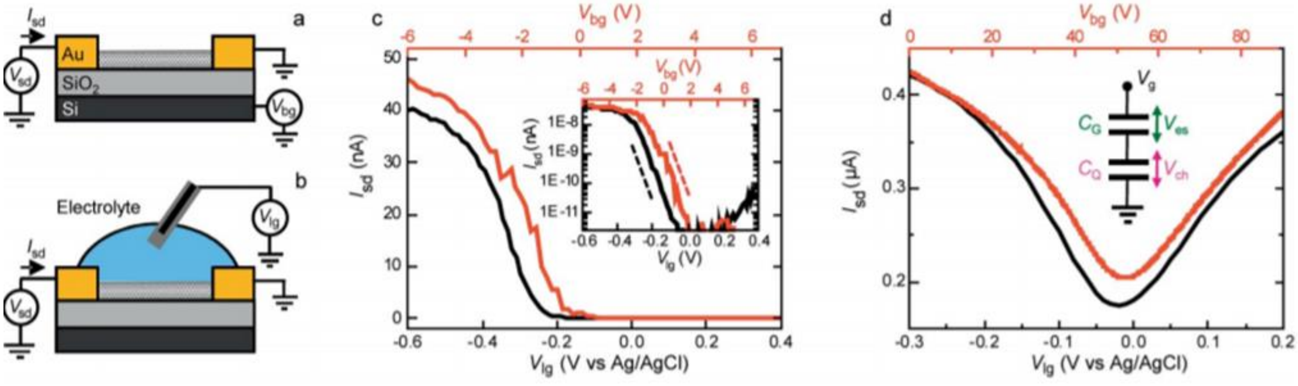

Figure 1.10 a, b) Diagrams of back-gating and liquid gating schemes for SWCNT and graphene transistor. c, d) Representative FET curves for SWCNT and graphene transistors. Reprinted with permission from reference.[74] Copyright © 2009 WILEY-VCH Verlag GmbH & Co. KGaA, Weinheim

SWCNT make exceptional FET devices due to their unique band structure which can enable differences in current to reach multiple orders of magnitude difference with relatively small applications of electrical field.[75] While FETs can be operated in solid state via capacitive charging, most of the discussion here is limited to liquid-based FET operation where ions in the solution act as the capacitive charges under application of an electrical field. This large change in current in response to electrical field can also be leveraged for chemical sensitivity. As chemical analytes approach the surface of the SWCNT, the chemical potential of the SWCNT is changed. Application of an electrical field has an additive effect to this change. By examining how the FET curve changes before and after chemical environmental changes, sensors can be constructed. Beyond sensing transient changes in chemical environment, FET curves also can be used as valuable diagnostics of the band structure of the underlying material before and after chemical modification to fabrication chemical sensors. This type of sensing operation can be extended with a wide range of chemistry including metal nanoparticles[76], biomolecules[77], polymers,[78] and small molecules.[79]

1.6 Nanomaterial Composites

While nanomaterials are beginning to be manufactured commercially,[80] many future applications of those materials would benefit from a rational integration of several different nanomaterials. Combinations of differing dimensionalities of nanomaterials can help control chemical processes occurring at their surfaces, enable long range interactions, and develop entirely new material characteristics which cannot be reduced into simple decompositions of individual materials. For instance, metal nanoparticle (zero dimensional) decoration of carbon nanotubes[81] (one dimensional) or graphene[82] (two dimensional) enables long range transport of localized changes to the chemistry at the nanoparticles surface. Another example would be the layering of 2-D organic frameworks on top of carbon nanomaterials[83] to restrict diffusion to the surface acting as a size selective membrane with potential for further control of the pore through post synthetic chemistry.

Many nanomaterial composites are formed via simple combinations of the individual constituents after respective synthesis. While this leads to well defined materials, it often limits the extent of chemical and electronic coupling between the materials. Another strategy is to use one material as a substrate for another to grow on in a structure directing manner.[84] This is often the most exciting application of composite materials as it enables strong interaction between the respective components. Syntheses which generate both materials at the same time are rare due to the large thermal and chemical differences in different synthetic methods.

1.7 Electrocatalytic Reactions for Energy

Current methods for producing energy for the planet heavily rely upon the combustion of hydrocarbon fuels. This combustion leads to a variety of products including carbon dioxide, water, and numerous carbonaceous products. Carbon by-products are hazardous for human health and have been implicated in several disease states and carcinogenic potential. Beyond immediate health implications, the build-up of carbon dioxide in the atmosphere has a range of negative consequences including but not limited to climate change, ocean acidification, sea level rise, and more extreme weather events.[85] It is crucial that future developments for energy production avoid combustion as the primary energy generation modality. Electrochemical reactions are efficient and pollution-free methods to store and release energy on demand. Most electrochemical reactions have large activation energy (kinetic) barriers to perform the work needed to oxidize or reduce chemical reactants. One of the most desirable set of reactions to develop is the electrochemical reactions involving water shown below in Figure 1.11

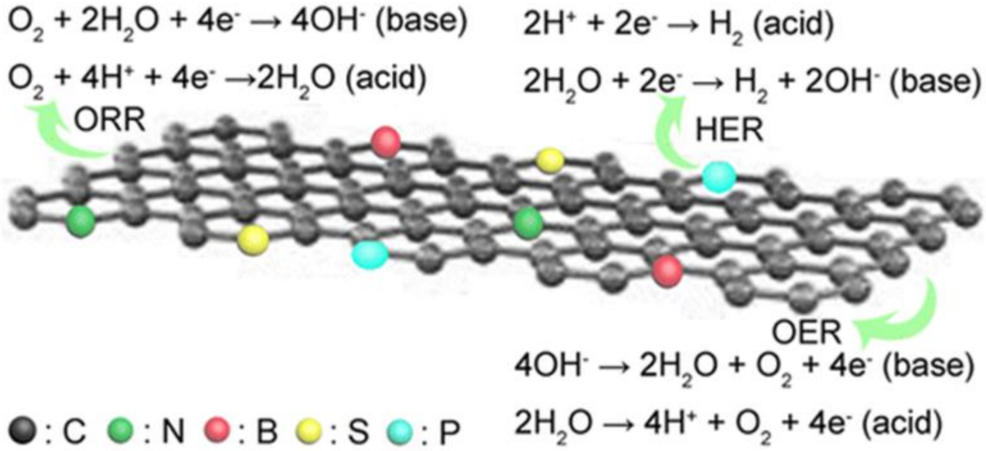

Figure 1.11 Scheme of heteroatom doped graphene and electrochemical half reactions of in differing pH environments including oxygen reduction (ORR), hydrogen evolution reaction (HER), and oxygen evolution reaction (OER). Reprinted with permission from reference.[86] Copyright 2015 American Chemical Society

None of the above reactions involve carbon and only require or produce water, hydrogen gas, oxygen gas, hydroxide ions, and protons. These reactions are useful both as potential energy storage in using them as hydrogen and oxygen gas production methods[87] (water splitting) as well as in fuel cell applications[88] where combining hydrogen and oxygen can be used to generate a potential difference to drive an electrochemical circuit. The particular reactions required for fuel cells would be the hydrogen oxidation reaction and oxygen reduction reaction. This work will focus on the energy storage reactions of hydrogen evolution reaction and primarily oxygen evolution reaction (OER). In addition to being useful for storing the energy of water splitting, OER can be coupled to carbon dioxide reduction to generate valuable hydrocarbon fuels from what is a currently a waste product.

The best existing commercial catalysts for OER have been iridium[89] and ruthenium[90] based materials, which are unfavorable due to scarcity and cost. Much effort has been placed into improving the ability of more common transition metals, cobalt,[91] nickel,[92] iron,[93] and manganese,[94] to catalyze the energetically challenging multiple proton transfer steps. Often explanations of electrocatalytic efficiency are considered in terms of the placement of d-band center[95] and the favorable binding energy of the reaction intermediates.[96] The principal reason that the more noble catalysts mentioned above work so well is an intermediate binding strength of different reactants. This ability allows for reactants to diffuse to the surface and have electrochemical transfer to take place followed by the products being capable of leaving. The multistep nature of OER makes this consideration especially important. One way to tune the binding strengths of the reactants is to change the size of the catalyst, which in turn alters the exposed facets and alters the surface energy. Another way to alter this binding energy is to change the supporting material which delivers the electrons to the catalyst. In this work, we consider utilizing the coupling of holey graphene materials which can both act as a facile electron transfer support as well as dictating the size of the catalyst by the size of the holes.

2.0 Holey Graphene Metal Nanoparticle Composites via Crystalline Polymer Templated Etching

2.1 Preface

Parts of the text as well as figures were published in "Holey Graphene Metal Nanoparticle Composites via Crystalline Polymer Templated Etching" and have been reprinted with permission from *Nano Lett.* **2019**, *19*, 2824–2831. Copyright 2019 American Chemical Society

List of Authors: David L. White, Seth C. Burkert, Sean I. Hwang, and Alexander Star

Author Contributions: DLW and AS designed the experiments and wrote the manuscript. DLW performed the bulk of the experimental work. SCB captured electron micrographs and XPS spectra. SIH captured the gas sensing data.

2.2 Introduction

Holey graphene structures have been pursued for use in electronic devices to modulate graphene's semi-metallic band structure through quantum confinement.[97] The three primary routes towards producing these structures are further oxidation of graphene oxide[98] type structures,[99-104] traditional lithographic processes,[68, 105-107] or bottom-up organic synthesis.[108] Further chemical or biological oxidation of graphene oxide structures lacks control over size and placement of holes generated. Traditional lithography allows for control over size and placement of holes but often lacks the necessary resolution to access significant band modulation that occurs at sub-5 nm neck widths. While bottom-up syntheses generate well defined structures with appropriate dimensions to access properties induced by dimensional reduction, the syntheses are generally not scalable to large areas. Our approach presents an advancement of utilizing a combination of the bottom-up synthesis of 2-D covalent organic frameworks onto graphene and the top down process of reactive ion etching (RIE) to affect the underlying graphene structure.

Covalent organic frameworks (COF) have been developed for many applications including gas storage,[109] organic electronics,[110] capacitors,[111] and catalytic applications.[112] Their application towards physical templating has been left unexplored. The crystalline structure of the polymers can be predicted in advance and provides an interesting avenue towards bridging traditional photolithography with rational chemical synthesis. COF-5, which as previously shown[47] orients with respect to graphene, has pore dimensions of 2.7 nm and is used here to provide high density patterning of graphene enabling unique composites which retain the outstanding electrical properties of graphene.

Graphene composite materials are useful for many applications ranging from chemical sensing[113-115] to catalysis.[116, 117] While pristine graphene has been demonstrated to be an excellent material for the aforementioned applications, there are limitations imposed by the nature of the material. The lack of functional groups, while enabling extraordinary conductivity, makes composite material manufacture more difficult. The primary difficulty in introducing functional groups is the destruction of the sp2 network. For applications where, composite materials would benefit from graphene’s extraordinary conductivity, the oxidative processes to introduce chemical handles are problematic. The ability to introduce a high density of oxidative moieties while retaining the underlying graphene conductivity represents a useful advance in graphene composite materials. Additionally, it has been shown that these oxidative moieties can act as reduction sites for metal ions to form metal nanoparticles.[118, 119] Thus, patterning allows for high density size-controlled nanoparticles that are electronically coupled through graphene which exhibits Raman enhancement and chemiresistive gas sensing applications presented here.

2.3 Results and Discussion

The changes in physical characteristics of graphene were tracked through a combination of SEM and high resolution TEM shown in Figure 2.1. Graphene, grown via an atmospheric chemical vapor deposition (APCVD) process,[120] was transferred from the copper foil substrate to a prefabricated silicon chip. Transfer occurred without polymer support to ensure intimate contact between the COF-5 and graphene as well as avoiding a subsequent step to remove polymer support residues.[121] Graphene was observed via SEM being draped between two electrodes approximately 6 μm apart displayed in panel a. Minimal wrinkles and no holes or defects are observed confirming that the transfer process preserves the integrity of the graphene.

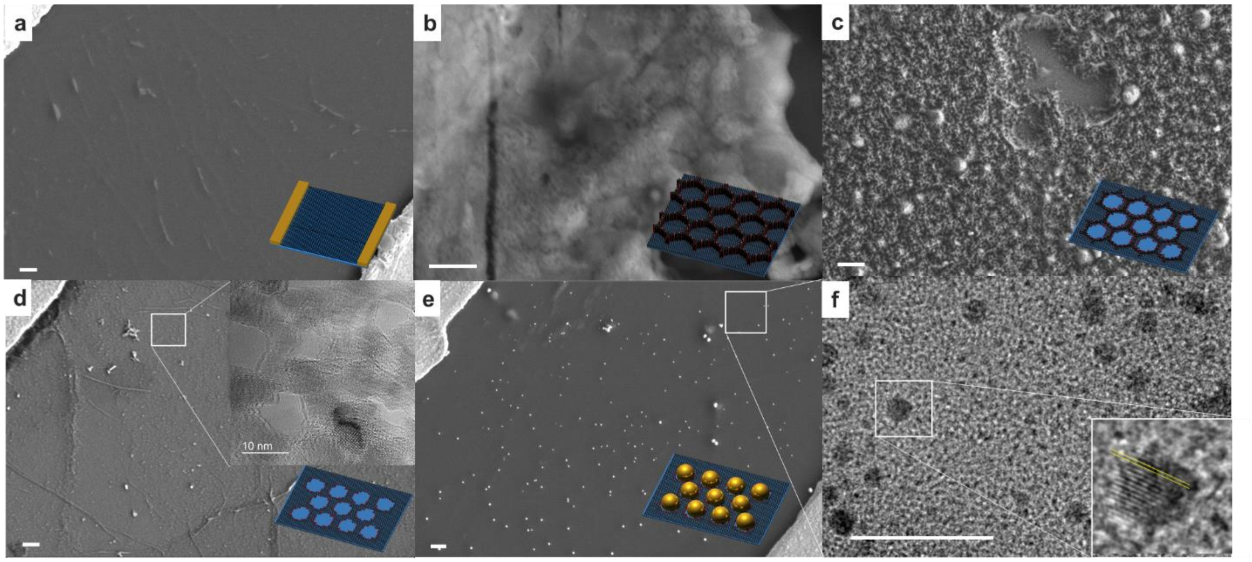

Figure 2.1 Electron micrographs tracking physical differences in graphene across the COF-5 templating process. a) Transferred graphene on a Si chip with interdigitated gold electrodes. b) COF-5 growth on the graphene chip. c) O_2 RIE etches COF-5 and graphene. d) Ethanol removes most of the COF-5 revealing patterned graphene. Inset: High resolution TEM micrograph demonstrating adjacent hole formation from COF patterning. e) Soaking in a 1 mM $HAuCl_4$ solution generates nanoparticles at oxidized hole sites. f) High resolution TEM micrograph illustrating nanoparticle formation corresponding to patterned holes. Inset: distance between highlighted lines is consistent with a lattice spacing of 0.204 nm indicating a gold (200) lattice plane. All SEM scale bars are 200 nm. The HRTEM scale bar in panel f is 20 nm. Reprinted with permission from reference.[122] Copyright 2019 American Chemical Society

COF-5 is synthesized via a modified solvothermal process[47] and orients its pores normal to the graphene. COF-5 is approximately as thick as the electrodes, which are 65 nm. Previous reports of the synthesis indicate that platelet formation for COF-5 are 7 nm thick.[47] We observed multiple layers of COF-5 on top of the graphene. COF-5 thickness measured via AFM demonstrate that our modified procedure on the prefabricated chip produces a minimum of 25 nm of COF-5 growth after 30 minutes of reaction time as compared to the observed ~65 nm of growth from 40 minutes of reaction time. While it has been previously reported that the ideal c-stacking arrangement of COF-5 is not perfectly eclipsed but slightly staggered,[123] this does not affect the described process because the layers of COF-5 closest to the graphene determine the patterning profile. Further high-resolution TEM micrographs, PXRD, and FTIR match[47] early timepoint formation of crystalline COF-5 as seen in Figure 2.2.

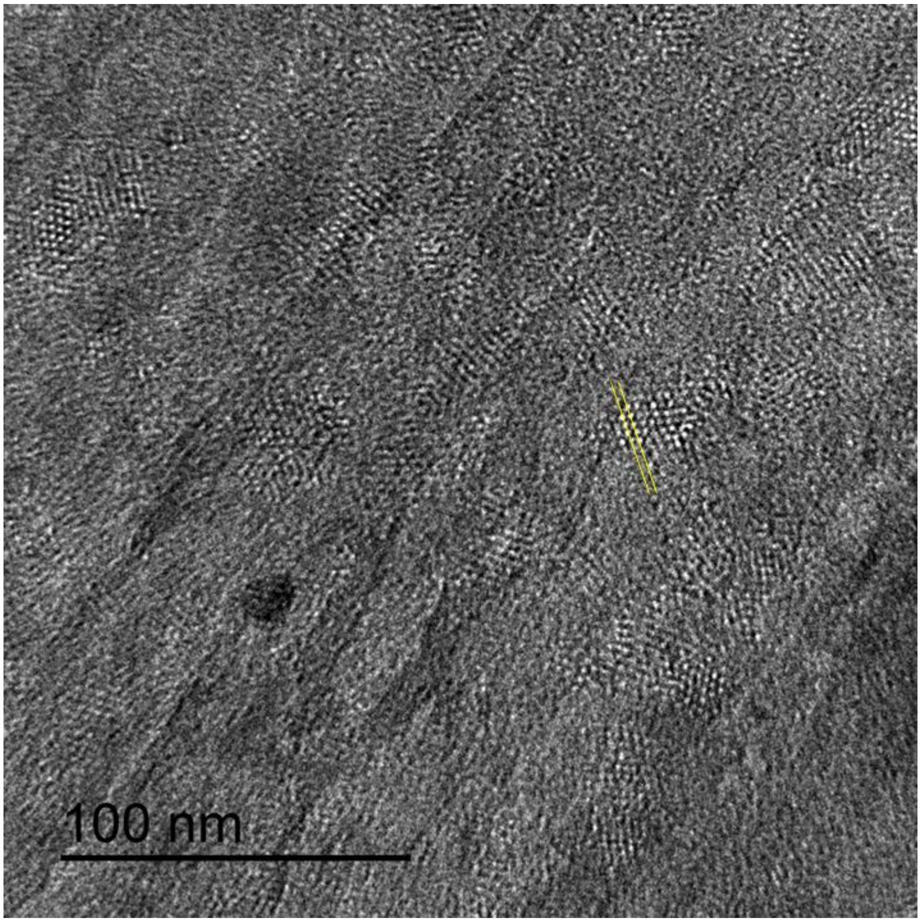

Figure 2.2 HRTEM micrograph of COF-5 on top of graphene with highlighted spacing of the crystalline regions that correspond to the hole spacing (2.7 nm) from the COF-5. Reprinted with permission from reference.[122] Copyright 2019 American Chemical Society

RIE utilizes oxygen plasma and a voltage bias to anisotropically etch through both the polymer and graphene. RIE promotes formation of dense holes in the polymer and changes in the electrical properties of graphene. RIE processing without the polymer destroys the graphene completely. Conditions to achieve regular patterning and changes in electrical characteristics were empirically optimized. The COF can be envisioned as both providing the initial template for the hole formation as well as acting as a temporary stop against overoxidation by protecting reactive sites formed in the initial oxidation. Larger white formations embedded within the etched polymer were attributed to homogeneous phase growth of COF-5 that was included in the film during the COF growth process[47] and are randomly oriented with respect to the surface of graphene and therefore lack distinct holes. COF-5 remains after etching as evidenced by SEM and must be removed through an ethanol wash.

The underlying graphene displays dense patterning on SEM and TEM. Residual COF-5 persists here but is ultimately removed in the metal salt soaks due to longer exposure to aqueous conditions. Overall structural continuity of the graphene remains intact and the COF-5 templating process is conformal with respect to the wrinkles. Across the relatively large area of the spacing between the electrodes, some areas experience more extensive oxidation. Extra oxidation is attributed to the unevenness in the thickness of the COF-5 where thinner areas will experience more intensive etching as compared to relatively thick areas. The inset reveals several adjacent holes with dimensions marginally larger than COF-5. Uneven etching across areas on prefabricated chip devices which we partially attribute to height changes caused by the presence of gold electrodes affecting the quality of the COF grown. When the patterning process is conducted on bare silicon wafer, AFM across micron-sized areas reveal relatively consistent patterning as seen in Figure 2.3.

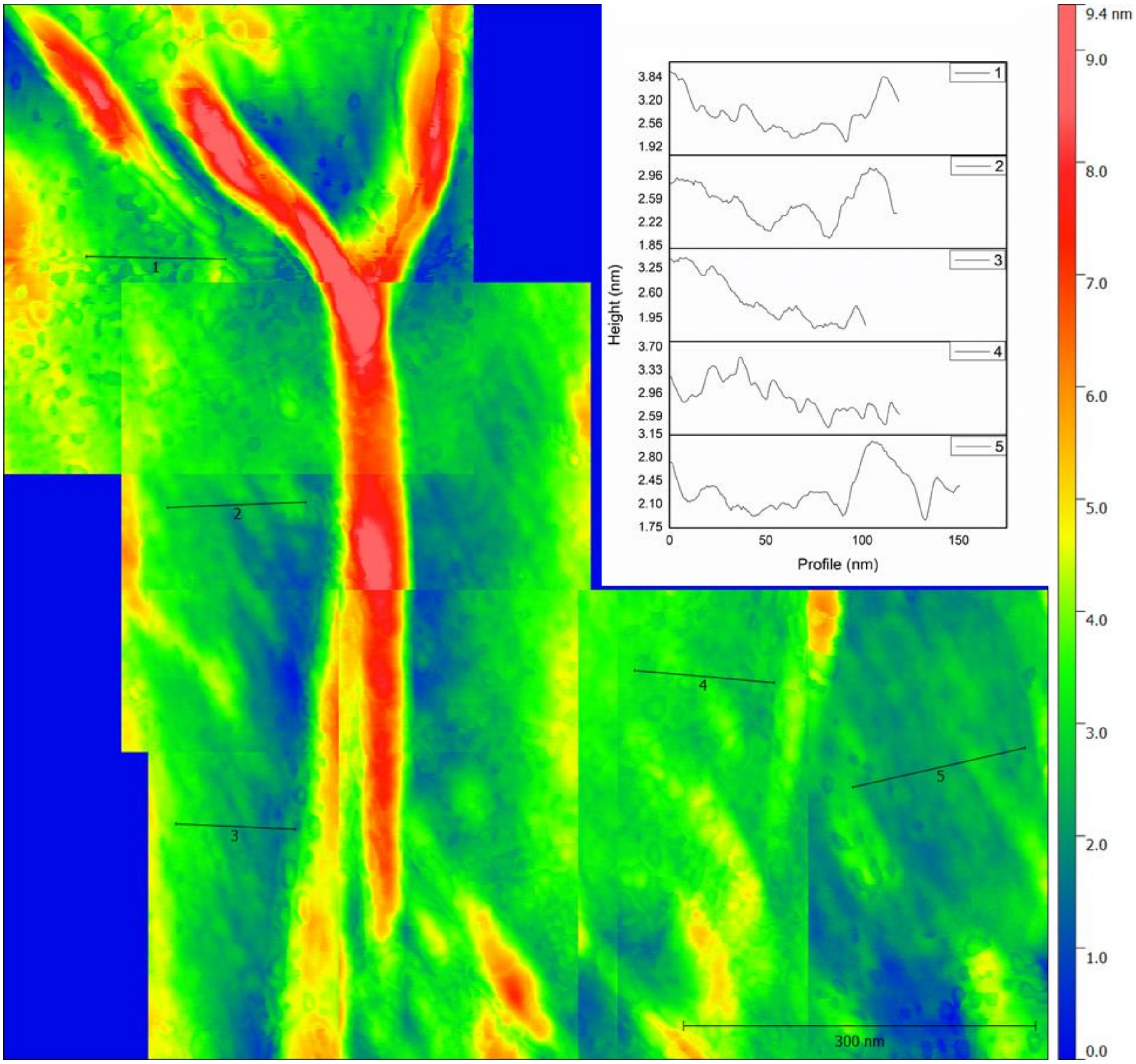

Figure 2.3 Stitched together AFM micrographs of patterned graphene after ethanol wash on bare silicon wafer demonstrating consistency over micron size areas. Upper right area depicts five separate profiles taking from each individual area consistent with patterned holes formed in graphene. The holes which can be contrasted against the relatively large height of the wrinkle feature shown in red. The repeating structure and minor height variations are consistent with holes in graphene. Reprinted with permission from reference.[122] Copyright 2019 American Chemical Society

COF-5 templated holey graphene structures are soaked in 1 mM noble metal solutions for two hours in a dark environment to promote nanoparticle growth at the reactive hole sites. Both gold and palladium solutions yield templated nanoparticle growth. Reduction of nanoparticles has been previously reported for gold at higher concentrations on graphene oxide composites.[118] The primary distinction between graphene oxide and our material is that the oxidative hole formation is templated and provides a confining environment. This is illustrated by control experiments utilizing as transferred graphene without any patterning exposed to the gold metal soak. While the as grown graphene is intact as confirmed by Raman spectroscopy (*vide infra*), it is known that CVD graphene will have defects over larger area growth without special synthetic consideration. Additionally, the transfer process provides an opportunity to damage the graphene or introduce wrinkling. The primary sites of formation are on edges, wrinkles, and defects. COF-5 based plasma patterning introduces more edge sites which act as nucleation sites for nanoparticle growth. Further control experiments with growth and removal of COF without RIE demonstrate that COF impurities lack the ability to seed appreciable gold nanoparticle growth.

Two types of nanoparticle growth occur with larger (40.1 ± 10.3 nm, n = 57) and smaller (3.27 ± 0.81 nm, n = 61) nanoparticles forming based on TEM observations. Additional oxidation contributes to the formation of larger nanoparticles by providing larger holes for nanoparticle formation. Overgrowth of individual small nanoparticles into larger nanoparticles is also observed in HRTEM images and contributes to multiple size distributions of nanoparticles. In areas where only the initial templated holes form, only small nanoparticles are produced. EDAX data collected during SEM confirms the identity of the nanoparticles as gold. Large area to area variation shows different distributions of nanoparticle growth. Some areas are only populated by smaller nanoparticle growth while others have both kinds.

Additional AFM images were taken on the post gold metal soak condition to understand the extent of gold nanoparticle formation and confirm high patterning density. Extensive minor height deviations are attributed to hole formation while large increases in height are assigned to gold nanoparticle formation. The lack of total coverage by gold nanoparticle formation on the small scale of the AFM image indicates that the concentrations used do not promote complete gold nanoparticle formation across the entire patterned graphene sheet. Higher concentrations were avoided to mitigate overgrowth. The high-resolution images confirm the successful patterning of the underlying graphene by COF-5 based plasma etching.

Further AFM images conducted on bare silicon wafer as opposed to prefabricated chips in the post gold metal soak condition demonstrate consistent patterning as well as gold nanoparticle formation as displayed in Figure 2.4. Over micron sized areas both holes (blue areas) and gold nanoparticles can be observed filling the patterned graphene. Magnified images reveal only partial filling in of the gold nanoparticles in formed holes. Medium range patterning displayed here holds the promise of COF based templates as a viable patterning strategy for achieving few nanometer sized features across micron areas.

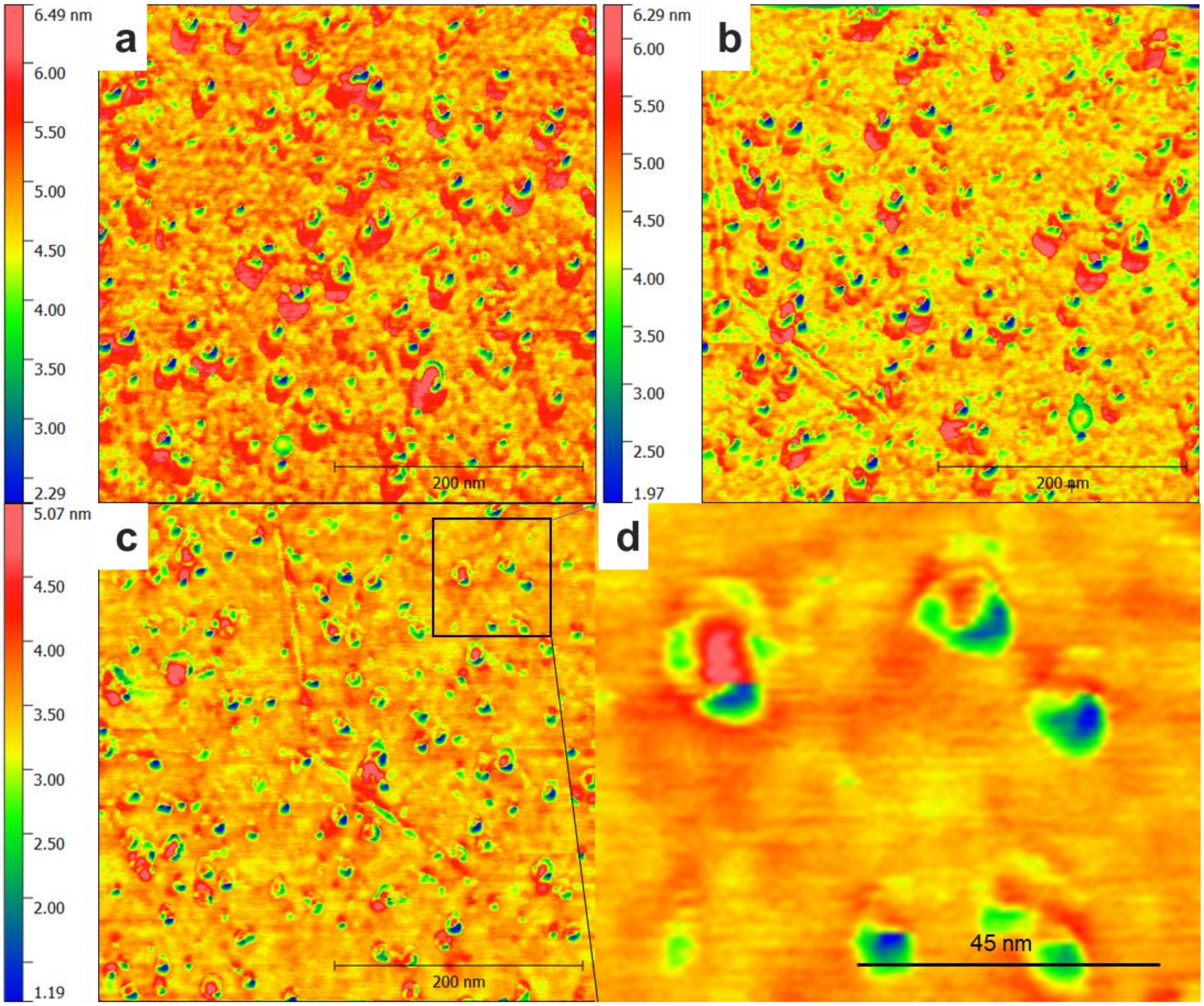

Figure 2.4 AFM micrographs of holey graphene gold nanoparticle composite on bare silicon wafer. a, b, c) Micrographs taken across a micron sized area showing consistent patterning. d) Magnified image for c) illustrating gold nanoparticles partially filling in COF-defined holes. Reprinted with permission from reference.[122] Copyright 2019 American Chemical Society

Patterning and nanoparticle growth were tracked both through spectroscopic and electrical measurements as seen in Figure 2.5. Raman spectroscopy is leveraged as a technique to track the changes in the structural characteristics of graphene during patterning.[124] The initial Raman signal contains the signature D, G, and 2D peaks at 1350, 1570, and 2690 cm^{-1}, respectively. The D peak in the initial spectrum is ascribed to the transfer process because the spectrum of the graphene on the copper foil has no appreciable D peak. After COF-5 is grown on top of the graphene, the Raman signal changes showing signal dominated by characteristic COF-5 peaks with a large decrease in the relative 2D peak intensity. Oxygen plasma etching induces a general decrease in signal accompanied by an increase in the D region of the spectra. Washing with ethanol reveals a large increase in the 2D intensity signifying that the underlying graphene is being probed indicating the removal of the overlying COF. Gold soaking induces three orders of magnitude increase in the signal of all three peaks as well as revealing an indictive shoulder peak, D', on G sourced from defect formation. The large increase in signal is attributed to a plasmonic enhancement from densely packed small gold nanoparticles.[125] The palladium-soaked composites do not show similar enhancement.

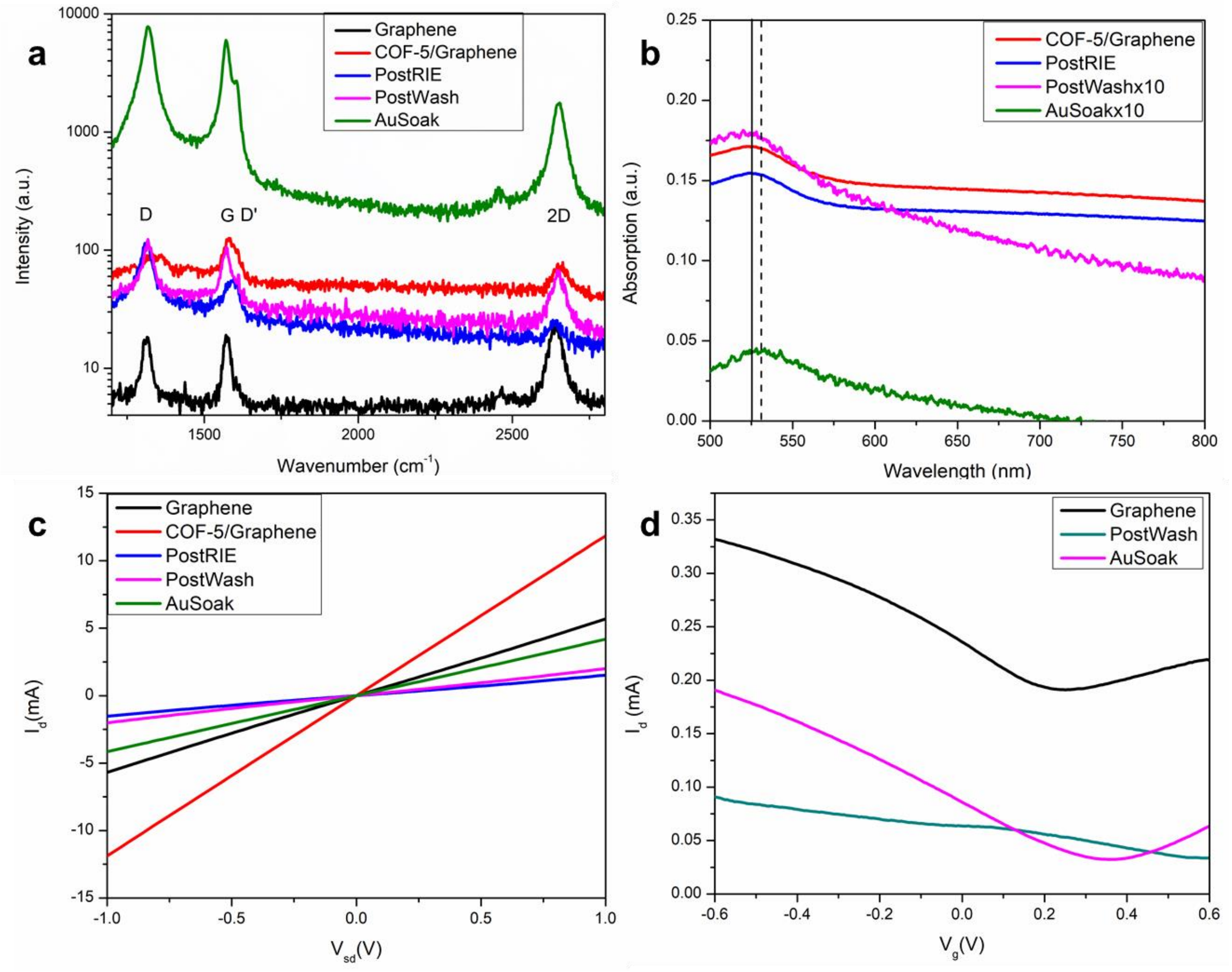

Figure 2.5 Optical and electrical measurements throughout the COF-5 templating process. a) Raman spectroscopy tracking changes during patterning. Intensity is plotted in log scale to capture the large increase in signal following gold soaking because of Raman enhancement. b) UV-Vis tracking changes from COF-5 growth. The solid and dashed vertical lines indicate λmax before and after gold soaking respectively. The signal of both post wash and gold soaking have been multiplied by ten to enable more direct comparison. c) Current-voltage characteristics measurements throughout the process. d) Liquid gated FET (vs 1 M Ag/AgCl) measurements of the structure at select time points. Reprinted with permission from reference.[122] Copyright 2019 American Chemical Society

Tracking the process through UV-Vis absorption spectroscopy on a quartz slide substantiates complementary physical changes in the visible absorption that are substrate independent. COF-5 on top of graphene dominates the initial signal with a peak around 525 nm.

Oxygen plasma decreases the general signal via removal of COF-5. Residual COF-5 remains after washing with ethanol, but the signal is still relatively weak compared to the initial and post plasma conditions. Soaking in a $HAuCl_4$ solution shifts the peak absorbance to 530 nm, indicating the formation of small gold nanoparticles.[126]

Current voltage measurements serve as a complementary method to track the progress of templated hole formation. Transferred graphene has linear increases in current in response to source drain biases sweeping from –1 V to +1 V. COF-5 growth generates a general increase in current in response to bias voltage across the entire range. COF-5 is electronically coupled to the underlying graphene.[127] Plasma etching decreases current across the entire range consistent with oxidation of the underlying graphene. Washing with ethanol removes most of the oxidized COF-5 and increases the current observed. Introduction of $HAuCl_4$ solution restores the current again to just below the level of the initial starting condition.

Liquid gated field-effect transistor (FET) measurements tracks the gate modulation of the current in response to the templating process. Initially, graphene demonstrates semi-metallic behavior with a p-type shift in the minimum conductance point that is attributed to atmospheric contamination and substrate effects.[128] Liquid gating measurements cannot be performed when the COF-5 is introduced due to the water sensitivity of COF-5.[45] COF-5 templated patterning decreases current and gate modulation as compared to the initial FET measurements even after washing with ethanol. The minimum conductance point is so far p-shifted out of the electrochemical window that it cannot be observed.[129] Extensive doping of graphene with plasma processing is consistent with other reports in the literature.[130] Gold nanoparticle deposition reestablishes much of the graphene's initial behavior with lower overall current and a slight shift in minimum conductance while retaining the overall same shape of the FET curve. Reinstating semi-metallic behavior of graphene is attributed to gold nanoparticles partially filling in some of the holes.

X-ray photoelectron spectroscopy can be a powerful tool to assess changes in chemical bonding environments through ejection of core electrons as illustrated in Figure 2.6. High resolution XPS data of carbon enables tracking of relative ratios of functional groups throughout the patterning process. Initially, the signal of bare graphene is dominated by sp^2 carbon with minimal contributions of other carbonaceous species. Deposition of COF-5 has a concurrent increase in the quantity of C-OR functionalities as per the chemical structure of COF-5. RIE raises the quantities of C-OR functionalities relative to the sp^2 peak while concurrently introducing C=O functionalities. Due to the small penetration depth of XPS and the relatively large amounts of COF-5 left on the surface at the end of RIE, as evidenced by SEM and UV-Vis; we believe the more oxidized carbon contributions are primarily COF-5. Washing with ethanol to remove leftover COF-5 reveals a shift to larger binding energies in the main sp^2 peak and significant contributions of C-OR and C=O functionalities. Higher binding energies are consistent with an increase in oxygen type defects and electronic depletion of the local chemical environment of the remaining sp^2 carbon network. Electron deficiency correlates well with the observed FET characteristics. Introduction of $HAuCl_4$ facilitates auto-reduction into gold nanoparticles with concomitant decreases in C-OR and C=O type functionalities and restoration of the sp^2 peak back to a similar level as unprocessed graphene.

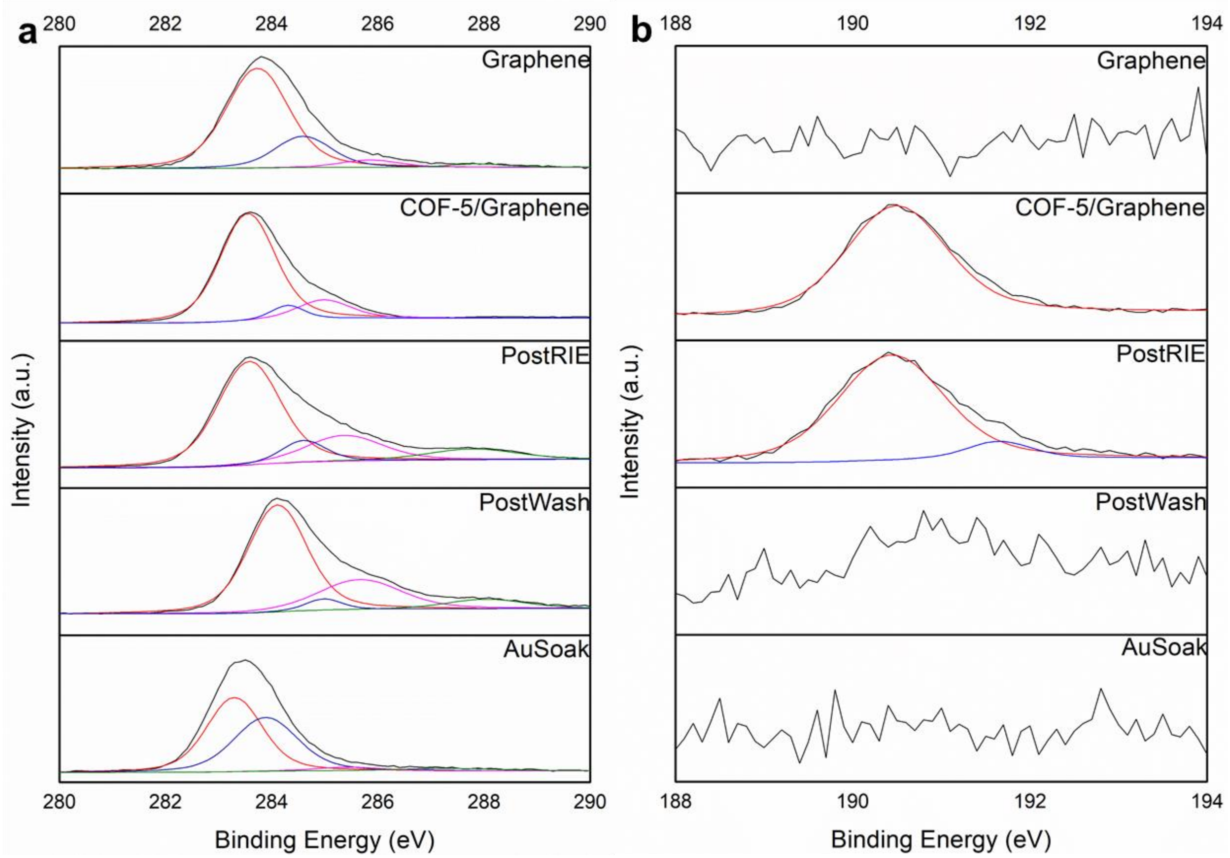

Figure 2.6 High resolution XPS of both carbon and boron at each step in the process on a prefabricated silicon chip. a) High resolution carbon 1s with deconvolutions of the signal. b) High resolution boron 1s with deconvolutions of signal. Reprinted with permission from reference.[122] Copyright 2019 American Chemical Society

High resolution XPS data of boron acts as a chemical handle to track the changes in COF-5 and the removal of COF-5 through ethanol washing. No boron signal is present in the initial graphene sample. COF-5 deposition reveals one boron peak that corresponds to the chemical structure of COF-5. RIE alters the local chemical environment of boron via reactive oxygen species as evidenced by the appearance of an additional boron peak at a higher binding energy. Ethanol washing removes the majority of remaining COF-5 as indicated by the disappearance of the boron peak. Lack of boron signal for the post gold soaking conditions confirms no residual COF remains on the final material.

Our material provides an interesting intermediate between the formation of graphene oxide and pristine single layer graphene with the primary distinction being introduction of patterned oxidative functionalities. Electrical characteristics in combination with the Raman measurements confirm that a contiguous sp^2 carbon network remains after patterning. The restoration in the p-type semi-metallic behavior confirms that a measure of the initial properties of graphene can be restored by partial filling in of the patterned holes by metal. Holes act as both reduction sites as well as a ligand environment for the formed nanoparticles. Interconnected metal nanoparticles through an electrically conductive graphene environment provides an excellent platform for sensing.

As an exploration of applications outside of Raman enhancement, both gold and palladium salt-soaked systems were tested for room temperature gas sensing applications of H_2S and H_2, respectively demonstrated in Figure 2.7. Both systems show remarkable sensitivity for their respective gaseous analytes with Au/H_2S having a calculated limit of detection of 3 ppb and the Pd/H_2 having a limit of detection of 10 ppm. Both systems showed reproducibility across different complete synthetic cycles with averages and standard deviations for a different run shown for responses.

The gold composite sensor has irreversible response due to strong gold sulfur interaction commonly reported.[131] Gold composite response is qualitatively similar in air as compared to N_2. The gold composite response is relatively unaffected by the different gold nanoparticle size distributions due to the surface-based interaction method of sulfur with gold. The effect of the gold electrodes on the sensing response corresponds to a small percentage of overall response at the highest concentration as confirmed by control experiments conducted under the same gas sensing conditions utilizing a graphene sample. The palladium composite sensor is believed to have an initially irreversible response due to larger nanoparticles generated at more oxidized sites that have slower recovery kinetics as compared to the smaller nanoparticles confined to the COF-templated holes. In N_2, the palladium composite lacks recovery and eventually saturates response. Lack of recovery is attributed to the need for O_2 to remove the hydrogen from the palladium nanoparticles.[132]

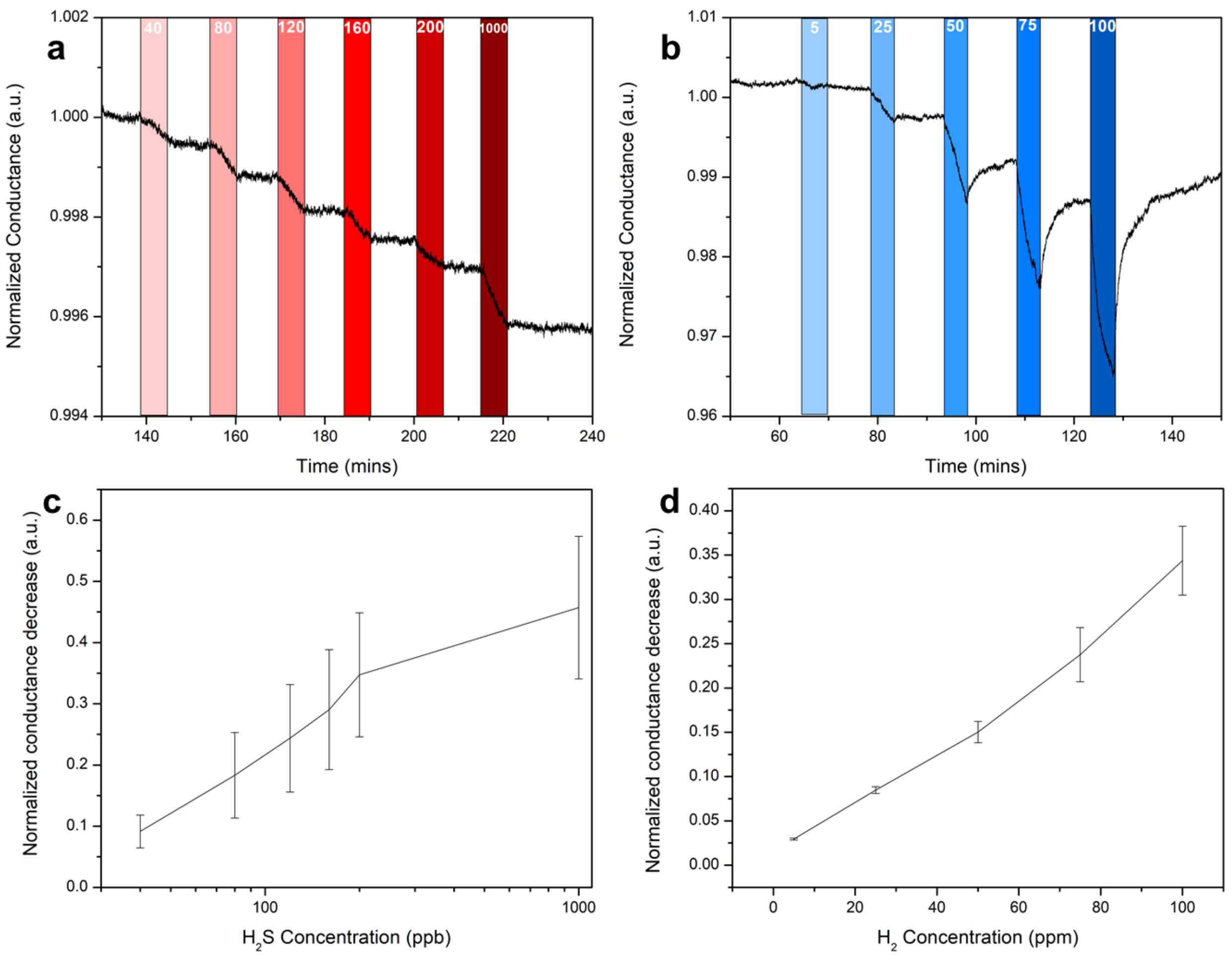

Figure 2.7 Room temperature gas sensing data for holey graphene composites a) Gold nanoparticle composite showing decrease in conductance in response to H_2S (ppb) in synthetic air. b) Palladium composite showing both irreversible and reversible responses to H_2 (ppm) in synthetic air. c-d) Averaged normalized conductance changes with standard deviation for H_2S (n = 6) and H_2 (n = 4) sensing, respectively. Reprinted with permission from reference.[122] Copyright 2019 American Chemical Society

2.4 Conclusions

The responses for gas sensing demonstrated here are near the top of the performance for limit of detection of similar graphene-based composites displayed in table 2.1.

Table 1 H_2S/H_2 Sensing Data Comparison

Material used	**Gas**	**Reversible**	**Lowest detection**	**Reference**
PtNPs on holey GO	H_2	yes	60 ppm	[102]
Multilayer GNRs with PdNPs	H_2	yes	40 ppm	[132]
rGO with PdNPs	H_2	yes	0.2 ppm	[133]
Flowerlike Pd on graphene	H_2	yes	0.1 ppm	[134]
GO with PdNPs	H_2	yes	1%	[135]
rGO with Pd nanocubes	H_2	yes	10 ppm	[136]
Holey Graphene PdNP	H_2	yes	10 ppm	[122]
rGO with SnO_2NWs	H_2S	yes	43 ppb	[137]
SWCNT with AuNPs	H_2S	yes	20 ppb	[131]
Graphene with AgNPs	H_2S	yes	100 ppb	[138]
rGO with AuNPs	H_2S	no	68 ppb	[139]
Graphene with AuNPs	H_2S	no	2 ppm	[140]
Holey Graphene AuNP	H_2S	no	3 ppb	[122]

There are only two reports of lower limits of detection for H_2 sensing and our H_2S sensing reports the best limit of detection to the best of our knowledge. The quality of the gas sensing behavior here is attributed to a combination of the ~3 nm metal nanoparticles with high conductivity that the holey graphene layer provides for transduction. The methodology presented here provides a route to pattern ~2.7 nm holes in graphene via COF-5 at high resolution and density side-stepping expensive processes like e-beam lithography and other traditional patterning methods. The composites formed through soaking with noble metal salts retain many of the properties of graphene including its semi-metallic nature while also enabling ~3 nm nanoparticle growth electronically coupled with graphene. The applications exhibited are of great interest for both Raman enhancement and gas sensing applications due to the relative ease of fabrication as compared to more expensive and complicated techniques. The H_2 (10 ppm) and H_2S (3 ppb) sensing limits of detection demonstrated here is comparable to the best results from similar graphene-based composites.

2.5 Experimental

2.5.1 APCVD growth of graphene

Cu foil was cut into 1 cm × 1 cm squares. The foil was cleaned by submerging into either 1 M HCl or 5.4% w/w HNO_3 for 30-40 seconds.[141] After removal from the cleaning solution the Cu foil was washed thoroughly with deionized water (18.2 MΩ cm^{-1}) and then blown dry with N_2 to remove all residual moisture.

The Cu foil was loaded onto a quartz crossplate and sealed into a 1-inch inner diameter quartz tube. The tube was loaded into the CVD oven and began a purge with argon (900 sccm) and hydrogen (50 sccm). After purging for 30 minutes the oven was ramped up to 980^{o}C over a period of 20 minutes. Cu foil was annealed at 980^{o}C for 10 mins at which point methane (10 sccm) was introduced to the oven for 30 mins. At this point, both the CH_4 flow and oven were shut off and the tube began cooling in air.

2.5.2 COF-5 growth

Heavy walled glass container was cleaned with a series of ethanol and deionized water washes before drying in an oven at 90^{o}C for 1 hour. 6.25 mg of phenylbisboronic acid and 4.00 mg of 2,3,6,7,10,11-hexahydroxytriphenylene were placed within the vessel. 0.5 mL of 1,4-dioxane and 0.5 mL of mesitylene were added to the reaction vessel and left sealed for 30 minutes of bath sonication. After sonication, graphene containing substrates were introduced to the vessel and left in an oven at 90^{o}C for 40 minutes. The reaction vessel was allowed to cool to room temperature before removing the substrates and placing them in toluene overnight. The powder was washed with toluene and recovered via vacuum filtration. Substrates were sonicated the next day in toluene for 10 seconds and then placed in vacuum to thoroughly dry.

2.5.3 Reactive ion etching

Trion Phantom III LT RIE was used to etch substrates. The following conditions were used for etching: 300 mTorr pressure with 50 W of power and 50 sccm of O_2 flow. The process conditions were run for 27 seconds (empirically optimized). After etching, the substrates were washed with ethanol, nanopure water and ethanol again to remove residual polymer.

2.5.4 Metal nanoparticle formation

Substrates with holey graphene were soaked in 150 µL of either 1mM $HAuCl_4$ or 1mM $Pd(acac)_2$ for two hours at room temperature in the dark. After two hours the substrates were washed copiously with nanopure water and blow-dried with N_2.

3.0 Synthesis of Holey Graphene Nanoparticle Compounds

3.1 Preface

Parts of the text as well as figures were published in “Synthesis of Holey Graphene Nanoparticle Compounds” and have been reprinted with permission from *ACS Appl. Mater. Interfaces* **2020**, *12*, 36513−36522. Copyright 2020 American Chemical Society

List of Authors: David L. White, Levi Lystrom, Xiaoyun He, Seth C. Burkert, Dmitri Kilin, Svetlana Kilina, and Alexander Star

Author Contributions: DLW and AS designed the physical experiments. LL, DK, and SK designed the computational investigations. DLW, AS, and SK wrote the manuscript. DLW performed the bulk of the experimental work. SCB captured some of the electron micrographs. LL conducted the computational experiments. XH acquired the DLS and zeta potential data.

3.2 Introduction

Graphene’s intensive research effort has been justified in the numerous results generated for a variety of potential applications.[142-150] Many prominent results have been in the unique electronic properties of the layers of sp^2 carbon and their potential as electrocatalytic supports and materials.[151-159] While the incorporation of graphene oxide and reduced graphene oxide into composites with a variety of heteroatom doping has received substantial attention,[160-162] less consideration has been directed at the possibilities of materials which retain sp^2 conjugation. So-called holey graphene materials have been synthesized in a variety of routes but most commonly through the further oxidation of graphene oxide materials.[99, 100, 103, 104, 163-165] These materials have already lost sp^2 conjugation through the initial oxidation process and therefore lack some of the crucial electronic properties needed for use in functional materials. To generate the milligram scale of material needed for electrocatalytic applications while also retaining sp^2 conjugation, we have developed a synthetic procedure for the generation of high-density holes in highly ordered pyrolytic graphite (HOPG) and exfoliation of these materials into aqueous environments.

Here we present a scalable technique for the generation of holey graphene (HG) (average of 38% mass exfoliated from a given flake n = 27) derived from HOPG as demonstrated in Figure 3.1. HG is synthesized by solvothermal growth of a covalent organic framework (COF) template onto HOPG flakes followed by reactive ion etching (RIE). Production of HG by this method has several distinct advantages over current synthetic techniques. Relatively large sheets measuring micrometers in diameter are densely decorated with few nanometer sized holes imprinted from the patterned COF. Both metal nanoparticles and metal containing nanoparticles can be grown into the holes at room temperature without the use of additional reducing agents. The hypothesized mechanism for this growth is the intact conjugated sp^2 network donating electrons to facilitate reduction of the metal ions forming nanoparticles in addition to further oxidation of the holey graphene edge moieties. The patterned holes of the HG act as confining sites restricting the overall size of the nanoparticles preventing nanoparticle aggregation. The nanoparticles are held in place by the underlying HG even under the presence of high-energy electron beams (200 KeV).

Spherical size-limited nanoparticle growth is dictated by the relative ratio of metal salt precursor to HG.

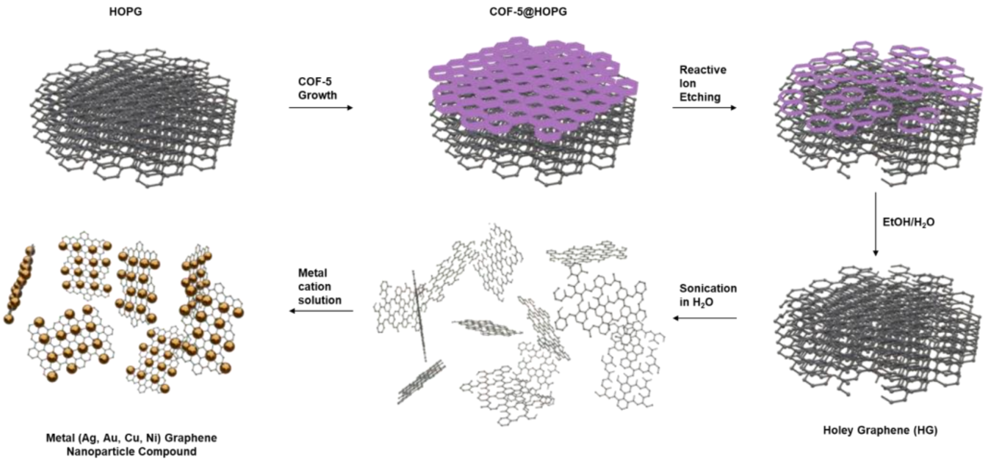

Figure 3.1 Synthesic scheme of holey graphene (HG) from HOPG and deposition of metal nanoparticles inside holes to yield graphene nanoparticle compounds (GNCs). Reprinted with permission from reference.[166] Copyright 2020 American Chemical Society

3.3 Results and Discussion

For the process of RIE-COF-5 patterning tight control over both the COF growth and RIE conditions must be considered.[167] If the ratio of hexahydroxytriphenylene to phenylbisboronic acid (HHTP:PBBA) falls outside of the precise ratio (1:3 molar ratio), the patterning is inconsistent leading to under patterning or over patterning if the HHTP is too high or too low respectively. Additionally, a wide range of RIE conditions were explored. Previously in the case of single layer graphene, we optimized hole formation based on the electronic properties (current on/off ratio) of field-effect transistor (FET) devices.[168] Here we optimize RIE conditions based on both perceived discrete hole formation in SEM as well as Raman characteristics like formation of D’ peak (1610 cm^{-1}) and relatively small D (1350 cm^{-1}) to G (1500 cm^{-1}) ratios.[124] Another consideration here is the formation of relatively deep holes inside HOPG to maximize material generated. RIE conditions can be challenging to optimize due to the relatively thin layer of COF-5 present (<100 nm), as observed in our previous investigation into single layer graphene,[168] which can be entirely removed in over-etching conditions. Optimization was initially performed with respect to RIE pressure and power while holding time constant. After identifying desired morphological characteristics from the pressure and power conditions, time was optimized to yield deepest patterning to maximize the production of material. The goal of the optimization was to optimize contiguous flake size while achieving dense and deep patterning of holey features. While two primary conditions emerged as viable, only 200 mTorr with 100 W for 30 seconds was selected for further study to limit redundancy.

The patterning of HOPG to the final composite material's physical morphology can be tracked through SEM, TEM, and AFM as shown in Figure 3.2. Dense features are present across large areas of HOPG flake and contiguous flakes that are larger than one micrometer in diameter can be identified. Exfoliation into pure water can yield substantial amount of material that are synthesis dependent. After three hours of sonication, as little at 0.1 mg/mL can go into solution and as much as 1 mg/mL can be present for the same RIE conditions. TEM observations of ten times diluted solutions can be used to evaluate the retention of patterning after exfoliation. Large flakes can still be identified in the TEM images with dense patterning of nanometer sized features (4.30 nm ± 1.52 nm, n = 83). After stirring with an optimized concentration of metal salt solution for one-hour, numerous nanoparticles can be identified. The formed nanoparticles have a relatively small size distribution (2.86 nm ± 0.66 nm, n = 43) with particle size that matches the COF hole pattern (2.7 nm) well. We expect a range of different hole pattern sizes due to the nature of the RIE patterning. Patterning in general does not yield a completely anisotropic etch profile leading to conical type etching into the HOPG flake. Therefore, HG in solution should retain material that is ranging in hole distributions which can explain the discrepancy between the material before and after nanoparticle reduction.

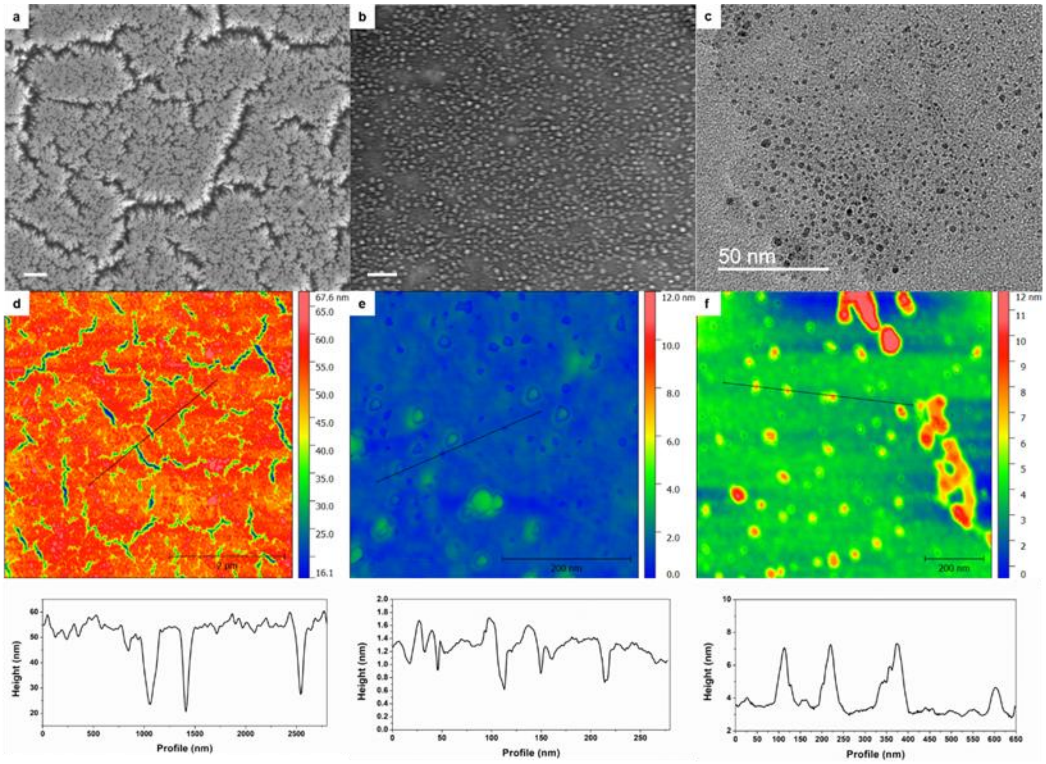

Figure 3.2 Electron microscopy and atomic force microscopy (AFM) characterization of the synthesis of GNCs. a) SEM of HOPG flake after RIE-COF-5 templated etching under optimized conditions (scale bar 200 nm). b) TEM of exfoliated HG sheet (scale bar 50 nm). c) HRTEM micrograph of HG copper nanoparticle composite utilizing optimized growth conditions (2 mg/mL of copper(II) chloride dihydrate). d) AFM of RIE-COF-5 templated etching. e) AFM of exfoliated HG sheet on mica. F) AFM of HG copper nanoparticle composite on silicon wafer. (Height profiles for each AFM micrograph displayed below the respective micrograph). Reprinted with permission from reference.[166] Copyright 2020 American Chemical Society

AFM imaging of the patterned flakes after washing the residual COF from RIE reveal correspondence between SEM and AFM imaging. While the holes show minor height differences as compared to the top of the flake the trenches formed show more than 30 nm of height difference. This indicates patterning is potentially reaching as deep as 100 layers into the HOPG, assuming

0.33 nm interlayer spacing. The primary reason that AFM imaging does not reveal more depth for the top features is the relatively small horizonal features which inhibit the tip from probing the deep features. Trenches could be viewed as non-ideal patterning, but the density of the trenches still leaves micrometer-sized flakes that are retained after exfoliation. AFM images of exfoliated sheets reveal large sheets with a wider distribution of holes then the as-patterned HOPG but still demonstrating single layer thickness. Single sheets are observed here, but most of the material formed is multilayer flakes as expected without special consideration devoted towards yielding single layer material.[169, 170] AFM images of the copper composite reveal correspondence between TEM imaging of the size distribution of the nanoparticles and the height distribution of the features observed by AFM.

Control experiments with no RIE failed to yield any exfoliation into water due to dissimilar surface energies of HOPG and water. RIE processing without COF templating yields material into water which is colloidally stable at lower concentrations but lacks the holey structure of COF-templated procedure. There are two primary differences between our synthesized material and this control experiment. For HOPG without COF-5 after RIE processing, the observed zeta potential was much larger, and the size of sheets was much smaller based on DLS and TEM. The contrast between the holey material and the RIE control is the difference between indiscriminate introduction of oxygen functionalities as compared to purposeful control of defects. While more oxygen functionalities will convey more colloidal stability, there is a lack of control in the resulting material and absence of larger sheets that are potentially useful in applications that require longer distance patterning.

Metal loading can be induced into the structures during a simple metal salt stirring procedure performed at room temperature in the dark. Precluding light is used to rule out the possibility of photoreduction reactions.[171] Introduction of nanoparticles into HG shows both concentration and time dependence. Holey graphene concentration before reactions is inferred from mass. Nanoparticle composites concentrations after reactions are determined by UV-vis absorption calibration curve. For this study we fixed the concentration of HG and varied the concentration of the metal salt. Briefly, a colloidally stable solution of HG was mixed with a range of metal salt (0.1 – 10 mg/mL) while stirring for a range of times (1 hour to 6 hours). Composites were recovered via centrifugation and washed several times with pure water to ensure removal of residual metal salt. Removal of metal salt was in general observed by UV-vis absorption spectroscopy as illustrated in Figure 3.3. We envision widespread applications in catalysis due to the strong electronic coupling present between the introduced metal species and the underlying HG.

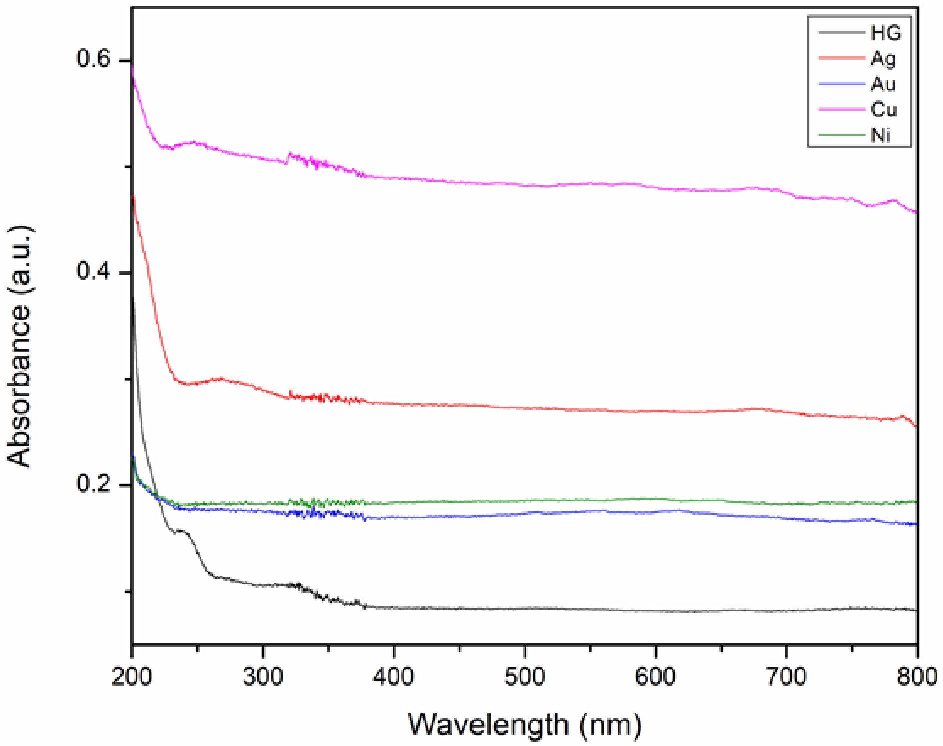

Figure 3.3 UV-vis absorption spectra of holey graphene (HG) and respective GNCs after centrifugation wash procedure. No metal salt absorption can be observed in the final products. Concentrations of the respective compounds are HG = 0.038 mg/mL, Ag-GNC = 0.119 mg/mL, Au-GNC = 0.076 mg/mL, Cu-GNC = 0.213 mg/mL, and Ni-GNC = 0.086 mg/mL. Concentrations are determined via a calibration curve for absorption at 800 nm. Reprinted with permission from reference.[166] Copyright 2020 American Chemical Society

To elucidate the strong metal coupling between the HG and the metal nanoparticles, we performed a series of high resolution XPS experiments as shown in Figure 3.4. High resolution carbon XPS reveals substantial differences of chemical moieties present in the as-exfoliated HG and each of the nanoparticle composites tested. The as-exfoliated HG shows a substantial tail at higher binding energies as compared to the based sp^2 peak at 284 eV. We attributed these to a combination of oxygen moieties including hydroxyl, carbonyl, and ether functionalities. These observations are supported by FTIR of the HG which reveals similar features. Although each nanoparticle composite shows different sp^2 shifts, the consistent decrease of the intensity of higher binding energy tail features of the main peak indicates that these functionalities are either being coordinated by or consumed in the reduction of the nanoparticles. We attribute the mechanism of nanoparticle formation to oxidation of hydroxyl type functionalities located at the edges, which is confirmed by elimination of O-H related features in the IR spectra of GNCs exhibited in Figure 3.5. This is consistent with increased reactivity of edge-based moieties of graphene[172] and other previously reported nanoparticle reductions.[173]

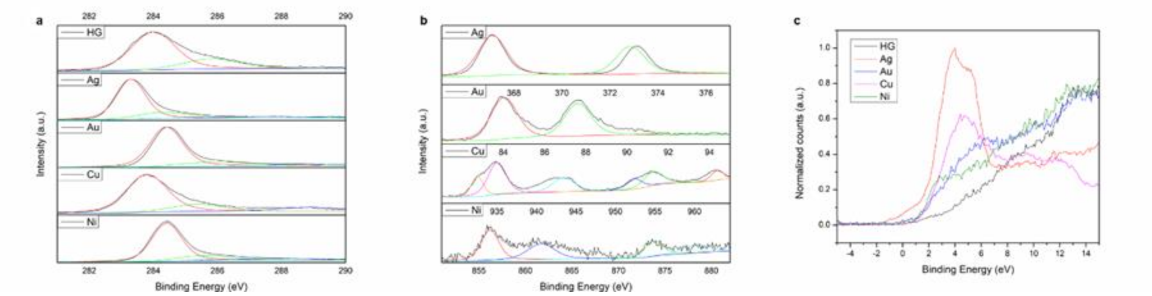

Figure 3.4 XPS of as-exfoliated HG and metal nanoparticle decorated GNCs. High resolution a) C1s, b) respective metal, and c) valence XPS scans of the HG and the different metal HG composites. Different colors in panels a) and b) represent deconvolutions of the overall signal into oxidation dependent peaks. Reprinted with permission from reference.[166] Copyright 2020 American Chemical Society

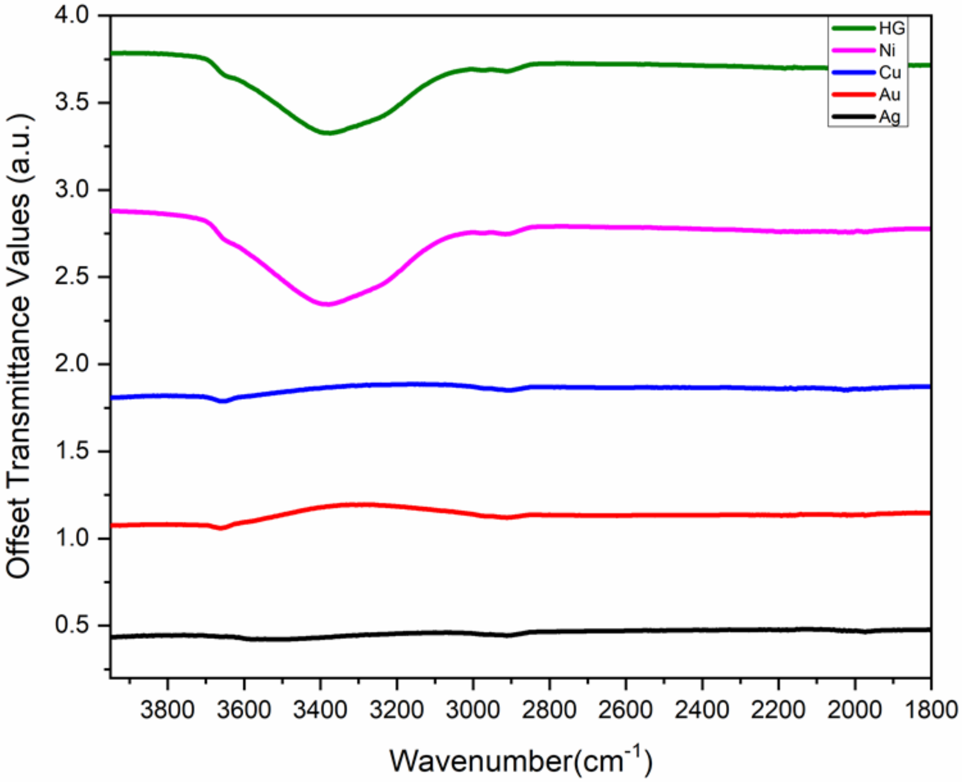

Figure 3.5 FTIR of HG and other M-GNCs on nitrocellulose filters. HG initially contains hydroxyl groups which are absent in all but the Ni-GNCs which is confirmed to be $Ni(OH)_2$ by XPS, HRTEM, and electrochemical characterization. Reprinted with permission from reference.[166] Copyright 2020 American Chemical Society

High resolution XPS of each of the relevant metal regions was taken to confirm the oxidation state and presence of the metals following the metal salt soaking procedure. Both silver and gold GNCs demonstrate the presence of metal states (with 0 charge) in the expected regions. Silver additionally shows extensive nanoparticle formation. This promising decoration indicates the potential for easily fabricated and consistent surface enhanced Raman scattering (SERS) substrates that are unfortunately beyond the scope of the current work. Copper and nickel samples have relatively more complicated spectra that cannot be fitted with single oxidation states. Although identification of copper oxidation state by XPS is somewhat ambiguous, the presence of satellite peaks at 945 and 963 eV indicate copper(II) oxide being present.[174] The shoulder in the main peak at 935 eV would indicate the presence of a secondary oxidation state that could be copper(0) or copper(I). Additional HRTEM imaging reveals the presence of copper metal as well as copper(I) oxide by lattice fringe. No copper(II) oxide lattice fringes could be observed under HRTEM. Additionally, the presence of the oxide formation in the XPS experiment could be attributed to the deposition process used to prepare the samples. The evidence indicates that the copper present is a mixed valency species that is susceptible to oxidation under mild heating (<100 °C). The presence of nickel hydroxide is confirmed by the relatively higher binding energy of the main peak at 857 eV. HRTEM of nickel GNC confirms the presence of nickel(0) lattice fringes as well but the same considerations for the copper hold here as well.

Valence XPS can be used as a tool to evaluate changes in the overall electronic structure of materials. All metal composites show different valence structure than the as-exfoliated material. Prominently silver and copper HG composites show large d electron peaks and substantial shifts in the valence band edge as compared to HG. Both gold and nickel show some shift in valence band edge although the shifts are minor by comparison. Valence band shifts as compared to initial exfoliated material indicate that there are substantial electronic changes to the overall material occurring; suggestive of strong electronic coupling between the formed nanoparticles and the underlying HG. Resultant Fermi levels of the GNCs are consistent with an averaging of workfunctions between the HG and the metal as displayed in Figure 3.6.

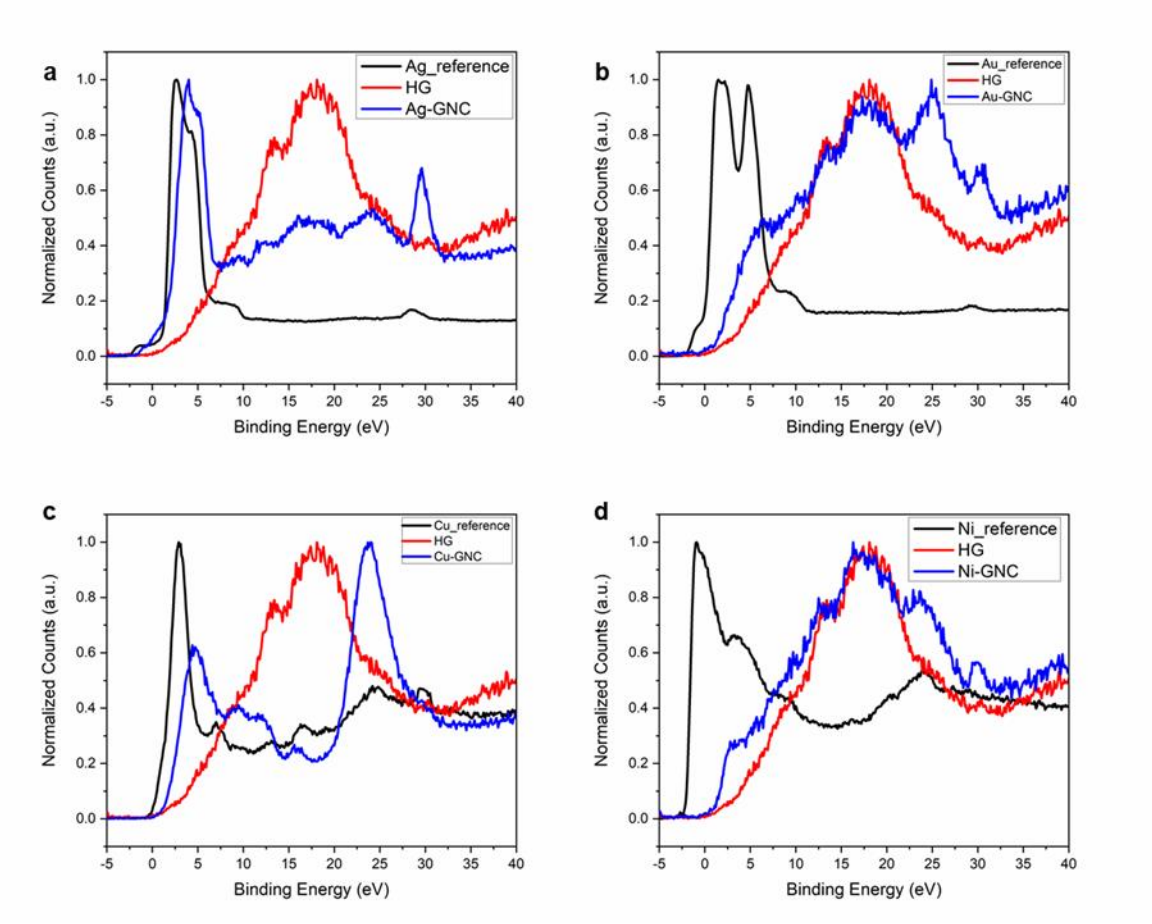

Figure 3.6 Normalized valence XPS comparison of metal references after etching samples, HG, and resultant GNCs for silver (a), gold (b), copper (c), and nickel (d). Each sample is normalized to itself to enable comparison on a similar scale. For each sample, there is a composition of peak features as well as a mixing of the fermi level as indicated by the shift of the x-intercept near zero binding energy in comparing the reference, HG, and GNCs. Reprinted with permission from reference.[166] Copyright 2020 American Chemical Society

Resulting nanoparticle size shows a sensitive metal precursor concentration dependence which is best illustrated through TEM, as displayed in Figure 3.7, but also supported through UV-vis absorption spectroscopy. Initially at higher concentrations of the metal precursor, formation of reduced structures completely overwhelms the size confining ability of the patterned holes. Overwhelming the patterned holes of all composites holds albeit with different concentrations for different metal precursors. As the concentration is decreased, nanoparticle overgrowth can still be observed but some of the size defining effect of the patterned holes can be observed as discrete structures can be resolved. Further decrease in metal precursor concentration can yield well defined nanoparticles that show little to no overgrowth. Additional decrease in metal precursor concentration shows no additional benefits and less overall nanoparticle formation at a given time point. Although these observations are for concentrations at a relatively short time point (1 hour), The overall size limiting behavior is observed for the optimized concentration persists into long time points with more complete decoration.

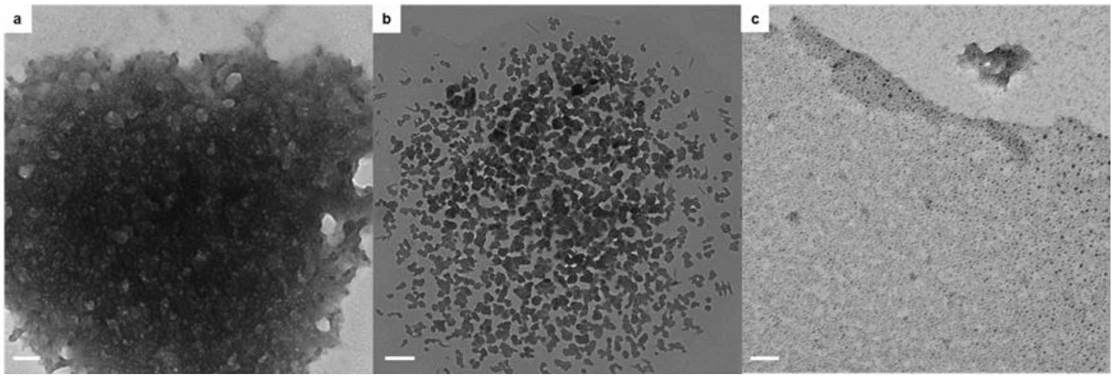

Figure 3.7 TEM micrographs of different copper HG composite syntheses at progressively lower ratios of copper(II) chloride to HG (0.146 mg/mL). a) 5 mg/mL of $CuCl_2$ HG (scale bar 100 nm). b) 2.5 mg/mL of $CuCl_2$ HG (scale bar 200 nm). c) 2 mg/mL of $CuCl_2$ HG (scale bar 50 nm). Reprinted with permission from reference.[166] Copyright 2020 American Chemical Society

HRTEM micrographs can be used to clarify the identity and oxidation state of the nanoparticles present in the composites as presented in Figure 3.8. Both more positive reduction potential metals, silver and gold, the composites show small nanoparticles with lattice spacing that can be indexed to the metal(0) oxidation state. Both single orientation of lattice spacing and multiple different lattice spacing growing together can be observed in the micrographs. Variability in lattice orientation indicates that the holes can support the growth of a single nanoparticle with a single nucleation site or multiple nucleation sites form around the hole and grow into a single nanoparticle. Although many nanoparticles are spaced relatively far apart as compared to the dimensions of the COF, there are several instances where nanoparticles are within a few nanometers of each other. Small inter-nanoparticle distances are relevant for a variety of technical applications which are currently underexplored due to the difficulty of placing nanoparticles in proximity. HG could serve as a route to these underexplored regimes. Further examination of the lattice spacing of the relatively negative reduction potential metals, copper and nickel, reveal more complex lattice spacing that cannot be attributed to single oxidation states. This behavior is somewhat expected as even if the nanoparticles were prepared in a metal (0) state, both metals are much more prone to oxidation than silver or gold species.

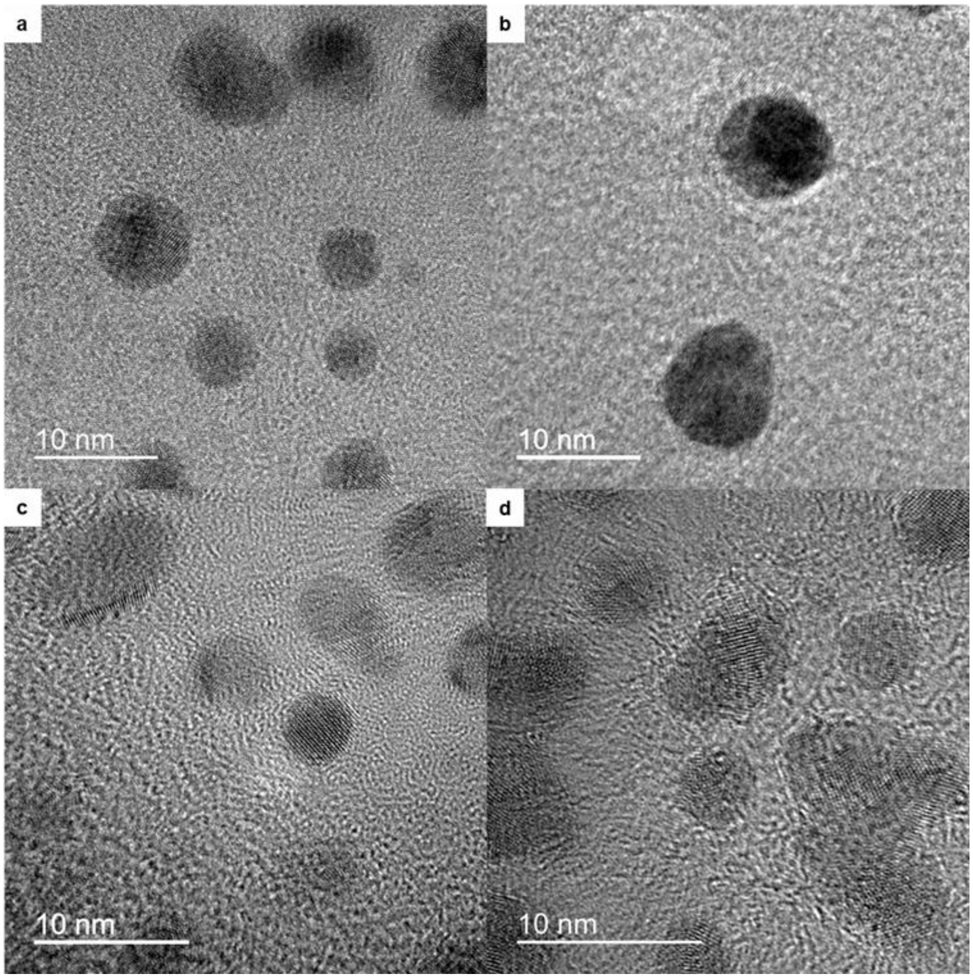

Figure 3.8 HRTEM micrographs of a) silver, b) gold, c) copper, and d) nickel decorated GNCs using optimized conditions for growth. Reprinted with permission from reference.[166] Copyright 2020 American Chemical Society

Zeta potential and dynamic light scattering (DLS) were also measured to evaluate both the stability and size distributions of both the initial exfoliated material as well as the material after metal decoration. HG is colloidally stable at lower concentrations (0.059 mg/mL concentration has a zeta potential of –30.1 ± 10.2 mV) due to the abundance of oxygen containing functional groups introduced during the RIE process. DLS reveals two distinct size distributions centered around 150 nm and 950 nm indicating a range of material in solution. Each of the other composite materials zeta potential and size distributions show somewhat different behavior as compared to the HG.

The primary distinction is the reduction of smaller size flakes and retention of a negative zeta potential albeit at varying magnitudes. The limiting of the small size distributions can be attributed to the effect of centrifugation as part of the composite synthesis. As only the pellet is resuspended, we can expect a shifting towards material that is more easily precipitated. The negative zeta potential can be ascribed to the retention of anionic salts to act as weakly bound ligands to composites nanoparticles. The relatively weakly bound nature of these ligands should ensure that they can be removed for catalytical applications as needed.

Computational investigations based on density functional theory (DFT) are used to understand the effects of inclusion of the nanoparticles in the HG and on the electronic structure of the composite. Gold clusters are chosen as the main model system, since Au-GNC samples demonstrate higher heterogeneity in their oxidation state and zeta-potential. The size of the synthesized systems is computationally prohibitive, therefore a smaller magic-size gold cluster of 13 atoms in size,[175-178] Au_{13}, is used as a simplified model of a metal nanoparticle. Au_{13} is inserted into the 1.5 nm hole at the HG, as illustrated in Figure 3.9. The lattice structure of Au_{13} perfectly fits to the geometry of the hole at the HG model. The edges of the hole at the HG model are capped by hydrogens and six carboxyl groups. It is expected that substitution of OH groups by H capping groups have a negligible effect on the electronic structure of the HG. This trend was observed for covalently functionalized carbon nanotubes (CNT), where substitution of OH groups with H at the sp^3-defect side negligibly altered the electronic structure[179,180,181] of the CNT. Calculations reveal that the HG capped with OH and 6 COOH has similar electronic features as the DOS of the HG with 6 COOH and the hydrogenated capping. Therefore, for simplicity, only the models with hydrogenated edges are used in calculations. This choice of the capping model is also rationalized by the fact that OH features in IR spectra are not resolved for Au-GNCs (see above). Therefore, it is reasonable to assume that hydroxyl groups do not contribute to the coordination of Au nanoparticle and are not expected to critically affect their electronic structure.

Due to flexibility of carboxyl groups, the Au_{13} cluster can be embedded inside the hole or slightly above the hole (at the surface), while strongly coordinated by carboxyl groups in both cases. Since carboxyl groups can be easily deprotonated in water solutions, we consider the “embedded” and “surface” structures for two cases: (i) HG with fully protonated carboxyl groups and zero charge on the metal cluster, $(Au_{13})^0/6COOH$, and (ii) HG with deprotonated groups turning to carboxylates, while the metal cluster remaining neutral, $(Au_{13})^0/6(COO^-)$. The number of deprotonated groups dictates the overall charge of the system. As such, the negative charge of deprotonated models is consistent with slightly negative zeta potential obtained experimentally for Au-GNCs.

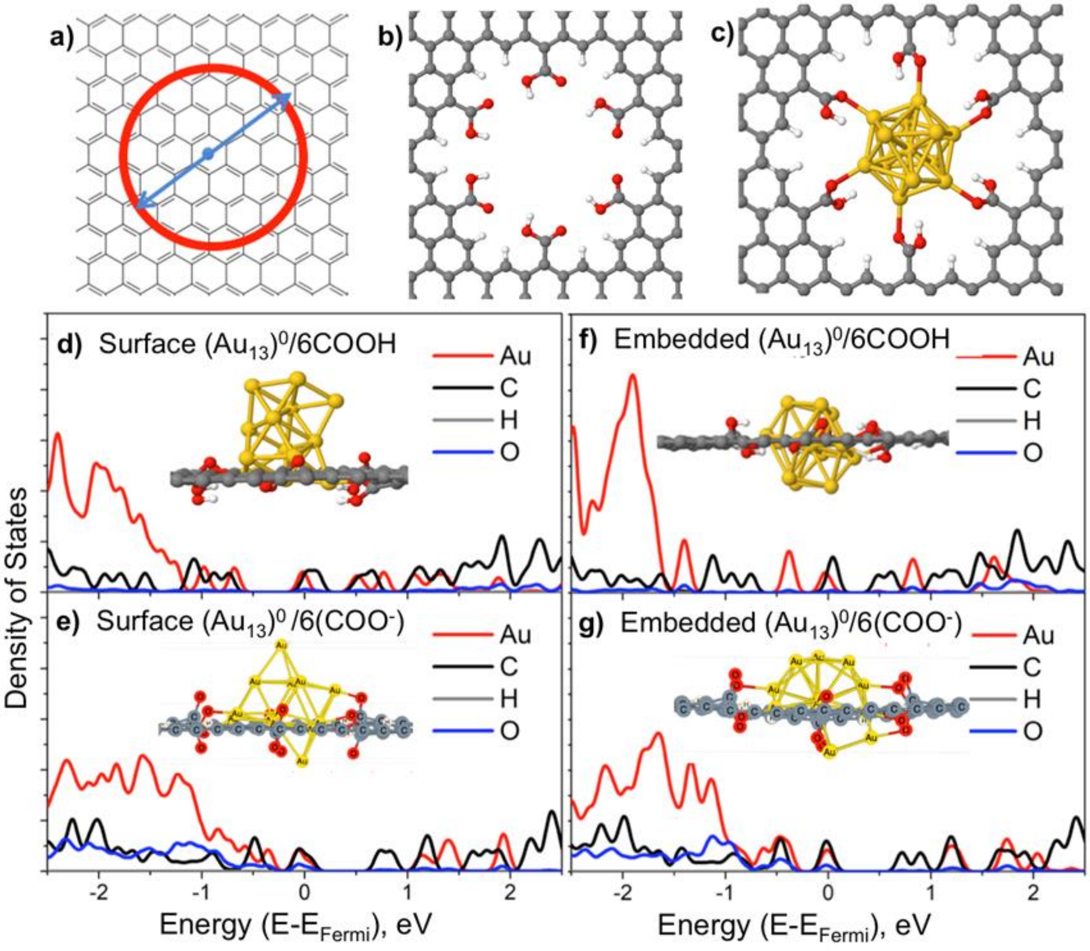

Figure 3.9 Schematic representation (a) and optimized structures of the HG model (b) and HG with the gold cluster, Au_{13}, embedded inside the hole of HG (c). The density of states (DOS) projected to the orbitals associated with carbon (black lines), oxygen (blue lines), hydrogen (grey lines), and gold (red lines) atoms of the HG with embedded $(Au_{13})^0$ coordinated with 6(COOH) (d) and $6(COO^-)$ (e) and with the $(Au_{13})^0$ at the surface of the hole coordinated with 6(COOH) (f) and $6(COO^-)$ (g). The negative charge of the whole system corresponds to the number of deprotonated carboxyl groups. Inserts show the optimized structures of the embedded and surface conformations. Reprinted with permission from reference.[168] Copyright 2020 American Chemical Society

Lower panels in Figure 3.9 show the density of states (DOS) projected on the orbitals originated from carbon, oxygen, and, metal atoms for embedded and surface structures of the neutral gold cluster coordinated with six carboxyl groups and six carboxyl groups being deprotonated. In all cases, the gold cluster introduces the metal-associated states at the Fermi energy. While these states are significantly hybridized with the carbon-originated states, the pristine HG does not exhibit states directly at the Fermi energy. The embedded protonated and deprotonated structures contribute additional Au-originated states at the edge of the VB from –0.5 eV to 0 eV. In contrast, the surface $(Au_{13})^0/6COOH$ has a well-pronounced sub-gap at this energy range. Interestingly, deprotonated carboxyl groups in the surface structure facilitate penetration of the gold cluster inside the HG, making it look more like the embedded conformation. As a result, the peaks at the VB of the surface $(Au_{13})^0/6(COO^-)$ are similar to those of the embedded $(Au_{13})^0/6(COO^-)$ system. Overall, deprotonation of carboxyl groups leads to their stronger coordination with the embedded metal cluster, which broadens and shifts the metal-associated peaks toward the edge of the VB.

Comparing these calculated results to the experimental valence XPS scans of the HG and the Au-HG composites, we can conclude that only the embedded $(Au_{13})^0$ cluster provides distinct peaks in the VB edge compared to HG, which agrees with experimental data. As such, we suggest that the nanoparticle is formed completely embedded in the hole of the HG, rather than at the surface of the hole. Second, the nanoparticle is expected to have no charge, while coordinated by fully protonated carboxyl groups. Additional calculations demonstrate that the structure with the positively charged cluster coordinated to six deprotonated carboxyl groups, $(Au_{13})^{6+}/6(COO^-)$, exhibits a sub-gap at the edge of the VB from –1 eV to 0 eV, with the metal-associated peak at the Fermi energy, which does not agree with the electronic features observed experimentally.

The calculations of the DOS of embedded $(Ag_{13})^0$ and $(Cu_{13})^0$ clusters, that were constructed in a similar manner as embedded $(Au_{13})^0$, also demonstrate a well-pronounced metal-associated peak at the edge of the VB that is distinct from the VB edge of HG. All embedded clusters show very similar VB near the Fermi-energy, while the difference in their bands become more noticeable for states deeper inside the VB, especially for d-states associated with metals. Deprotonation of all carboxylic groups coordinated with metal clusters results in a slight redshift (~0.5 eV) of the highly intensive peaks associated with metal d-d orbitals, broadening their shapes near to the VB edge. This broadening is the most pronounced for $(Ag_{13})^0/6(COO^-)$ system. Taking into account that the zeta potential of Ag-HG composites shows a wider distribution toward more negative values compared to those of Au-HG and Cu-HG, it is reasonable to assume that structures with deprotonated carboxyl groups are more frequently present in Ag-HG samples. These deprotonated structures are likely result in much more pronounced VB shoulder at the lowest energies observed for Ag-HG, compared to other composites.

To evaluate these GNCs as electrocatalytic platforms, we investigated the activity of the Ni-GNC for oxygen evolution reaction (OER) activity as shown in Figure 3.10. GNCs can serve as a platform to reduce overall metal usage, provide additional conductivity to boost catalytical activity, and reduce sintering.

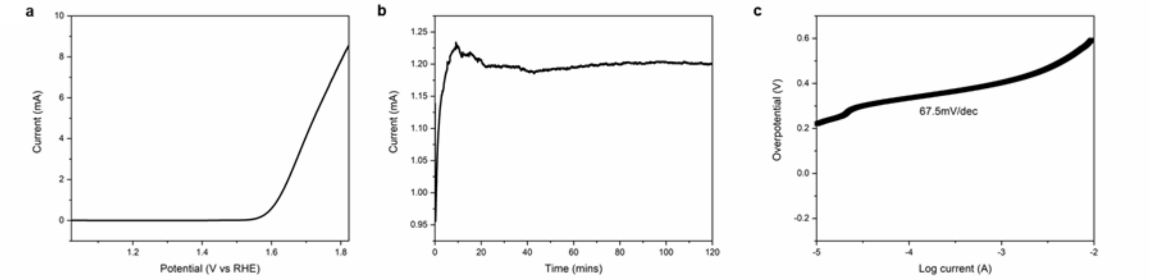

Figure 3.10 Electrochemical catalytic data for Ni-GNC toward oxygen evolution reaction (OER). a) Linear sweep voltammogram (LSV) in 1 M KOH on a rotating disk electrode @ 1600 rpm. b) Galvanostatic electrolysis of Ni-GNCs for 2 hours of continuous operation under the same conditions as LSV. c) Tafel plot of a) where the central region has been fitted. Reprinted with permission from reference.[166] Copyright 2020 American Chemical Society

Current of 5 mA can be seen at 1.7 V potential vs RHE for 80 µg of Ni-GNC deposited onto a glassy carbon electrode. Onset potential for catalysis is at 1.53 V vs RHE, on par with other $Ni(OH)_2$ based OER catalysts.[182, 183] Catalytic activity shows stability over 2 hours of continuous operation at 1.6 V vs RHE. This performance serves as indirect evidence of the stability of the nanoparticles to remain inside of the holes and avoid sintering. Tafel slope of the Ni-GNC composite is 67.5 mV/dec, the value is also consistent with other $Ni(OH)_2$ based catalysts. Electrochemical impedance spectroscopy was used to evaluate both surface area and the favorability of charge transfer after the onset potential. Equivalent circuit modeling at open circuit potential (1.28 V vs RHE) reveals large resistance to charge transfer (22570 Ohms) and 20 µF capacitance. Similar capacitances were observed under working potentials of 1.6 V and 1.7 V vs RHE but with dramatically reduced charge transfer resistance (193 and 133 Ohms, respectively). Additional confirmation of capacitance values was obtained by differential scanning of cyclic voltammetry in a 0.05 V non-faradaic window around 1.28 V vs RHE. Assuming a specific capacitance of 40 $\mu F/cm^2$ in 1 M KOH, the overall electrochemically active surface area is approximately 0.61 cm^2.[184] We attribute the relatively small area to preference for restacking during deposition on electrode as well as the presence of Nafion in the catalyst ink blocking active sites. Future studies will focus on improving the active area but are beyond the scope of this current work. Further improvements in onset potential could be induced through pre- and post-synthetic doping strategies to generate Ni-Fe hybrids.[185, 186]

3.4 Conclusions

Here we have demonstrated a facile process for production of holey graphene from HOPG via a COF-5 RIE process. The resulting material can be exfoliated into water and can have flake sizes ranging from 1 to 2 micrometers densely patterned with nanometer sized features. The material is active for a broad reduction potential range of size limited nanoparticles dictated by the relative ratio of metal salt to HG. Both metal(0) and metal oxide/hydroxide states were observed to form in an element dependent fashion without additional reducing agents. Edge hydroxyl-based oxidation is posited as the reduction mechanism as per FTIR and XPS evidence. Formed composites demonstrated strong electronic coupling between carbon and metal resulting in large changes to carbon and valence XPS of the material. Nanoparticle growth can overwhelm the hole sites at higher concentrations forming larger agglomerations. At lower concentrations metal nanoparticles can remain contained in their respective sites and cover large areas of the HG. All composite materials form metastable suspensions in water with negative zeta potentials, which we associate to the retention of anionic ligands, including deprotonated carboxyl groups at the HG edges, weakly coordinated to the nanoparticles in the composites. Computational investigations on model systems reveal a preference for embedding of nanoparticles inside the hole of the HG over their surface-based incorporation. Metal d-states are shown to contribute to the valence band of the electronic structure only for neutral nanoparticles consistent with XPS evidence. Ni-GNCs were evaluated as OER catalysts and demonstrated low overpotential of 300 mV, no degradation of current over two hours of operation, and 67.5 mV/dec Tafel slope.

3.5 Experimental

3.5.1 COF-5 growth on HOPG

COF-5 was synthesized in a procedure previously published.[168] Briefly, a thick walled glass container was cleaned and dried in an oven . A mixture of phenylbisboronic acid (PBBA) (6.25 mg, 37.7 mmol) and 2,3,6,7,10,11-hexahydroxytriphenylene (HHTP) (4.00 mg, 12.33 mmol) in 1:1 mixture of (1 total mL) of 1,4-dioxane and mesitylene was added to the container and sonicated for 30 minutes. After sonication, 1×1 cm flakes of freshly cleaved highly ordered pyrolytic graphite (HOPG, #439HP-AB from SPI Supplies, West Chester, PA) were introduced to the vessel and left in an oven at 90^{o}C for 40 minutes. The reaction vessel was allowed to cool to room temperature before removing the HOPG flakes and placing them in toluene overnight. The powder was washed with toluene and recovered via vacuum filtration. Substrates were sonicated the next day in toluene for 10 seconds and then placed in vacuum to thoroughly dry for several hours.

3.5.2 Reactive ion etching

Trion Phantom III LT RIE was used to etch HOPG flakes. The following conditions were used for etching: 200 mTorr pressure with 100 W of power for 30 seconds and 50 sccm of O_2 flow were chosen as the final conditions. After etching, the substrates were washed with ethanol, nanopure water, and ethanol again to remove residual polymer. HOPG flakes were dried in vacuum after the wash to retrieve an initial starting mass used to estimate concentration in solution.

3.5.3 Exfoliation into solution

Dried patterned HOPG flakes were massed and then placed into (2 mL) of nanopure water in a 1-dram vial. Sonication proceeded for 3 hours to attempt maximal retrieval of patterned material. After sonicating, the solution was retrieved and placed into a separate 1-dram vial for storage. The flake (if remaining) would be retrieved and dried under vacuum for several hours before massing. The mass difference between before and after sonication was used to estimate concentration in solution.

3.5.4 Nanoparticle formation

Solutions of HG were diluted to (0.292 mg/mL) and mixed with a variety of metal salt solutions at different concentrations. The following metal salts were used: ($AgNO_3$, $HAuCl_4 \cdot 3H_2O$, $CuCl_2 \cdot 2H_2O$, and $NiCl_2 \cdot 6H_2O$.) Concentrations ranged from (10 mg/mL to 0.1 mg/mL). The typical copper process was to introduce (1 mL of 0.292 mg/mL) HG to (1 mL of 4 mg/mL) metal salt solution in a 1-dram vial with a freshly cleaned stir bar. The magnetic stirrer was set at 800 rpm and the reaction was carried out in the dark at room temperature. All screening for nanoparticle decoration was conducted with 1-hour reaction while more complete coverage of nanoparticles was achieved with 6-hour reactions. After the reaction was completed, the solutions were centrifuged down for 30 minutes. The supernatant was recovered and (2 mL) of nanopure water were added for an additional two centrifugations. The later supernatants were discarded, and the final solutions were brought up in (1 mL) of nanopore nanopure water in a 1-dram vial. Optimized conditions for all metal salts were as follows: (Au) (2.5 mg/mL), (Ag) (5 mg/mL), (Cu) (4 mg/mL), and (Ni) (10 mg/mL).

3.5.5 Computational methodology

All DFT calculations were performed in the Vienna Ab-initio Simulation Package[187-189] (VASP 5.4.4) using the Perdew, Burke, and Ernzerhof (PBE)[190] exchange-correlation generalized gradient approximation (GGA) functional with projector-augmented wave (PAW) pseudopotentials[191, 192] and plane-wave basis sets at the Gamma k-point.

The supercell of HG with metal clusters is 20 Å × 21.5 Å along the x-y plane, where the z dimension varies, while providing at least 8 Å separation to minimize spurious interactions between replicas. The charge of the whole system is determined by the number of deprotonated carboxyl groups, while the charge on the metal cluster is zero. The optimization of the metal-HG systems was performed till the forces between ions were smaller than 0.01 eV/Å. All projected density of states (PDOS) calculations were performed at the Gamma-point. The $(Ag_{13})0$ and $(Cu_{13})0$ clusters were embedded in the HG with hydrogenated edges and coordinated to protonated or deprotonated carboxyl groups, similar to the created structures of the emended $(Au_{13})0$ cluster. Then the metal-HG structures are optimized at the same size supercell using the same methodology as Au-HG.

4.0 FET Size Discrimination of Carbohydrates via Conductive MOF@CNT Composites

4.1 Preface

This chapter contains work from yet unpublished manuscript.

List of Contributors: David L. White, Brian A. Day, Zachary M. Schulte, Noah Borland, Nathaniel L. Rosi, Christopher E. Wilmer, and Alexander Star

Author Contributions: DLW and AS designed the physical experiments. BD and CW designed the computational investigations. DLW wrote the manuscript. DLW and NB performed the bulk of the experimental work. ZS collected BET surface area data. BD conducted MD simulations.

4.2 Introduction

Sensing methodologies utilizing electrical conductivity as a transducing element are well developed technologies with extensive examples in gas phase,[193-197] liquid phase,[198-202] and biological sensing.[203-205] Changes are typically recorded through direct alteration of charge carrier number,[206, 207] modification of local chemical potential,[208] or alteration in local capacitance.[209, 210] Broad improvement in each of these sensing methodologies has been achieved through integration with single-walled carbon nanotubes (SWCNTs). SWCNTs are particularly well-suited to these techniques due to large surface to volume ratios,[25] superior electrical conductivity,[211] and potential semiconducting band structure.[206, 212] The advantages of SWCNTs also typically include other sensitizing chemistry to improve their selectivity.[26] However, most of these techniques degrade the performance of the nanotubes through covalent modification,[213, 214] which limits electrical properties through the generation of trap states. Non-covalent functionalization with polymers[215, 216] can also induce selectivity but limit access the surface of the nanotube, the most sensitive part of the device. Covalent and non-covalent modifications of nanotubes are limited in identifying a particular functional group or chemical feature (i.e., electron donating, electron withdrawing, or polar).

A relatively less explored area has been the rational integration of metal organic frameworks (MOF) as selective chemical layers for SWCNT-based sensors.[217] The large structural diversity of MOFs allows limitless possibilities to dictate interactions at the surface of sensors.[59] A particular advantage of MOFs combined with existing covalent chemistry on nanotubes is the wide variety of ways to control morphology of the composite through functional groups present on the nanotube and synthetic conditions. The principal advantage of MOFs when combined with non-covalent functionalization is the retention of access to the surface of nanotubes through the inherently porous structure of the MOF. Beyond improvement of sensing performance, SWCNTs provide natural structure to transmit information regarding local chemical events in the pores of the MOFs across long distances through conductivity. While electrically conductive MOFs are a rapidly growing field,[218-223] incorporating SWCNTs into MOFs provides an alternative framework to improve conductivity with minimal pore disruption, or to make nonconductive frameworks inherit additional properties.

Here we develop a methodology to discriminate chemically similar molecules (i.e., a homologous series of carbohydrates) based only by size as illustrated in Figure 4.1. By rationally integrating an existing conductive water stable MOF (Cu_3HHTP_2)[219] with SWCNTs, we demonstrate changes in field-effect transistor (FET) composites that correlate with a filling of the pores of the Cu_3HHTP_2. Differential growth of Cu_3HHTP_2 on unoxidized SWCNTs versus oxidized nanotubes (ox-SWCNTs) is observed, as well as a dependence on electrical conductivity correlated with mass loading of nanotubes. As the size of the carbohydrate molecule is reduced larger and larger decreases in current can be observed because of decreased gate capacitance. For the smallest sugar, glucose, we observed concentration dependent decreases in conductance at the most negative applied gate voltage with limits of detection in the single digit micromolar region.

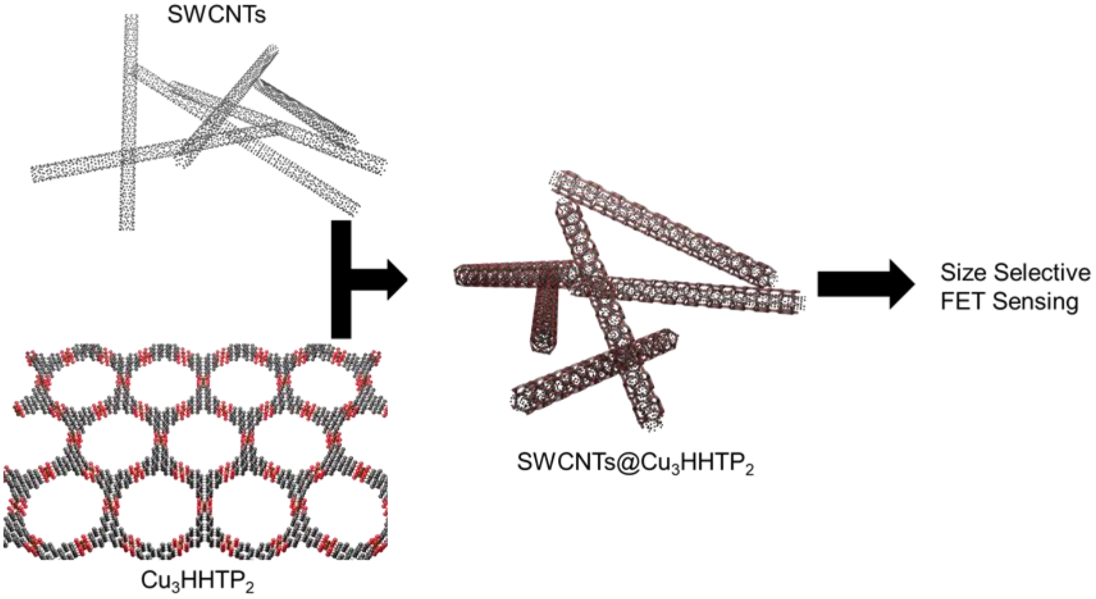

Figure 4.1 Illustration of the synthetic strategy utilized to achieve size selective sensing through synergy between Cu_3HHTP_2 and SWCNTs.

4.3 Results and Discussion

We synthesized Cu_3HHTP_2 in a solvothermal mixture of water and dimethylformamide (DMF) by slightly modifying the previously reported procedure.[224] DMF was used as the solvent to suspend the nanotubes due to the favorable matching of surface energies.[225] Both SWCNTs and ox-SWCNTs were used to pursue functional composites. Our previous work[217] had centered primarily around ox-SWCNTs due to the presence of carboxylic groups to act as nucleation sites for the formation of MOF. Herein we find that SWCNTs work better for the construction of FET sensors and are more amenable for dielelectrophoresis (DEP).

A variety of nanotube to Cu_3HHTP_2 ratios were initially explored but final devices were focused on larger quantities of nanotubes (5% theoretical loading by mass) due to more favorable electronic behavior. Devices below 4% loading would commonly fail to generate devices. ox-SWCNTs failed to yield consistent devices until 10% loading was utilized. Physical morphology characterization of the formed composite materials was conducted utilizing electron microscopy demonstrated in Figure 4.2. SWCNT composites show relatively complete covering of nanotubes indicating the interaction is governed by pi-pi interactions most clearly seen in Figures 4.2 a-c. In contrast, ox-SWCNTs based composites with same initial mass loading, show more clustered Cu_3HHTP_2 formation with numerous instances of bare nanotubes displayed in Figure 4.2.d-f. In both cases, no free Cu_3HHTP_2 was observed unassociated to nanotubes.

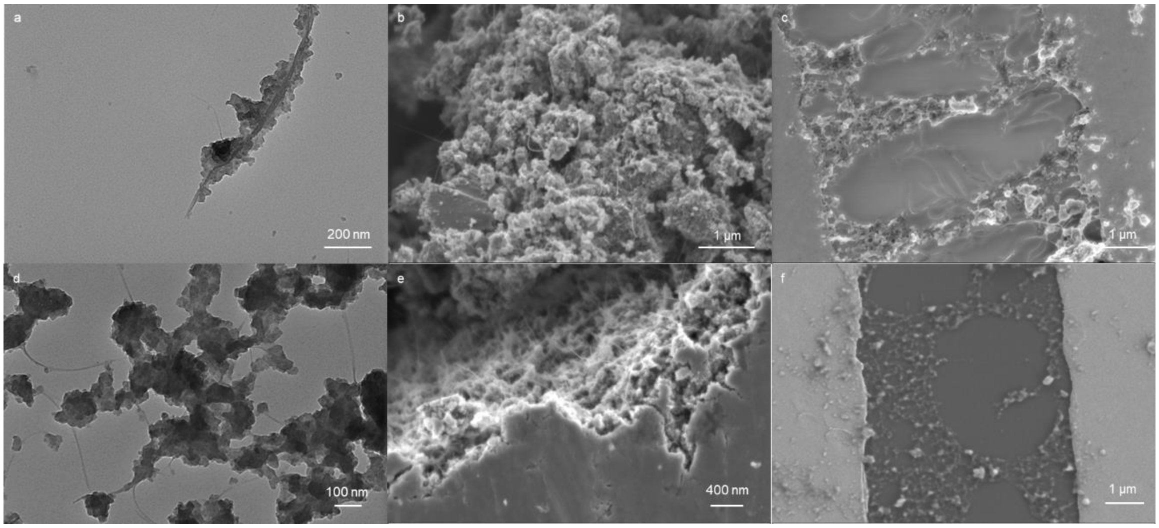

Figure 4.2 Electron microscopy of SWCNTs@Cu_3HHTP_2 composites. a) SWCNTs@Cu_3HHTP_2 with 5% mass loading of CNT on carbon backed TEM. b) SWCNTs@Cu_3HHTP_2 in powder form with clear nanotube dispersal throughout the structure. c) SWCNTs@Cu_3HHTP_2 deposited onto prefabricated devices with interdigitated gold electrodes. d,e,f) Similar micrographs as a,b,c but with ox-SWCNTs@Cu_3HHTP_2 instead of SWCNTs@Cu_3HHTP_2

Observed SEM powders reveal homogeneous structure with intermixing of nanotubes and Cu_3HHTP_2. Tuning the mass loading alters the observed density of nanotubes. Nanorod morphology is attenuated as compared to previous reports[218] but this is attributed to large amounts of co-solvent. Nanorod morphology is more pronounced in lower nanotube concentrations due to reduction of co-solvent volume. Cu_3HHTP_2 synthesized without nanotubes still lack clear nanorod morphology. This indicates that absolute presence of co-solvent is more critical for perturbing the nanorod morphology formation rather than the relative amount.

Suspending powders in DMF by sonication with subsequent deposition onto interdigitated electrodes via dielectrophoresis (DEP)[226] yields structures that more closely resemble observed TEM than bulk powders. Sonication has been shown not to affect the overall microcrystalline structure even after 72 hours. Cu_3HHTP_2 coverage on top of nanotubes is dense but not complete by simple observation. Retention of composite attachment through DEP processing and sonication indicates both pi-pi interactions and carboxylic groups have strong interactions to support composite materials through processing. DEP was chosen over previously used dropcasting to ensure thin layers of composite which are more amenable to liquid based FET measurements and are more easily subjected to liquid electrolyte gating.

Raman Microscopy was utilized to understand the interface of Cu_3HHTP_2 on nanotubes both in terms of the relative presence or absence of peaks as well as shifting of known peaks displayed in Figure 4.3.a. Raman spectroscopy of carbon nanomaterials is a well-developed field,[227] allowing for facile comparison of the Cu_3HHTP_2 growth. Analysis of Cu_3HHTP_2 powders with and without nanotubes reveal a complicated spectrum with the bulk of the features occurring between 1200 and 1600 cm^{-1}. The prominent features present in both nanotube composites are the radial breathing mode at ~150 cm^{-1} and the 2D peak present at 2670 cm^{-1}. Minor redshifting of the RBM is observed in the composite, indicative of additional mass present on the nanotubes.[228] Typical analysis of relative D (1350 cm^{-1}): G (1600 cm^{-1}) ratios are precluded by the presence of Cu_3HHTP_2 vibration modes. Difficultly in achieving DEP deposition of ox-SWCNTs composite at similar mass loadings frustrates a comparative analysis of SWCNTs and ox-SWCNTs Raman peaks on silicon devices

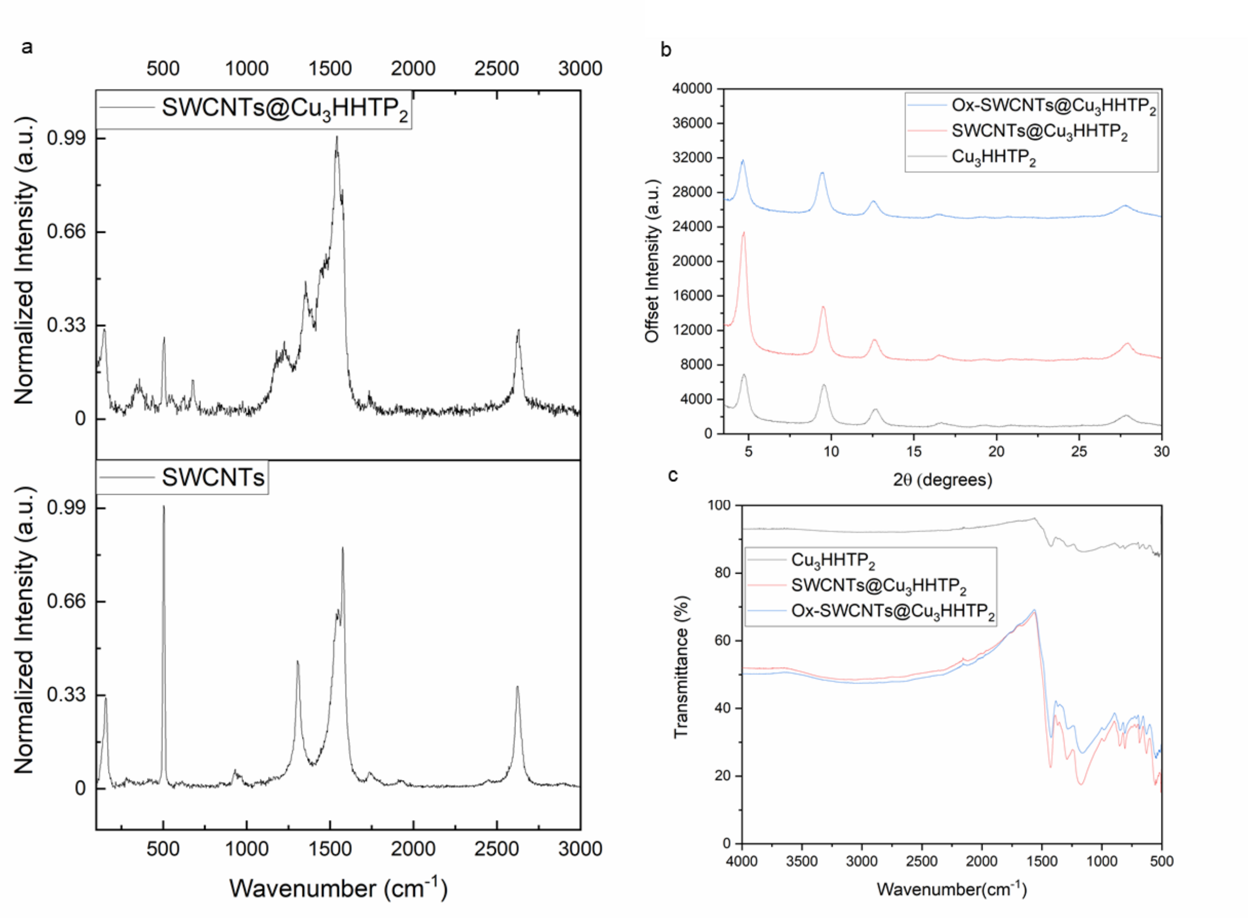

Figure 4.3 Raman spectroscopy, XRD, and FTIR spectroscopy of Cu_3HHTP_2, SWCNTs@Cu_3HHTP_2, and ox-SWCNTs@Cu_3HHTP_2. a) Raman spectra for bare SWCNTs and SWCNTs@Cu_3HHTP_2 deposited on prefabricated silicon devices. b) Stacked PXRD spectra for each of the different nanotube composite as well as Cu_3HHTP_2 without nanotubes. c) FTIR spectra for each of the different nanotube composite as well as Cu_3HHTP_2 without nanotubes.

Comparisons of microcrystalline structure through powder X-ray diffraction (PXRD) show minor variations depending on the presence of nanotubes via Figure 4.3.b. In particular, the presence of SWCNTs shows larger relative growth of the 100 plane over other observed peaks. The 100 plane is primarily associated with the main pore presence in the structure and is suggestive of favorable growth of Cu_3HHTP_2 on pi surfaces as compared to carboxylic groups. Both Cu_3HHTP_2 as well as the ox-SWCNTs composite show expected peaks with minimal deviation from the known crystal pattern. The presence of carboxylic groups therefore does not impede the growth or substantially alter the microcrystalline structure.

FTIR was used as a complementary technique to evaluate changes in MOF structure upon addition of nanotubes as shown in Figure 4.3.c. No differences in observed peaks were observed between the three cases of Cu_3HHTP_2, SWCNTs@Cu_3HHTP_2, and ox-SWCNTs@Cu_3HHTP_2. Observed spectra match previous reports[219] and indicated minimal effects of incorporation of nanotubes on the overall MOF structure.

UV-vis absorption spectroscopy recapitulates the trend observed in XRD. As the proportion of nanotubes as well as co-solvent is increased, smaller and smaller amounts of Cu_3HHTP_2 growth can be observed as considered by a UV peak attributed to hexahydroxytriphenylene and a visible peak attributed to the coordinated Cu species.[229] As UV-vis samples are prepared through post-synthetic suspension of known masses, the spectra represent insight into the relative proportion of Cu_3HHTP_2:CNT. Both Cu_3HHTP_2 as well as ox-SWCNTs@Cu_3HHTP_2 show relatively similar proportions as evaluated by peak height. This holds both as function of co-solvent volume as well as time. SWCNTs@Cu_3HHTP_2 shows comparatively higher growth as measured by peak height for the same measures as seen in Figure 4.4.

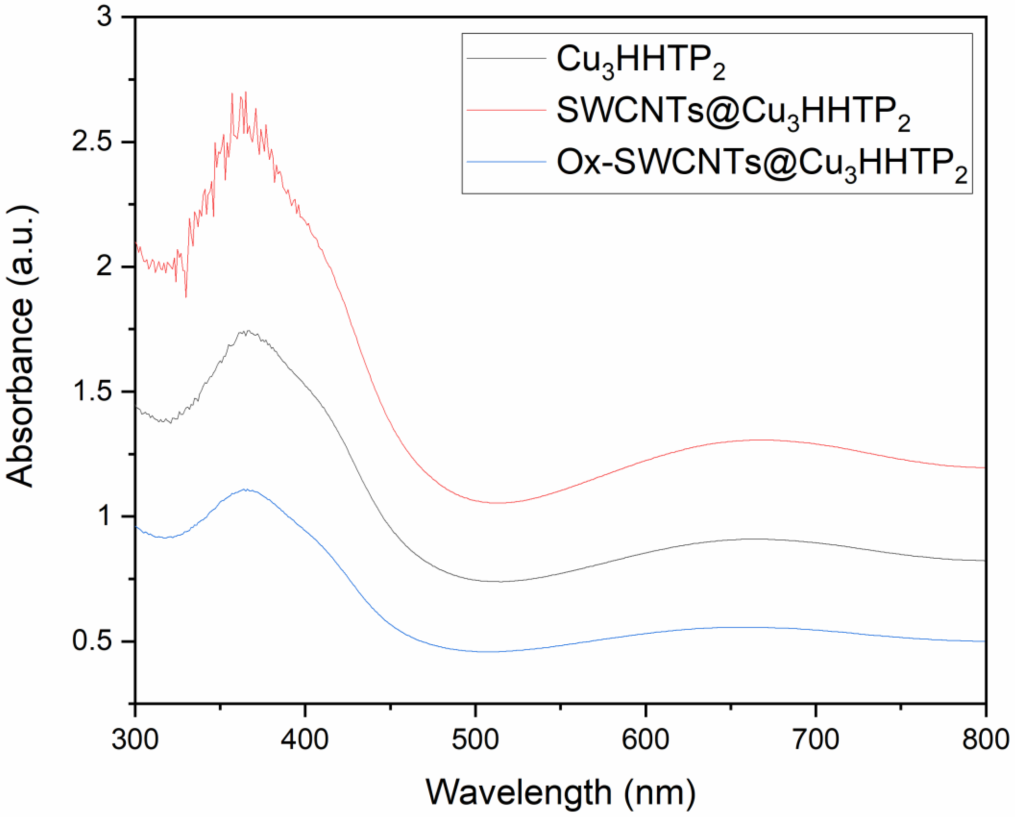

Figure 4.4 UV-vis absorption spectra of suspended $SWCNTs@Cu_3HHTP_2$ composites and Cu_3HHTP_2 prepared at 0.1 mg/mL in water.

BET surface area measurements were also conducted for each of the different nanotube composite as well as Cu_3HHTP_2 without nanotubes as demonstrated in Figure 4.5. All the N_2 isotherms demonstrated type-I adsorption behavior with no hysteresis.[230] BET surface area was somewhat lower than previous reports (~520 m^2/g)[224] with Cu_3HHTP_2 having a surface area of (279.49 ± 0.26 m^2/g). $SWCNTs@Cu_3HHTP_2$ with the largest surface area (419.01 ± 1.04 m^2/g), and ox-$SWCNTs@Cu_3HHTP_2$ having a similar surface area to just the MOF alone (262.52 ± 0.68 m^2/g). We attribute this reduced surface area to relative short synthetic time (2 hours) as compared to previous synthesis (18 hours). The larger surface area of $SWCNTs@Cu_3HHTP_2$ composite is attributed to increased peak intensity observed in both UV-vis as well as PXRD. This also indicate a potentially interesting structure directing effect or lower energy growth mechanism that could be leveraged for future applications. This is beyond the scope of the current work.

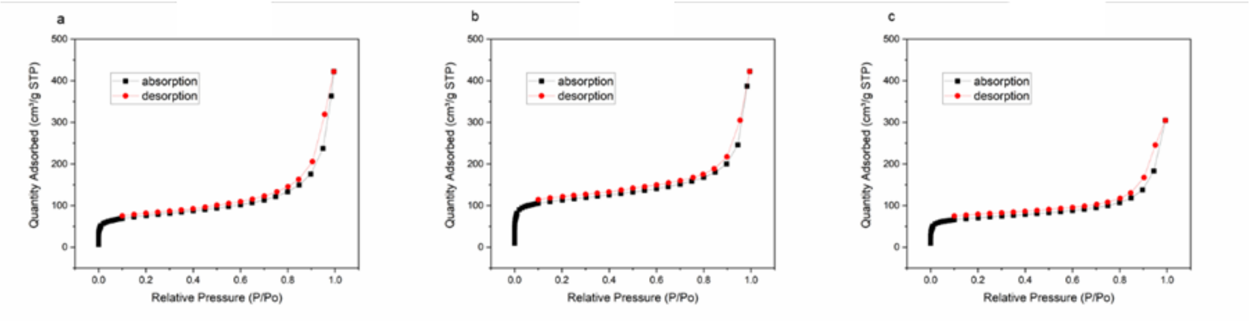

Figure 4.5 Nitrogen isotherms collected at 77K for a) Cu_3HHTP_2 b) SWCNTs@Cu_3HHTP_2 with 5% loading by mass and c) ox-SWCNTs@Cu_3HHTP_2 with 5% loading by mass.

Composites of Cu_3HHTP_2 with carbon surfaces[224] have been made before but to the best of our knowledge this has not been applied to SWCNTs. SWCNTs are particularly attractive from a FET sensing perspective due to the presence of semiconducting nanotubes. As-synthesized SWCNTs have a proportion of metallic nanotubes (1/3) which limits the usefulness in FET applications as metallic tubes are not easily modulated by an external charge environment. We note here in similarity to other efforts by our group,[217] that MOF growth on top of the nanotubes suppresses the metallic aspects of the present nanotubes. This gives strong evidence for either complete wrapping of nanotubes to prevent traditional electrical contact or at a minimum a percolation theory threshold[231] that is not exceeded. It has previously been noted that vary dilute networks of unsorted SWCNTs can have more semiconducting nature even with the presence of metallic nanotubes. This can be rationalized as a decreasing quantity of metallic nanotube junctions which increase the overall resistance of the nanotube network. By including an additional material, Cu_3HHTP_2, again the quantity of these nanotube junctions is lowered, and a more semiconducting network is established. Additional considerations for making devices here include a preference for DEP as compared to drop casting to achieve much thinner films which is more reliably gated in liquid electrolyte. Device fabrication was also considerably improved by utilizing DMF as the solvent for the suspension instead of H_2O. We hypothesize that this due to relative lowering of the dielectric constant which means less effect screening of the AC field and consequently more force to pull the composites to the surface.

At higher relative concentrations of Cu_3HHTP_2 to nanotube, devices cannot achieve sufficient electrical contact between the metal electrodes to make viable FET devices. This indicates a percolation mechanism governing the overall electric properties of the composite material. At the two highest concentrations (5 and 10% respectively) explored, good devices with tens to hundreds of microamps in on current can be manufactured utilizing unoxidized nanotubes. Oxidized nanotubes generate consistent devices only at 10% mass loading demonstrated in Figure 4.6.

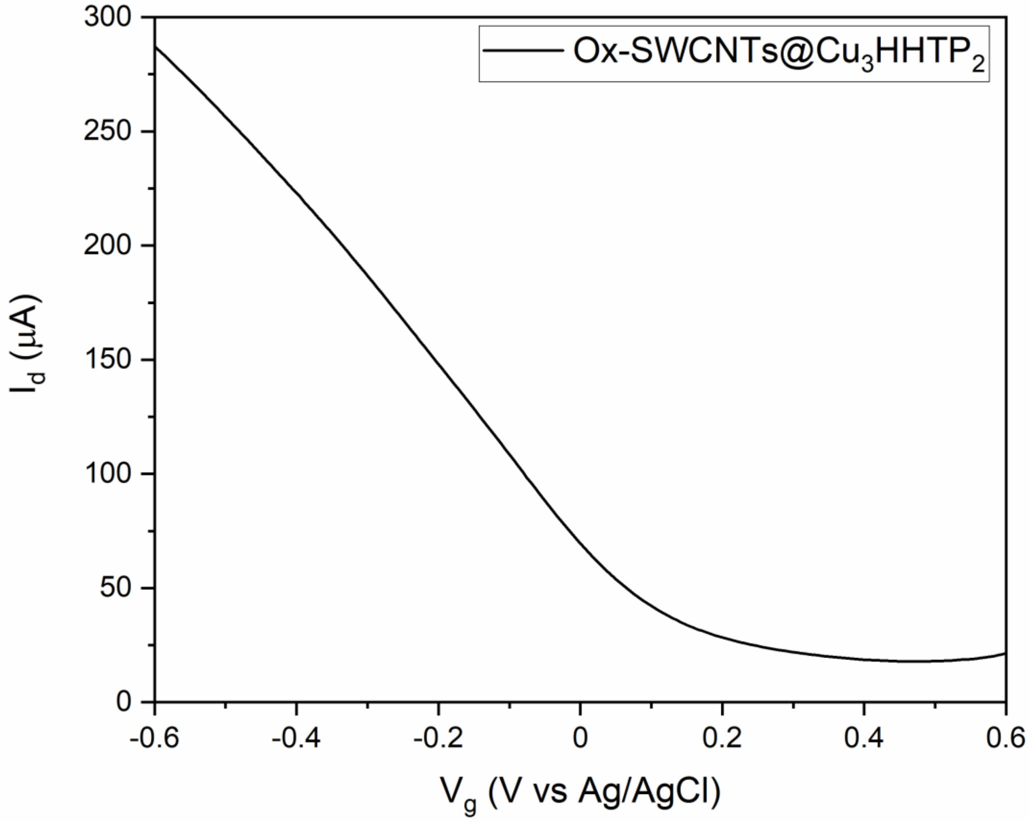

Figure 4.6 FET curve of ox-SWCNTs@Cu$_3$HHTP$_2$ composite with 10% by mass loading. Substantial increases in current are observed.

This difference in the electrical properties of the devices points to key differences in how nanotube functionalization affects the orientation and overall properties of the resulting devices. We chose to focus on unoxidized nanotubes for electrical device testing to have multiple loadings to compare initial sensing results against. Without salts present in the gating solution, devices show relatively poor gate modulation of the current. Introduction of 100 mM KCl dramatically improves the gating performance with on/off current ratios typically exceeds 20. Current on/off ratios for SWCNTs are typically beneath one unless devices are sparsely generated. Off current is dictated by the CNT junction resistance and the presence of metallic nanotubes.

We explored the sensing of a homologous series of glucose monomers including glucose, maltose, maltotriose, α-, β-, and γ-cyclodextrin as a test case for size selective sensing as indicated in Figure 4.7. FET sensing is typically modulated by the presence of small molecule chemical moieties which affect the overall chemical potential of the device.[232] Distinguishing analytes is typically conducted by choosing materials which have radically different chemical character (either electron donating, electron withdrawing, polar, or preferential interaction with the surface). Here we demonstrate differentiate solely based on size of analyte molecules instead of chemical functionalities present. The proposed mechanism for this sensing is the clogging of pores by smaller carbohydrates of the series which inhibit the transport of ions to the surface of the nanotubes altering the gate capacitance of the composite.[233]

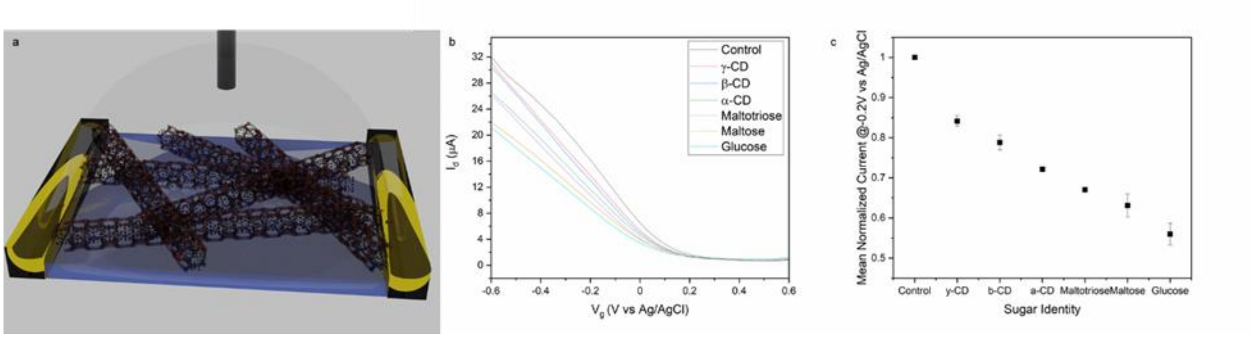

Figure 4.7 Liquid Gated FET demonstrating size selective changes in current. a)Illustration of Liquid FET sensing using Cu_3HHTP_2@ SWCNTs. b) FET curves with different size carbohydrates measured serially in constant ionic strength. c) Mean±SD current for (n=3) devices displayed in panel b. Devices are normalized to current with no sugar present @ –0.2V vs Ag/AgCl

Measuring different carbohydrates at equivalent concentrations (500 µM) in the same ionic strength KCl solution reveals a decreasing current on the p-branch of the nanotubes as the size of the sugar molecule is decreased. Larger sugars, which should not necessarily enter the pores, also affect the capacitance indicating that gaps in Cu_3HHTP_2 coverage on the SWCNTs. Sugars interacting with bare SWCNTs also block the transit of ions to the surface. This trend holds across different synthetic runs and even after several months in solution before deposition onto devices. Bending of the curve in this manner is equivalent to a reduction in gate capacitance. Additional titration measurements reveal a concentration dependent reduction of current in the p-branch for glucose. Limits of detection are in the single digit micromolar range made by evaluating the conductance at –0.4 V vs Ag/AgCl as shown in Figure 4.8. Making evaluations at the most negative gate voltage results can lead to spurious results due to effect of changing ionic strength in a titration experiment. The observed decrease in p-branch current is on a time scale similar to the length of the measurement as no change is observed at the highest concentrations for repeated measurements after five and ten minutes.

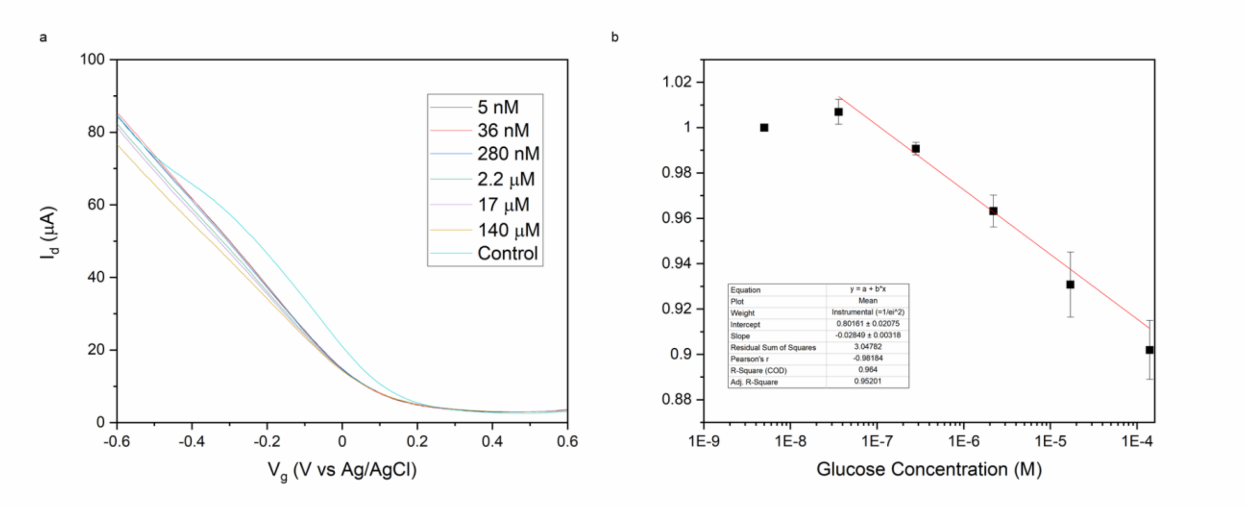

Equation	y = a + b*x
Plot	Mean
Weight	Instrumental (=1/ei^2)
Intercept	0.80161 ± 0.02075
Slope	-0.02849 ± 0.00318
Residual Sum of Squares	3.04782
Pearson's r	-0.98184
R-Square (COD)	0.964
Adj. R-Square	0.95201

Figure 4.8 Glucose titration and calibration curve. a) FET of Glucose titration on SWCNTs@Cu_3HHTP_2 device. Concentration dependent bending of the curve can be observed at higher glucose concentrations. b) Glucose calibration curve based on changes in conductance at –400 mV vs Ag/AgCl. Linear fitting is only attempted on five rightmost data points.

Further confirmation of size selective sensing can be ascertained from running titrations without washing off devices in between measurements. Initial introduction of glucose followed by other sugars in ascending sequence of size yields the largest current decrease with glucose. The addition of other sugar solutions decreases the overall concentration of glucose in the solution increasing the observed current but is still differentiable from the measurements made in the absence of sugar in each case. Titration experiments running from the largest sugar unit, γ-CD, to the smallest, glucose, reveal similar trends in current. The lowest current for the p-branch is always with the glucose testing revealing a size selective behavior for the response in the FET curve. Consistence in observe minimal current is strong evidence for the filling of the pores of Cu_3HHTP_2 as a dominant mechanism in modulating gate capacitance.

No trend in gate modulation is observed in SWCNTs deposited on a device indicating the crucial presence of the MOF as displayed in Figure 4.9. If the relative concentration of the nanotubes is increased to 10%, the observed effect is decreased, indicating that the thickness of the Cu_3HHTP_2 also crucially modulates the effect. Higher ratios of Cu_3HHTP_2 to SWCNTs induce less favorable electronic characteristics. We therefore have optimized around an intermediate loading of 5% to achieve maximal sensing response without sacrificing conductivity. Minimal change is observed upon simple dilution of the solution indicating the presence of the sugar units as crucial to achieve observed gate modulation.

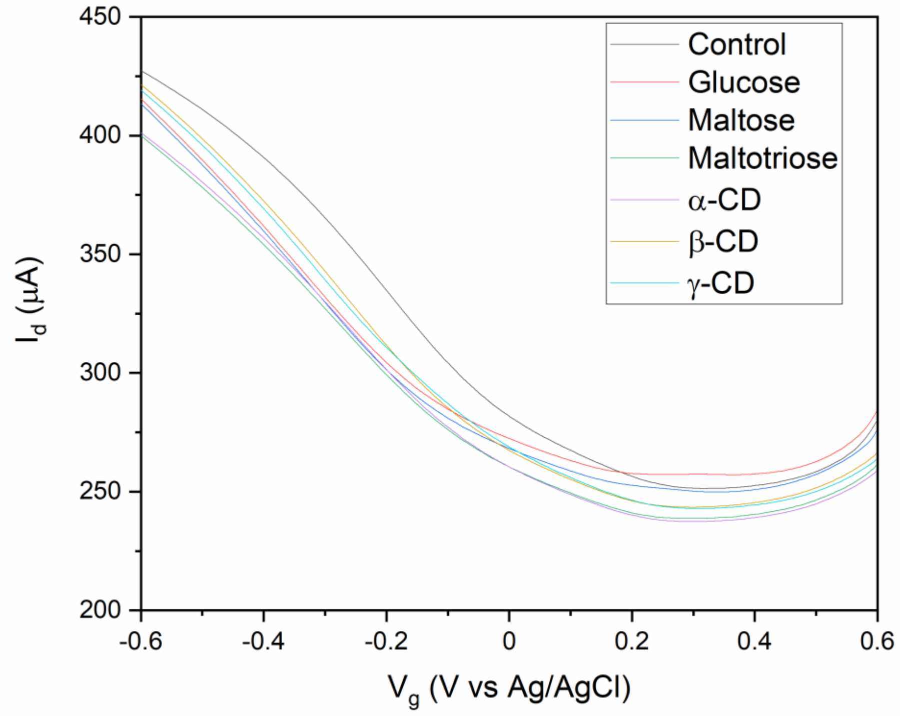

Figure 4.9 FET titration experiment without Cu_3HHTP_2 as a selective sensing layer for SWCNTs. No clear trend is size can be made.

Sweeping gate voltage in the opposite direction yields similar differentiation between the presence and absence of glucose. Repeated scans in the reverse direction also show minimal differences in current indicating that the initial pore filling process is rapid and observed behavior is not a transient effect. Additional FET measurements with a slower gate voltage sweep show decreased current indicating that the capacitance is indeed reduced and the observed reduced capacitance is minimally affected by the rate at which the gate voltage is swept.

In the interest of understanding the effect of ionic strength on the measurements, we performed additional experiments with and without glucose presence in solutions with increasing ionic strength as illustrated in Figure 4.10. As ionic strength is increased, both threshold voltage shifts to more negative potentials and well as higher current at the most negative gate voltages are observed. To demonstrate the relative effect of glucose in different ionic strength environments we plot the current observed at –200 mV vs Ag/AgCl reference for a range of ionic strengths from 1 mM to 1 M in order of magnitude steps. The observed effect in the presence of glucose is a decreasing change in slope indicative of lower ionic strength due to pore blocking.

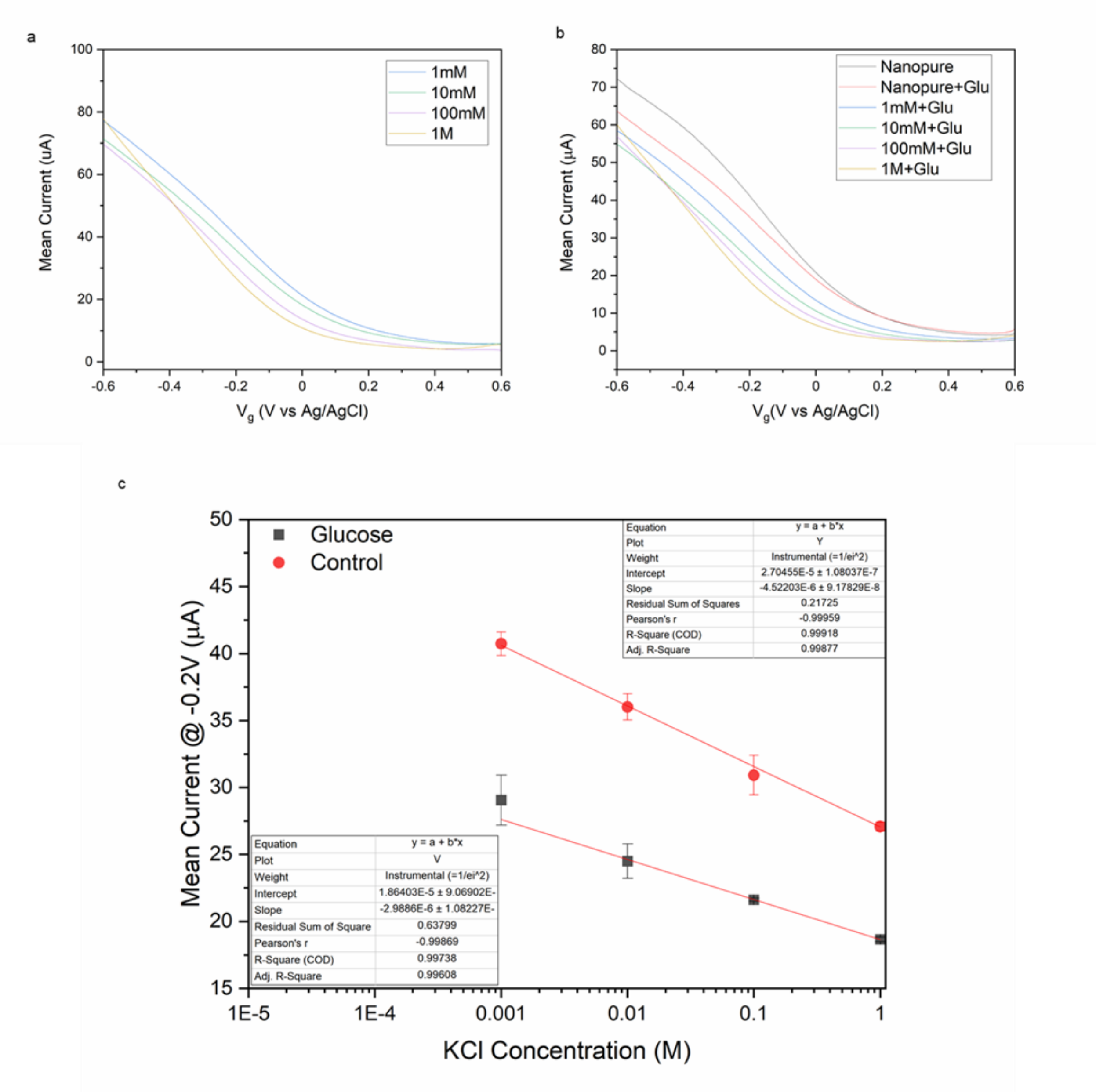

Equation	y = a + b*x
Plot	Y
Weight	Instrumental (=1/ei^2)
Intercept	2.70455E-5 ± 1.08037E-7
Slope	-4.52203E-6 ± 9.17829E-8
Residual Sum of Squares	0.21725
Pearson's r	-0.99959
R-Square (COD)	0.99918
Adj. R-Square	0.99877

Equation	y = a + b*x
Plot	V
Weight	Instrumental (=1/ei^2)
Intercept	1.86403E-5 ± 9.06902E-
Slope	-2.9886E-6 ± 1.08227E-
Residual Sum of Square	0.63799
Pearson's r	-0.99869
R-Square (COD)	0.99738
Adj. R-Square	0.99608

Figure 4.10 FET curves of SWCNTs@Cu_3HHTP_2 composite at 5% loading by mass in increasing ionic strength environments. Each measurement was made in triplicate to yield mean curves displayed here. a) Without

glucose and b) with glucose. c) Comparison of current at –200 mV vs Ag/AgCl in increasing ionic strength environments.

4.4 Conclusions

Here we present a methodology for size selective sensing of sugars utilizing SWCNTs@Cu_3HHTP_2 hybrids. We have demonstrated changes in resulting morphology, microcrystalline structure, and surface area conditional upon the presence of carboxylic groups on the surface of nanotubes as well as absolute quantity of co-solvent present in the synthesis. Only larger relative loadings of nanotubes (>5% by mass) yield well-behaved electrical devices which can be deposited on interdigitated electrodes via DEP. Lack of carboxylic groups enables deposition at lower mass loadings for the resulting composites. As-deposited composite materials show enhanced semiconducting characteristics as compared to unfunctionalized nanotubes evidenced by improved current on/off ratios.

FET devices show size dependent changes in current dependent on the size of the sugar unit for a homologous series of carbohydrates ranging from eight glucose units to one unit. Glucose shows the largest decrease in current due to pore filling which alters the gate capacitance. Current is modified for in the presence of glucose in a linear fashion dependent on the concentration. Titration of FET devices from either largest to smallest or vice versa yields the lowest current for glucose. Measuring in a series of increasing ionic strengths, the presence of glucose shows smaller changes in current at –200 mV indicating the effect of glucose as alteration of the capacitive strength of the environment.

We believe the sensing methodology presents a new way to evaluate molecules in complex environments and provides a way to reliably discriminate on the basis of size. MOF composites with SWCNTs remain a nascent field and the potential structural diversity of MOFs would enable large ranges of sizes to be explored. This work represents several important advances in demonstrating size selective FET sensing, development of synthetic methodology to combine MOFs with carbon nanotubes, and improved SWCNTs@MOF composite device manufacture.

4.5 Experimental

4.5.1 Suspension of carbon nanotubes

For composites, either unoxidized single-walled carbon nanotubes (SWCNT, P2 Carbon Solutions) or oxidized single-walled carbon nanotubes (ox-SWCNT, P3 Carbon Solutions) were prepared into 0.1 mg/mL solutions of DMF. DMF solutions were sonicated for one hour to suspend nanotubes yielding a dark black solution. Suspended nanotubes were centrifuged for 30 mins at 3000 rpm to remove large aggregates and bundles. 90% of the supernatant was recovered and used for the Cu_3HHTP_2 synthesis. A small aliquot of both the SWCNTs and ox-SWCNTs were taken to measure UV-vis characteristics. Concentrations of nanotubes used for the synthesis were normalized according to the observed intensity at 550 nm.

4.5.2 Cu_3HHTP_2 growth with and without carbon nanotubes

Cu_3HHTP_2 was synthesized from a previously published adapted procedure. For small scale syntheses to investigate the effects of mass loading of nanotubes, the following conditions were used. 8 mg of copper(II) acetate monohydrate and 6.5 mg of 2,3,6,7,10,11-hexahydroxytriphenylene (HHTP) were massed and placed into either a 1 dram vial or 20 mL scintillation vial. Mass loading of nanotubes was controlled by changing the volume of the reaction. For instance, in the case of 0.5% loading, 0.5 mL of the previously generated suspended nanotube DMF solution was added to 0.5 mL of deionized water along with the copper and HHTP precursors. This mixture was sonicated for 20 minutes and then placed into an oven at 85 ^{o}C for two hours. The reaction mixture was removed and allowed to cool to room temperature. The result mixture was washed three times with both H_2O and acetone and the final product was left to dry in a vacuum oven at 65 ^{o}C for 18 hours under reduced pressure to achieve a black powder. Large scale syntheses for the 5% mass loading were also conducted in very similar conditions with the primary difference of using 80 mg of the copper precursor, 65 mg of HHTP, 50 mL of the CNT/DMF solution and 50 mL of water. Cu_3HHTP_2 without nanotubes present were synthesized by using laboratory DMF.

4.5.3 DEP deposition on prefabricated silicon devices

Cu_3HHTP_2@SWCNTs powders at various mass loadings were sonicated into DMF at a concentration of 0.1 mg/mL for a total of one hour. Suspended solutions took on a deep blue color. These solutions were used for dielectrophoresis on prefabricate silicon devices with interdigitated electrodes with the following conditions: 60 µL of Cu_3HHTP_2@SWCNTs in DMF solution, 100 kHz frequency, 10 V of peak to peak voltage for two minutes. Devices were immediately washed with water and blown dry with N_2. Devices were left on a hotplate at 120 ^oC for 30 minutes before any FET measurements to remove residual solvent.

4.5.4 FET sensing of carbohydrates

Glucose, maltose, maltotriose, α-, β-, and γ-cyclodextrin were prepared in 1 mM concentrations utilizing deionized water as the solvent. Measurements for constant ionic strength were conducted by initially placing 100 mM KCl with deionized water in a 1:1 proportion on devices. The solution was in contact with an Ag/AgCl reference electrode. A 50 mV source drain bias was apply while gate voltages were swept from +600 mV to –600 mV in 200 total steps taking a total of 24 seconds. After this initial test, devices were washed with deionized water and blown dry with N_2 before the next test was conducted. This cycle was repeated for each sugar solution replacing the deionized water with the appropriate 1mM sugar solution.

For titration measurements, an initial set of measurements with the 1:1 100 mM KCl:deionized water was conducted. An addition equal volume aliquot of deionized water was then introduced without washing off the device. Electrical measurements followed the same parameters as above. This was repeated as many times as the titration required. Comparatively little changes caused by dilution of the electrolyte were observed as compared to presence of sugars.

5.0 Summary and Future Outlook

The research described in this dissertation develops several lines of inquiry which have rich possibilities for future discoveries. In Chapter 2, a novel strategy to pattern graphene into holey graphene was performed and characterized. The use of covalent organic frameworks to facilitate physical pattern masking is potentially very useful due to the synthetic diversity exhibited in linker chemistry, post functionalization, structure directing agents, and pore size. The as developed chemistry could also be used to pattern one-dimensional objects such as carbon nanotubes. The electronic consequences of such patterning on both graphene and carbon nanotubes also deserve fuller attention. Examining how changing pore size and pitch between holes with different reticular covalent organic frameworks affects resulting electronic band structure is a worthwhile endeavor to develop a family of electronic materials from graphene. Beyond patterning considerations, ability to control nanoparticle growth on the surface of holey graphene structures through metal salt concentration could use additional attention. A fuller study of different ligands and the resulting FET curves would be useful to demonstrate the ability of localized electronic structure changes at the nanoparticle surface to be transmitted across longer distances. Additionally, single layered holey graphene metal nanoparticle composites serve as an ideal platform for conductive atomic force microscopy measurements for a range of molecular conductors.

In Chapter 3, covalent organic framework patterning of single layer graphene was expanded to include highly ordered pyrolytic graphite with a range of different nanoparticle decoration. The developed composites showed size-controlled nanoparticle growth and synthetic control of fermi level through nanoparticle choice. Electrocatalytic behavior of this material towards OER was additionally promising and could be further improved through iron doping. This material serves as a rich synthetic landscape for a variety of chemistry which was not explored here. Composites with polymers, other two-dimensional materials, poly-elemental metallic nanoparticles, and semiconducting nanocrystals all serve as additional directions this project could take on. Polymer composites would be useful in both improving the mechanical strength of materials at potential low mass loadings as well as serving a conductive filler. Other two-dimensional materials (transition metal dichalcogenides or layered double hydroxides) could be interfaced with the exfoliated holey graphene material to achieve changes in electronic structure and to develop strongly bound solution phase materials sandwiches. Either placement of several different kinds of synthesized nanoparticles or alloying through galvanic displacement of holey graphene compound could be used to achieve even richer electronic control. The partial ligand environment of the holey graphene can also be used to access otherwise metastable states due to the size confining nature of the material. Semiconductor nanocrystals are potentially installable into holey graphene allowing for rapid conduction and photocatalytic schemes.

For both single layer and graphite derived holey graphene, a potential workflow could be established to aid in the development of sensors and catalysts in both liquid and gaseous states. Synthetic control over the edge moieties present in holey graphene could be used to modulate the strength of binding to the nanoparticles. The different binding strengths would modulate the interaction with analytes in the gas phase, including carbon dioxide, water, hydrogen, and oxygen. Tunability of the sensing response in the gas phase can be correlated to response in the liquid phase FET measurements including pH which can be used to understand how electronic communication in the composites is modulated by dielectric environment. The data assembled in these interactions can be used to identify promising combinations of edge chemistry and nanoparticle to facilitate carbon dioxide reduction reaction, oxygen reduction reaction, oxygen evolution reaction, and hydrogen evolution reaction. All these electrochemical reactions are important for future fuel cell development and energy storage. The combinatorial problem of assessing promising catalysts can be limited through pre-identification through sensing measurements.

In Chapter 4, synthetic techniques to integrate metal organic frameworks with two different kinds of nanotubes were developed. Primary considerations for achieving high electrical conductivity in composite materials were the presence of functional groups on the surface of the single-walled nanotubes as well as mass loading of the nanotube. Composite materials enabled size selective sensing of a homologous series of sugars through a novel ionic strength mediated mechanism. This class of composite materials is particularly interesting due to rich chemistry that can be performed on both nanotubes and metal organic frameworks. The variety of metal ions and linkers that can be introduced will inevitably change the interactions with analytes. Additionally, as nanotubes can be functionalized with a wide range of chemical moieties, the interaction between the two materials can be mediated greatly. There is more potential in studying how diffusion in confined environments can be monitored with nanotubes sensors. Another possibility is to monitor chemical modifications of the metal organic framework in real time. Size selective sensing could be adapted to a wide range of environments especially due to the large range of potential pore sizes which are achievable with metal organic frameworks.

The possibilities of rational carbon nanomaterial composites for sensing and catalytic applications are abundant. The exceptional electrical properties and large space of chemical reactions will enable many applications through composite formation that would be unachievable with any individual material. This work has illustrated just a few of those potential applications and highlighted potential directions for future work to go.

Appendix A Publications

Hwang, S., Chen, H., Fenk, C., Rothfuss, M., Bocan, K., Franconi, N., Morgan, G., **White, D. L.,** Burkert, S., Ellis, J.,Vinay, M., Rometo, D., Finegold, D., Cho, S. K., Sejdic, E., Star, A. *Manuscript Submitted*

Zeng, Z., Sorescu, D. C., **White, D. L.,** Hwang, S. I., Star, A. UiO-66-NH_2 Metal-Organic Framework/Single-walled Carbon Nanotube Hybrid Composites *Manuscript in preparation*

Bian, L., Wang, Z. **White, D. L.,** A. Star Machine Learning-Assisted Calibration of Hg^{2+} Sensors Based on Carbon Nanotube Field-Effect Transistors *Manuscript Submitted*

He, X. **White, D. L.,** Kapralov, A., Kagan, V. E., Star, A., Photoluminescent Response in Carbon Nanomaterials to Enzymatic Degradation *Anal. Chem* **2020,** Just Accepted

White, D. L., Lystrom, L., He, X., Burkert S.C., Kilin, D., Kilina, S., Star, A. Synthesis of Holey Graphene Nanoparticle Compounds *ACS Appl. Mater. Interfaces* **2020,** 12, 36513–36522

Luo, T. Y., Das, P., **White, D. L.**, Liu, C., Star, A. Rosi, N. Luminescence "Turn-On" Detection of Gossypol using Ln^{3+}-Based Metal-Organic Frameworks and Ln Salts *J. Am. Chem. Soc.* **2020,** 142, 2897-2904

Ellis, J. E., Sorescu, D. C., Hwang, S. I., Burkert, S. C., **White, D. L.**, Kim, H., Star, A. Modification of Carbon Nitride/Reduced Graphene Oxide van der Waals Heterostructure with Copper Nanoparticles to Improve CO_2 Sensitivity *ACS Appl. Mater. Interfaces* **2019,** 11, 41588-41594

Hwang, S. I., Franconi, N. G., Rothfuss, M. A., Bocan, K., Bian, L., **White, D. L.**, Burkert, S. C., Euler, R., Sopher, B. J., Vinay, M. L., Sejdic, E., Star A. Tetrahydrocannabinol (THC)

Detection using Semiconductor-enriched Single-Walled Carbon Nanotube Chemiresistors *ACS Sens.*, **2019,** 4, 2084-2093

Shao, W., Burkert, S. C., **White, D. L.**, Scott, V. L., Ding, J., Li, Z., Ouyang, J., Lapointe, F., Malenfant, P. R. L., Islam, K., Star, A. Probing Ca^{2+}-induced conformational change of Calmodulin with gold nanoparticle-decorated single-walled carbon nanotube field-effect transistors *Nanoscale* **2019,** 11, 13397-13406

White, D. L.; Burkert, S. C.; Hwang, S. I.; Star, A. Holey graphene metal nanoparticle composites via crystalline polymer templated etching *Nano Lett.*, **2019**, 19, 2824-2831.

Burkert, S. C.; Shurin, G. V.; **White, D. L.**; He, X.; Kapralov, A. A.; Kagan, V. E.; Shurin, M. R.; Star, A. Targeting myeloid regulators by paclitaxel-loaded enzymatically degradable nanocups *Nanoscale*, **2018**, 10, 17990-18000.

Ellis, J. E.; Zeng, Z.; Li, S.; Luo, T.; Burkert, S. C.; **White, D. L**.; Rosi, N. L.; Gassensmith, J. J.; Star, A. Growth of ZIF-8 on molecularly ordered 2-methylimidazole/single-walled carbon nanotubes to form highly porous, electrically conductive composites *Chem. Sci.*, **2019**, 10, 737-742

Bian, L.; Sorescu, D. C.; Chen, L.; **White, D. L.;** Burkert, S. C.; Khalifa, Y.; Zhang, Z.; Sejdic, E. Star, A. Machine learning identifications of the sensing descriptors relevant in molecular interactions with metal nanoparticle-decorated nanotube field-effect transistors *ACS Appl. Mater. Interfaces*, **2019**, 11, 1219–1227

Ellis, J. E.; Sorescu, D. C.; Burkert, S. C.; **White, D. L.**; Star, A. Uncondensed graphitic carbon nitride on reduced graphene oxide for oxygen sensing via a photoredox mechanism *ACS Appl. Mater. Interfaces* **2017**, *9*, 27142 – 27151.

Seo, W.; **White, D. L.**; Star, A. Fabrication of holey graphene: Catalytic oxidation by metalloporphyrin–based covalent organic framework immobilized on highly ordered pyrolytic graphite *Chem. Eur. J.* **2017,** *23,* 5652-5657.

Bibliography

1.Moore, G. E., Cramming more components onto integrated circuits, Reprinted from Electronics, volume 38, number 8, April 19, 1965, pp. 114 ff. *IEEE solid-state circuits society newsletter* **2006,** *11* (3), 33-35.

2.Whitesides, G. M., Nanoscience, nanotechnology, and chemistry. *Small* **2005,** *1* (2), 172-179.

3.Yin, Y.; Alivisatos, A. P., Colloidal nanocrystal synthesis and the organic–inorganic interface. *Nature* **2005,** *437* (7059), 664-670.

4.Murray, C.; Norris, D. J.; Bawendi, M. G., Synthesis and characterization of nearly monodisperse CdE (E= sulfur, selenium, tellurium) semiconductor nanocrystallites. *Journal of the American Chemical Society* **1993,** *115* (19), 8706-8715.

5.Zheng, G.; Patolsky, F.; Cui, Y.; Wang, W. U.; Lieber, C. M., Multiplexed electrical detection of cancer markers with nanowire sensor arrays. *Nature biotechnology* **2005,** *23* (10), 1294-1301.

6.Alivisatos, A. P., Semiconductor clusters, nanocrystals, and quantum dots. *science* **1996,** *271* (5251), 933-937.

7.Lieber, C. M.; Wang, Z. L., Functional nanowires. *MRS bulletin* **2007,** *32* (2), 99-108.

8.Novoselov, K. S.; Mishchenko, A.; Carvalho, A.; Neto, A. H. C., 2D materials and van der Waals heterostructures. *Science* **2016,** *353* (6298).

9.Roduner, E., Size matters: why nanomaterials are different. *Chemical Society Reviews* **2006,** *35* (7), 583-592.

10.Guo, Y.; Xu, K.; Wu, C.; Zhao, J.; Xie, Y., Surface chemical-modification for engineering the intrinsic physical properties of inorganic two-dimensional nanomaterials. *Chemical Society Reviews* **2015,** *44* (3), 637-646.

11.Dai, H.; Wong, E. W.; Lieber, C. M., Probing electrical transport in nanomaterials: conductivity of individual carbon nanotubes. *Science* **1996,** *272* (5261), 523-526.

12.Gogotsi, Y.; Presser, V., *Carbon nanomaterials*. CRC press: 2013.

13.Kroto, H. W.; Heath, J. R.; O'Brien, S. C.; Curl, R. F.; Smalley, R. E., C60: Buckminsterfullerene. *nature* **1985,** *318* (6042), 162-163.

14.Iijima, S., Helical microtubules of graphitic carbon. *nature* **1991,** *354* (6348), 56-58.

15.Novoselov, K. S.; Geim, A. K.; Morozov, S. V.; Jiang, D.; Zhang, Y.; Dubonos, S. V.; Grigorieva, I. V.; Firsov, A. A., Electric field effect in atomically thin carbon films. *science* **2004,** *306* (5696), 666-669.

16.Yu, M.-F.; Lourie, O.; Dyer, M. J.; Moloni, K.; Kelly, T. F.; Ruoff, R. S., Strength and breaking mechanism of multiwalled carbon nanotubes under tensile load. *Science* **2000,** *287* (5453), 637-640.

17.Frank, I. W.; Tanenbaum, D. M.; van der Zande, A. M.; McEuen, P. L., Mechanical properties of suspended graphene sheets. *Journal of Vacuum Science & Technology B: Microelectronics and Nanometer Structures Processing, Measurement, and Phenomena* **2007,** *25* (6), 2558-2561.

18.Zhou, C.; Kong, J.; Dai, H., Intrinsic electrical properties of individual single-walled carbon nanotubes with small band gaps. *Physical Review Letters* **2000,** *84* (24), 5604.

19.Yao, Z.; Kane, C. L.; Dekker, C., High-field electrical transport in single-wall carbon nanotubes. *Physical Review Letters* **2000,** *84* (13), 2941.

20.Sarma, S. D.; Adam, S.; Hwang, E. H.; Rossi, E., Electronic transport in two-dimensional graphene. *Reviews of modern physics* **2011,** *83* (2), 407.

21.Geim, A. K.; Novoselov, K. S., The rise of graphene. In *Nanoscience and technology: a collection of reviews from nature journals*, World Scientific: 2010; pp 11-19.

22.Novoselov, K. S.; Geim, A. K.; Morozov, S. V.; Jiang, D.; Katsnelson, M. I.; Grigorieva, I.; Dubonos, S.; Firsov; Aa, Two-dimensional gas of massless Dirac fermions in graphene. *nature* **2005,** *438* (7065), 197-200.

23.Hoffmann, R., How chemistry and physics meet in the solid state. *Angewandte Chemie International Edition in English* **1987,** *26* (9), 846-878.

24.Joselevich, E., Electronic structure and chemical reactivity of carbon nanotubes: a chemist's view. *ChemPhysChem* **2004,** *5* (5), 619-624.

25.Odom, T. W.; Huang, J.-L.; Kim, P.; Lieber, C. M., Atomic structure and electronic properties of single-walled carbon nanotubes. *Nature* **1998,** *391* (6662), 62-64.

26.Tasis, D.; Tagmatarchis, N.; Bianco, A.; Prato, M., Chemistry of carbon nanotubes. *Chemical reviews* **2006,** *106* (3), 1105-1136.

27.Eigler, S.; Hirsch, A., Chemistry with graphene and graphene oxide—challenges for synthetic chemists. *Angewandte Chemie International Edition* **2014,** *53* (30), 7720-7738.

28.Yan, K. A. I.; Fu, L. E. I.; Peng, H.; Liu, Z., Designed CVD growth of graphene via process engineering. *Accounts of chemical research* **2013,** *46* (10), 2263-2274.

29.Huang, M.; Ruoff, R. S., Growth of Single-Layer and Multilayer Graphene on Cu/Ni Alloy Substrates. *Accounts of Chemical Research* **2020,** *53* (4), 800-811.

30.Hummers Jr, W. S.; Offeman, R. E., Preparation of graphitic oxide. *Journal of the american chemical society* **1958,** *80* (6), 1339-1339.

31.Marcano, D. C.; Kosynkin, D. V.; Berlin, J. M.; Sinitskii, A.; Sun, Z.; Slesarev, A.; Alemany, L. B.; Lu, W.; Tour, J. M., Improved synthesis of graphene oxide. *ACS nano* **2010,** *4* (8), 4806-4814.

32.Pei, S.; Cheng, H.-M., The reduction of graphene oxide. *Carbon* **2012,** *50* (9), 3210-3228.

33.Cote, A. P.; Benin, A. I.; Ockwig, N. W.; O'Keeffe, M.; Matzger, A. J.; Yaghi, O. M., Porous, crystalline, covalent organic frameworks. *science* **2005,** *310* (5751), 1166-1170.

34.Diercks, C. S.; Yaghi, O. M., The atom, the molecule, and the covalent organic framework. *Science* **2017,** *355* (6328).

35.El-Kaderi, H. M.; Hunt, J. R.; Mendoza-Cortés, J. L.; Côté, A. P.; Taylor, R. E.; O'Keeffe, M.; Yaghi, O. M., Designed synthesis of 3D covalent organic frameworks. *Science* **2007,** *316* (5822), 268-272.

36.Cote, A. P.; El-Kaderi, H. M.; Furukawa, H.; Hunt, J. R.; Yaghi, O. M., Reticular synthesis of microporous and mesoporous 2D covalent organic frameworks. *Journal of the American Chemical Society* **2007,** *129* (43), 12914-12915.

37.Díaz, U.; Corma, A., Ordered covalent organic frameworks, COFs and PAFs. From preparation to application. *Coordination Chemistry Reviews* **2016,** *311*, 85-124.

38.Colson, J. W.; Dichtel, W. R., Rationally synthesized two-dimensional polymers. *Nature chemistry* **2013,** *5* (6), 453-465.

39.Zhang, B.; Wei, M.; Mao, H.; Pei, X.; Alshmimri, S. A.; Reimer, J. A.; Yaghi, O. M., Crystalline dioxin-linked covalent organic frameworks from irreversible reactions. *Journal of the American Chemical Society* **2018,** *140* (40), 12715-12719.

40.Su, Y.; Wan, Y.; Xu, H.; Otake, K.-i.; Tang, X.; Huang, L.; Kitagawa, S.; Gu, C., Crystalline and Stable Benzofuran-Linked Covalent Organic Frameworks from Irreversible Cascade Reactions. *Journal of the American Chemical Society* **2020**.

41.Evans, A. M.; Castano, I.; Brumberg, A.; Parent, L. R.; Corcos, A. R.; Li, R. L.; Flanders, N. C.; Gosztola, D. J.; Gianneschi, N. C.; Schaller, R. D., Emissive single-crystalline boroxine-linked colloidal covalent organic frameworks. *Journal of the American Chemical Society* **2019,** *141* (50), 19728-19735.

42.Smith, B. J.; Hwang, N.; Chavez, A. D.; Novotney, J. L.; Dichtel, W. R., Growth rates and water stability of 2D boronate ester covalent organic frameworks. *Chemical Communications* **2015,** *51* (35), 7532-7535.

43.Gao, Q.; Li, X.; Ning, G.-H.; Leng, K.; Tian, B.; Liu, C.; Tang, W.; Xu, H.-S.; Loh, K. P., Highly photoluminescent two-dimensional imine-based covalent organic frameworks for chemical sensing. *Chemical Communications* **2018,** *54* (19), 2349-2352.

44.Wei, S.; Zhang, F.; Zhang, W.; Qiang, P.; Yu, K.; Fu, X.; Wu, D.; Bi, S.; Zhang, F., Semiconducting 2D triazine-cored covalent organic frameworks with unsubstituted olefin linkages. *Journal of the American Chemical Society* **2019,** *141* (36), 14272-14279.

45.Lanni, L. M.; Tilford, R. W.; Bharathy, M.; Lavigne, J. J., Enhanced Hydrolytic Stability of Self-Assembling Alkylated Two-Dimensional Covalent Organic Frameworks. *Journal of the American Chemical Society* **2011,** *133* (35), 13975-13983.

46.Smith, B. J.; Overholts, A. C.; Hwang, N.; Dichtel, W. R., Insight into the crystallization of amorphous imine-linked polymer networks to 2D covalent organic frameworks. *Chemical Communications* **2016,** *52* (18), 3690-3693.

47.Colson, J. W.; Woll, A. R.; Mukherjee, A.; Levendorf, M. P.; Spitler, E. L.; Shields, V. B.; Spencer, M. G.; Park, J.; Dichtel, W. R., Oriented 2D covalent organic framework thin films on single-layer graphene. *Science* **2011,** *332* (6026), 228-31.

48.Li, Z.; Feng, X.; Zou, Y.; Zhang, Y.; Xia, H.; Liu, X.; Mu, Y., A 2D azine-linked covalent organic framework for gas storage applications. *Chemical Communications* **2014,** *50* (89), 13825-13828.

49.Wu, X.; Han, X.; Xu, Q.; Liu, Y.; Yuan, C.; Yang, S.; Liu, Y.; Jiang, J.; Cui, Y., Chiral BINOL-based covalent organic frameworks for enantioselective sensing. *Journal of the American Chemical Society* **2019,** *141* (17), 7081-7089.

50.Pachfule, P.; Acharjya, A.; Roeser, J. r. m.; Langenhahn, T.; Schwarze, M.; Schomäcker, R.; Thomas, A.; Schmidt, J., Diacetylene functionalized covalent organic framework (COF) for photocatalytic hydrogen generation. *Journal of the American Chemical Society* **2018,** *140* (4), 1423-1427.

51.Wang, P.; Wu, Q.; Han, L.; Wang, S.; Fang, S.; Zhang, Z.; Sun, S., Synthesis of conjugated covalent organic frameworks/graphene composite for supercapacitor electrodes. *Rsc advances* **2015,** *5* (35), 27290-27294.

52.Sun, B.; Zhu, C.-H.; Liu, Y.; Wang, C.; Wan, L.-J.; Wang, D., Oriented covalent organic framework film on graphene for robust ambipolar vertical organic field-effect transistor. *Chemistry of Materials* **2017,** *29* (10), 4367-4374.

53.Chen, X.; Zhang, H.; Ci, C.; Sun, W.; Wang, Y., Few-layered boronic ester based covalent organic frameworks/carbon nanotube composites for high-performance K-organic batteries. *ACS nano* **2019,** *13* (3), 3600-3607.

54.Kreno, L. E.; Leong, K.; Farha, O. K.; Allendorf, M.; Van Duyne, R. P.; Hupp, J. T., Metal–organic framework materials as chemical sensors. *Chemical reviews* **2012,** *112* (2), 1105-1125.

55.Férey, G., Hybrid porous solids: past, present, future. *Chemical Society Reviews* **2008,** *37* (1), 191-214.

56.Matheu, R.; Gutierrez-Puebla, E.; Monge, M. Á.; Diercks, C. S.; Kang, J.; Prévot, M. S.; Pei, X.; Hanikel, N.; Zhang, B.; Yang, P., Three-Dimensional Phthalocyanine Metal-Catecholates for High Electrochemical Carbon Dioxide Reduction. *Journal of the American Chemical Society* **2019,** *141* (43), 17081-17085.

57.Hmadeh, M.; Lu, Z.; Liu, Z.; Gándara, F.; Furukawa, H.; Wan, S.; Augustyn, V.; Chang, R.; Liao, L.; Zhou, F., New porous crystals of extended metal-catecholates. *Chemistry of Materials* **2012,** *24* (18), 3511-3513.

58.Farha, O. K.; Hupp, J. T., Rational design, synthesis, purification, and activation of metal−organic framework materials. *Accounts of chemical research* **2010,** *43* (8), 1166-1175.

59.Stavila, V.; Talin, A. A.; Allendorf, M. D., MOF-based electronic and opto-electronic devices. *Chemical Society Reviews* **2014,** *43* (16), 5994-6010.

60.Chen, T.; Dou, J.-H.; Yang, L.; Sun, C.; Libretto, N. J.; Skorupskii, G.; Miller, J. T.; Dincă, M., Continuous Electrical Conductivity Variation in M3 (Hexaiminotriphenylene) 2 (M= Co, Ni, Cu) MOF Alloys. *Journal of the American Chemical Society* **2020,** *142* (28), 12367-12373.

61.Dou, J.-H.; Sun, L.; Ge, Y.; Li, W.; Hendon, C. H.; Li, J.; Gul, S.; Yano, J.; Stach, E. A.; Dincă, M., Signature of metallic behavior in the metal–organic frameworks M3 (hexaiminobenzene) 2 (M= Ni, Cu). *Journal of the American Chemical Society* **2017,** *139* (39), 13608-13611.

62.Ko, M.; Mendecki, L.; Mirica, K. A., Conductive two-dimensional metal–organic frameworks as multifunctional materials. *Chemical Communications* **2018,** *54* (57), 7873-7891.

63.Freestone, I.; Meeks, N.; Sax, M.; Higgitt, C., The Lycurgus cup—a roman nanotechnology. *Gold bulletin* **2007,** *40* (4), 270-277.

64.El-Sayed, M. A., Some interesting properties of metals confined in time and nanometer space of different shapes. *Accounts of chemical research* **2001,** *34* (4), 257-264.

65.Ouyang, G.; Tan, X.; Yang, G., Thermodynamic model of the surface energy of nanocrystals. *Physical Review B* **2006,** *74* (19), 195408.

66.Park, J.; Joo, J.; Kwon, S. G.; Jang, Y.; Hyeon, T., Synthesis of monodisperse spherical nanocrystals. *Angewandte Chemie International Edition* **2007,** *46* (25), 4630-4660.

67.Wang, F.; Gu, H.; Swager, T. M., Carbon nanotube/polythiophene chemiresistive sensors for chemical warfare agents. *Journal of the American Chemical Society* **2008,** *130* (16), 5392-5393.

68.Paul, R. K.; Badhulika, S.; Saucedo, N. M.; Mulchandani, A., Graphene Nanomesh As Highly Sensitive Chemiresistor Gas Sensor. *Anal. Chem.* **2012,** *84* (19), 8171-8178.

69.Campbell, M. G.; Liu, S. F.; Swager, T. M.; Dincă, M., Chemiresistive sensor arrays from conductive 2D metal–organic frameworks. *Journal of the American Chemical Society* **2015,** *137* (43), 13780-13783.

70.Schroeder, V.; Savagatrup, S.; He, M.; Lin, S.; Swager, T. M., Carbon nanotube chemical sensors. *Chemical reviews* **2018,** *119* (1), 599-663.

71.Ganzhorn, M.; Vijayaraghavan, A.; Dehm, S.; Hennrich, F.; Green, A. A.; Fichtner, M.; Voigt, A.; Rapp, M.; von Löhneysen, H.; Hersam, M. C., Hydrogen sensing with diameter-and chirality-sorted carbon nanotubes. *Acs Nano* **2011,** *5* (3), 1670-1676.

72.Dey, A., Semiconductor metal oxide gas sensors: A review. *Materials Science and Engineering: B* **2018,** *229*, 206-217.

73.Korotcenkov, G.; Cho, B. K., Metal oxide composites in conductometric gas sensors: Achievements and challenges. *Sensors and Actuators B: Chemical* **2017,** *244*, 182-210.

74.Heller, I.; Chatoor, S.; Männik, J.; Zevenbergen, M. A. G.; Dekker, C.; Lemay, S. G., Comparing the weak and strong gate-coupling regimes for nanotube and graphene transistors. *physica status solidi (RRL)–Rapid Research Letters* **2009,** *3* (6), 190-192.

75.McEuen, P. L.; Fuhrer, M. S.; Park, H., Single-walled carbon nanotube electronics. *IEEE transactions on nanotechnology* **2002,** *1* (1), 78-85.

76.Kauffman, D. R.; Sorescu, D. C.; Schofield, D. P.; Allen, B. L.; Jordan, K. D.; Star, A., Understanding the sensor response of metal-decorated carbon nanotubes. *Nano letters* **2010,** *10* (3), 958-963.

77.Katz, E.; Willner, I., Biomolecule-functionalized carbon nanotubes: applications in nanobioelectronics. *ChemPhysChem* **2004,** *5* (8), 1084-1104.

78.Zhao, Y.-L.; Stoddart, J. F., Noncovalent functionalization of single-walled carbon nanotubes. *Accounts of chemical research* **2009,** *42* (8), 1161-1171.

79.Zhao, Y. L.; Hu, L.; Stoddart, J. F.; Grüner, G., Pyrenecyclodextrin-decorated single-walled carbon nanotube field-effect transistors as chemical sensors. *Advanced Materials* **2008,** *20* (10), 1910-1915.

80.Rao, R.; Pint, C. L.; Islam, A. E.; Weatherup, R. S.; Hofmann, S.; Meshot, E. R.; Wu, F.; Zhou, C.; Dee, N.; Amama, P. B., Carbon nanotubes and related nanomaterials: critical advances and challenges for synthesis toward mainstream commercial applications. *ACS nano* **2018,** *12* (12), 11756-11784.

81.Ebbesen, T. W.; Hiura, H.; Bisher, M. E.; Treacy, M. M. J.; Shreeve-Keyer, J. L.; Haushalter, R. C., Decoration of carbon nanotubes. *Advanced Materials* **1996,** *8* (2), 155-157.

82.Luo, Z.; Somers, L. A.; Dan, Y.; Ly, T.; Kybert, N. J.; Mele, E. J.; Johnson, A. T. C., Size-selective nanoparticle growth on few-layer graphene films. *Nano letters* **2010,** *10* (3), 777-781.

83.Sun, J.; Klechikov, A.; Moise, C.; Prodana, M.; Enachescu, M.; Talyzin, A. V., A molecular pillar approach to grow vertical covalent organic framework nanosheets on graphene: hybrid materials for energy storage. *Angewandte Chemie* **2018,** *130* (4), 1046-1050.

84.Ong, W.-J.; Tan, L.-L.; Chai, S.-P.; Yong, S.-T., Graphene oxide as a structure-directing agent for the two-dimensional interface engineering of sandwich-like graphene–gC 3 N 4 hybrid nanostructures with enhanced visible-light photoreduction of CO 2 to methane. *Chemical Communications* **2015,** *51* (5), 858-861.

85.Intergovernmental Panel on Climate, C., IPCC Fifth Assessment Report (AR5) Observed Climate Change Impacts Database, Version 2.01. NASA Socioeconomic Data and Applications Center (SEDAC): Palisades, NY, 2017.

86.Duan, J.; Chen, S.; Jaroniec, M.; Qiao, S. Z., Heteroatom-doped graphene-based materials for energy-relevant electrocatalytic processes. *Acs Catalysis* **2015,** *5* (9), 5207-5234.

87.Yan, Y.; Xia, B. Y.; Zhao, B.; Wang, X., A review on noble-metal-free bifunctional heterogeneous catalysts for overall electrochemical water splitting. *Journal of Materials Chemistry A* **2016,** *4* (45), 17587-17603.

88.Lim, R. J.; Xie, M.; Sk, M. A.; Lee, J.-M.; Fisher, A.; Wang, X.; Lim, K. H., A review on the electrochemical reduction of CO2 in fuel cells, metal electrodes and molecular catalysts. *Catalysis Today* **2014,** *233*, 169-180.

89.Fu, L.; Zeng, X.; Huang, C.; Cai, P.; Cheng, G.; Luo, W., Ultrasmall Ir nanoparticles for efficient acidic electrochemical water splitting. *Inorganic Chemistry Frontiers* **2018,** *5* (5), 1121-1125.

90.Cheng, X.; Wang, H.; Ming, M.; Luo, W.; Wang, Y.; Yang, Y.; Zhang, Y.; Gao, D.; Bi, J.; Fan, G., Well-defined Ru nanoclusters anchored on carbon: facile synthesis and high electrochemical activity toward alkaline water splitting. *ACS Sustainable Chemistry & Engineering* **2018,** *6* (9), 11487-11492.

91.Wang, J.; Cui, W.; Liu, Q.; Xing, Z.; Asiri, A. M.; Sun, X., Recent progress in cobalt-based heterogeneous catalysts for electrochemical water splitting. *Advanced materials* **2016,** *28* (2), 215-230.

92.Fominykh, K.; Feckl, J. M.; Sicklinger, J.; Döblinger, M.; Böcklein, S.; Ziegler, J.; Peter, L.; Rathousky, J.; Scheidt, E. W.; Bein, T., Ultrasmall dispersible crystalline nickel oxide nanoparticles as high-performance catalysts for electrochemical water splitting. *Advanced Functional Materials* **2014,** *24* (21), 3123-3129.

93.Anantharaj, S.; Ede, S. R.; Sakthikumar, K.; Karthick, K.; Mishra, S.; Kundu, S., Recent trends and perspectives in electrochemical water splitting with an emphasis on sulfide, selenide, and phosphide catalysts of Fe, Co, and Ni: a review. *Acs Catalysis* **2016,** *6* (12), 8069-8097.

94.Sun, X.; Shao, Q.; Pi, Y.; Guo, J.; Huang, X., A general approach to synthesise ultrathin NiM (M= Fe, Co, Mn) hydroxide nanosheets as high-performance low-cost electrocatalysts for overall water splitting. *Journal of Materials Chemistry A* **2017,** *5* (17), 7769-7775.

95.Xin, H.; Vojvodic, A.; Voss, J.; Nørskov, J. K.; Abild-Pedersen, F., Effects of d-band shape on the surface reactivity of transition-metal alloys. *Physical Review B* **2014,** *89* (11), 115114.

96.Roger, I.; Shipman, M. A.; Symes, M. D., Earth-abundant catalysts for electrochemical and photoelectrochemical water splitting. *Nature Reviews Chemistry* **2017,** *1* (1), 1-13.

97.Bai, J.; Zhong, X.; Jiang, S.; Huang, Y.; Duan, X., Graphene nanomesh. *Nature nanotechnology* **2010,** *5* (3), 190-194.

98.Zhu, Y.; Murali, S.; Cai, W.; Li, X.; Suk, J. W.; Potts, J. R.; Ruoff, R. S., Graphene and graphene oxide: synthesis, properties, and applications. *Advanced materials* **2010,** *22* (35), 3906-3924.

99.Xu, Y.; Chen, C. Y.; Zhao, Z.; Lin, Z.; Lee, C.; Xu, X.; Wang, C.; Huang, Y.; Shakir, M. I.; Duan, X., Solution Processable Holey Graphene Oxide and Its Derived Macrostructures for High-Performance Supercapacitors. *Nano Lett.* **2015,** *15* (7), 4605-10.

100.Hu, X.; Bai, D.; Wu, Y.; Chen, S.; Ma, Y.; Lu, Y.; Chao, Y.; Bai, Y., A facile synthesis of reduced holey graphene oxide for supercapacitors. *Chem Commun (Camb)* **2017,** *53* (99), 13225-13228.

101.Han, T. H.; Huang, Y. K.; Tan, A. T.; Dravid, V. P.; Huang, J., Steam etched porous graphene oxide network for chemical sensing. *J Am Chem Soc* **2011,** *133* (39), 15264-7.

102.Vedala, H.; Sorescu, D. C.; Kotchey, G. P.; Star, A., Chemical Sensitivity of Graphene Edges Decorated with Metal Nanoparticles. *Nano Letters* **2011,** *11* (6), 2342-2347.

103.Zhao, X.; Hayner, C. M.; Kung, M. C.; Kung, H. H., Flexible Holey Graphene Paper Electrodes with Enhanced Rate Capability for Energy Storage Applications. *ACS Nano* **2011,** *5* (11), 8739-8749.

104.Han, X.; Funk, M. R.; Shen, F.; Chen, Y.-C.; Li, Y.; Campbell, C. J.; Dai, J.; Yang, X.; Kim, J.-W.; Liao, Y.; Connell, J. W.; Barone, V.; Chen, Z.; Lin, Y.; Hu, L., Scalable Holey Graphene Synthesis and Dense Electrode Fabrication toward High-Performance Ultracapacitors. *ACS Nano* **2014,** *8* (8), 8255-8265.

105.Yang, Y.; Yang, X.; Zou, X.; Wu, S.; Wan, D.; Cao, A.; Liao, L.; Yuan, Q.; Duan, X., Ultrafine Graphene Nanomesh with Large On/Off Ratio for High-Performance Flexible Biosensors. *Adv. Funct. Mater.* **2017,** *27* (19).

106.Liang, X.; Jung, Y.-S.; Wu, S.; Ismach, A.; Olynick, D. L.; Cabrini, S.; Bokor, J., Formation of Bandgap and Subbands in Graphene Nanomeshes with Sub-10 nm Ribbon Width Fabricated via Nanoimprint Lithography. *Nano Letters* **2010,** *10* (7), 2454-2460.

107.Gethers, M. L.; Thomas, J. C.; Jiang, S.; Weiss, N. O.; Duan, X.; Goddard, W. A.; Weiss, P. S., Holey Graphene as a Weed Barrier for Molecules. *ACS Nano* **2015,** *9* (11), 10909-10915.

108.Moreno, C.; Vilas-Varela, M.; Kretz, B.; Garcia-Lekue, A.; Costache, M. V.; Paradinas, M.; Panighel, M.; Ceballos, G.; Valenzuela, S. O.; Pena, D.; Mugarza, A., Bottom-up synthesis of multifunctional nanoporous graphene. *Science* **2018,** *360* (6385), 199-203.

109.Du, Y.; Yang, H.; Whiteley, J. M.; Wan, S.; Jin, Y.; Lee, S. H.; Zhang, W., Ionic Covalent Organic Frameworks with Spiroborate Linkage. *Angew Chem Int Ed Engl* **2016,** *55* (5), 1737-41.

110.Wan, S.; Gándara, F.; Asano, A.; Furukawa, H.; Saeki, A.; Dey, S. K.; Liao, L.; Ambrogio, M. W.; Botros, Y. Y.; Duan, X.; Seki, S.; Stoddart, J. F.; Yaghi, O. M., Covalent Organic Frameworks with High Charge Carrier Mobility. *Chemistry of Materials* **2011,** *23* (18), 4094-4097.

111.DeBlase, C. R.; Silberstein, K. E.; Truong, T. T.; Abruna, H. D.; Dichtel, W. R., beta-Ketoenamine-linked covalent organic frameworks capable of pseudocapacitive energy storage. *J Am Chem Soc* **2013,** *135* (45), 16821-4.

112.Lin, S.; Diercks, C. S.; Zhang, Y.-B.; Kornienko, N.; Nichols, E. M.; Zhao, Y.; Paris, A. R.; Kim, D.; Yang, P.; Yaghi, O. M.; Chang, C. J., Covalent organic frameworks comprising cobalt porphyrins for catalytic CO_2 reduction in water. *Science* **2015,** *349* (6253), 1208-1213.

113.Phan, D.-T.; Chung, G.-S., A novel Pd nanocube–graphene hybrid for hydrogen detection. *Sensors and Actuators B: Chemical* **2014,** *199,* 354-360.

114.Pak, Y.; Kim, S. M.; Jeong, H.; Kang, C. G.; Park, J. S.; Song, H.; Lee, R.; Myoung, N.; Lee, B. H.; Seo, S.; Kim, J. T.; Jung, G. Y., Palladium-decorated hydrogen-gas sensors using periodically aligned graphene nanoribbons. *ACS Appl Mater Interfaces* **2014,** *6* (15), 13293-8.

115.Li, W.; Geng, X.; Guo, Y.; Rong, J.; Gong, Y.; Wu, L.; Zhang, X.; Li, P.; Xu, J.; Cheng, G.; Sun, M.; Liu, L., Reduced Graphene Oxide Electrically Contacted Graphene Sensor for Highly Sensitive Nitric Oxide Detection. *ACS Nano* **2011,** *5* (9), 6955-6961.

116.Yoo, E.; Okata, T.; Akita, T.; Kohyama, M.; Nakamura, J.; Honma, I., Enhanced Electrocatalytic Activity of Pt Subnanoclusters on Graphene Nanosheet Surface. *Nano Letters* **2009,** *9* (6), 2255-2259.

117.Guo, S.; Dong, S.; Wang, E., Three-Dimensional Pt-on-Pd Bimetallic Nanodendrites Supported on Graphene Nanosheet: Facile Synthesis and Used as an Advanced Nanoelectrocatalyst for Methanol Oxidation. *ACS Nano* **2010,** *4* (1), 547-555.

118.Kong, B. S.; Geng, J.; Jung, H. T., Layer-by-layer assembly of graphene and gold nanoparticles by vacuum filtration and spontaneous reduction of gold ions. *Chem Commun (Camb)* **2009,** (16), 2174-6.

119.Chen, X.; Wu, G.; Chen, J.; Chen, X.; Xie, Z.; Wang, X., Synthesis of "clean" and well-dispersive Pd nanoparticles with excellent electrocatalytic property on graphene oxide. *J Am Chem Soc* **2011,** *133* (11), 3693-5.

120.Lv, R.; Li, Q.; Botello-Mendez, A. R.; Hayashi, T.; Wang, B.; Berkdemir, A.; Hao, Q.; Elias, A. L.; Cruz-Silva, R.; Gutierrez, H. R.; Kim, Y. A.; Muramatsu, H.; Zhu, J.; Endo, M.; Terrones, H.; Charlier, J. C.; Pan, M.; Terrones, M., Nitrogen-doped graphene: beyond single substitution and enhanced molecular sensing. *Sci. Rep.* **2012,** *2*, 586.

121.Pirkle, A.; Chan, J.; Venugopal, A.; Hinojos, D.; Magnuson, C. W.; McDonnell, S.; Colombo, L.; Vogel, E. M.; Ruoff, R. S.; Wallace, R. M., The effect of chemical residues on the physical and electrical properties of chemical vapor deposited graphene transferred to SiO2. *Applied Physics Letters* **2011,** *99* (12), 3.

122.White, D. L.; Burkert, S. C.; Hwang, S. I.; Star, A., Holey Graphene Metal Nanoparticle Composites via Crystalline Polymer Templated Etching. *Nano Lett.* **2019,** *19* (5), 2824-2831.

123.Lukose, B.; Kuc, A.; Heine, T., The structure of layered covalent-organic frameworks. *Chemistry* **2011,** *17* (8), 2388-92.

124.Wu, J. B.; Lin, M. L.; Cong, X.; Liu, H. N.; Tan, P. H., Raman spectroscopy of graphene-based materials and its applications in related devices. *Chem Soc Rev* **2018,** *47* (5), 1822-1873.

125.Zhao, Y.; Zhu, Y., Graphene-based hybrid films for plasmonic sensing. *Nanoscale* **2015,** *7* (35), 14561-76.

126.Haiss, W.; Thanh, N. T. K.; Aveyard, J.; Fernig, D. G., Determination of Size and Concentration of Gold Nanoparticles from UV−Vis Spectra. *Analytical Chemistry* **2007,** *79* (11), 4215-4221.

127.Gunasinghe, R. N.; Reuven, D. G.; Suggs, K.; Wang, X.-Q., Filled and Empty Orbital Interactions in a Planar Covalent Organic Framework on Graphene. *The Journal of Physical Chemistry Letters* **2012,** *3* (20), 3048-3052.

128.Ryu, S.; Liu, L.; Berciaud, S.; Yu, Y. J.; Liu, H.; Kim, P.; Flynn, G. W.; Brus, L. E., Atmospheric oxygen binding and hole doping in deformed graphene on a SiO(2) substrate. *Nano Lett* **2010,** *10* (12), 4944-51.

129.Nourbakhsh, A.; Cantoro, M.; Vosch, T.; Pourtois, G.; Clemente, F.; van der Veen, M. H.; Hofkens, J.; Heyns, M. M.; De Gendt, S.; Sels, B. F., Bandgap opening in oxygen plasma-treated graphene. *Nanotechnology* **2010,** *21* (43), 435203.

130.Wu, J.; Xie, L.; Li, Y.; Wang, H.; Ouyang, Y.; Guo, J.; Dai, H., Controlled chlorine plasma reaction for noninvasive graphene doping. *J Am Chem Soc* **2011,** *133* (49), 19668-71.

131.Mubeen, S.; Zhang, T.; Chartuprayoon, N.; Rheem, Y.; Mulchandani, A.; Myung, N. V.; Deshusses, M. A., Sensitive Detection of H2S Using Gold Nanoparticle Decorated Single-Walled Carbon Nanotubes. *Analytical Chemistry* **2010,** *82* (1), 250-257.

132.Johnson, J. L.; Behnam, A.; Pearton, S. J.; Ural, A., Hydrogen sensing using pd-functionalized multi-layer graphene nanoribbon networks. *Adv Mater* **2010,** *22* (43), 4877-80.

133.Phan, D.-T.; Chung, G.-S., Characteristics of resistivity-type hydrogen sensing based on palladium-graphene nanocomposites. *Int. J. Hydrogen Energy* **2014,** *39* (1), 620-629.

134.Shin, D. H.; Lee, J. S.; Jun, J.; An, J. H.; Kim, S. G.; Cho, K. H.; Jang, J., Flower-like Palladium Nanoclusters Decorated Graphene Electrodes for Ultrasensitive and Flexible Hydrogen Gas Sensing. *Sci Rep* **2015,** *5*, 12294.

135.Lange, U.; Hirsch, T.; Mirsky, V. M.; Wolfbeis, O. S., Hydrogen sensor based on a graphene – palladium nanocomposite. *Electrochim. Acta* **2011,** *56* (10), 3707-3712.

136.Phan, D.-T.; Chung, G.-S., Effects of Pd nanocube size of Pd nanocube-graphene hybrid on hydrogen sensing properties. *Sensors and Actuators B: Chemical* **2014,** *204*, 437-444.

137.Song, Z.; Wei, Z.; Wang, B.; Luo, Z.; Xu, S.; Zhang, W.; Yu, H.; Li, M.; Huang, Z.; Zang, J.; Yi, F.; Liu, H., Sensitive Room-Temperature H2S Gas Sensors Employing SnO2 Quantum Wire/Reduced Graphene Oxide Nanocomposites. *Chem. Mater.* **2016,** *28* (4), 1205-1212.

138.Ovsianytskyi, O.; Nam, Y.-S.; Tsymbalenko, O.; Lan, P.-T.; Moon, M.-W.; Lee, K.-B., Highly sensitive chemiresistive H 2 S gas sensor based on graphene decorated with Ag nanoparticles and charged impurities. *Sensors and Actuators B: Chemical* **2018,** *257*, 278-285.

139.Tjoa, V.; Jun, W.; Dravid, V.; Mhaisalkar, S.; Mathews, N., Hybrid graphene–metal nanoparticle systems: electronic properties and gas interaction. *J. Mater. Chem.* **2011,** *21* (39).

140.Gutes, A.; Hsia, B.; Sussman, A.; Mickelson, W.; Zettl, A.; Carraro, C.; Maboudian, R., Graphene decoration with metal nanoparticles: towards easy integration for sensing applications. *Nanoscale* **2012,** *4* (2), 438-40.

141.Kim, S. M.; Hsu, A.; Lee, Y. H.; Dresselhaus, M.; Palacios, T.; Kim, K. K.; Kong, J., The effect of copper pre-cleaning on graphene synthesis. *Nanotechnology* **2013,** *24* (36), 365602.

142.Zhu, Y.; Murali, S.; Cai, W.; Li, X.; Suk, J. W.; Potts, J. R.; Ruoff, R. S., Graphene and graphene oxide: synthesis, properties, and applications. *Adv. Mater.* **2010,** *22* (35), 3906-24.

143.Chen, Q.; Zhang, L.; Chen, G., Facile Preparation of Graphene-Copper Nanoparticle Composite by in situ Chemical Reduction for Electrochemical Sensing of Carbohydrates. *Anal. Chem.* **2012,** *84* (1), 171-178.

144.Liu, J.; Ma, Q.; Huang, Z.; Liu, G.; Zhang, H., Recent Progress in Graphene-Based Noble-Metal Nanocomposites for Electrocatalytic Applications. *Adv. Mater.* **2019,** *31* (9), e1800696.

145.Jo, G.; Choe, M.; Lee, S.; Park, W.; Kahng, Y. H.; Lee, T., The Application of Graphene as Electrodes in Electrical and Optical Devices. *Nanotechnology* **2012,** *23* (11), 112001-112012.

146.Georgakilas, V.; Tiwari, J. N.; Kemp, K. C.; Perman, J. A.; Bourlinos, A. B.; Kim, K. S.; Zboril, R., Noncovalent Functionalization of Graphene and Graphene Oxide for Energy Materials, Biosensing, Catalytic, and Biomedical Applications. *Chem Rev* **2016,** *116* (9), 5464-519.

147.Novoselov, K. S.; Fal'ko, V. I.; Colombo, L.; Gellert, P. R.; Schwab, M. G.; Kim, K., A Roadmap for Graphene. *Nature* **2012,** *490* (7419), 192-200.

148.Ehsani, A.; Heidari, A. A.; Shiri, H. M., Electrochemical pseudocapacitors based on ternary nanocomposite of conductive polymer/graphene/metal oxide: An introduction and review to it in recent studies. *The Chemical Record* **2019,** *19* (5), 908-926.

149.Ajdari, F. B.; Kowsari, E.; Ehsani, A.; Schorowski, M.; Ameri, T., New synthesized ionic liquid functionalized graphene oxide: synthesis, characterization and its nanocomposite with conjugated polymer as effective electrode materials in an energy storage device. *Electrochimica Acta* **2018,** *292*, 789-804.

150.Ehsani, A.; Kowsari, E.; Ajdari, F. B.; Safari, R.; Shiri, H. M., Sulfonated graphene oxide and its nanocomposites with electroactive conjugated polymer as effective pseudocapacitor electrode materials. *Journal of colloid and interface science* **2017,** *497*, 258-265.

151.Higgins, D.; Zamani, P.; Yu, A.; Chen, Z., The Application of Graphene and its Composites in Oxygen Reduction Electrocatalysis: a Perspective and Review of Recent Progress. *Energy Environ. Sci.* **2016,** *9* (2), 357-390.

152.Kou, R.; Shao, Y.; Mei, D.; Nie, Z.; Wang, D.; Wang, C.; Viswanathan, V. V.; Park, S.; Aksay, I. A.; Lin, Y., Stabilization of Electrocatalytic Metal Nanoparticles at Metal− Metal Oxide− Graphene Triple Junction Points. *J. Am. Chem. Soc.* **2011,** *133* (8), 2541-2547.

153.Li, Y.; Zhou, W.; Wang, H.; Xie, L.; Liang, Y.; Wei, F.; Idrobo, J. C.; Pennycook, S. J.; Dai, H., An Oxygen Reduction Electrocatalyst Based on Carbon Nanotube-Graphene Complexes. *Nat. Nanotechnol.* **2012,** *7* (6), 394-400.

154.Liang, Y.; Li, Y.; Wang, H.; Zhou, J.; Wang, J.; Regier, T.; Dai, H., Co 3 O 4 Nanocrystals On Graphene as a Synergistic Catalyst for Oxygen Reduction Reaction. *Nat. Mat.* **2011,** *10* (10), 780.

155.Dou, S.; Tao, L.; Huo, J.; Wang, S.; Dai, L., Etched and Doped Co 9 S 8/Graphene Hybrid for Oxygen Electrocatalysis. *Energy Environ. Sci.* **2016,** *9* (4), 1320-1326.

156.Li, J. S.; Wang, Y.; Liu, C. H.; Li, S. L.; Wang, Y. G.; Dong, L. Z.; Dai, Z. H.; Li, Y. F.; Lan, Y. Q., Coupled Molybdenum Carbide and Reduced Graphene Oxide Electrocatalysts for Efficient Hydrogen Evolution. *Nat. Commun.* **2016,** *7*, 11204.

157.Li, Y.; Li, Y.; Zhu, E.; McLouth, T.; Chiu, C. Y.; Huang, X.; Huang, Y., Stabilization of High-Performance Oxygen Reduction Reaction Pt Electrocatalyst Supported on Reduced Graphene Oxide/Carbon Black Composite. *J. Am. Chem. Soc.* **2012,** *134* (30), 12326-12329.

158.Wang, H.; Dai, H., Strongly coupled inorganic-nano-carbon hybrid materials for energy storage. *Chem. Soc. Rev.* **2013,** *42* (7), 3088-113.

159.Liang, Y.; Li, Y.; Wang, H.; Dai, H., Strongly Coupled Inorganic/Nanocarbon Hybrid Materials for Advanced Electrocatalysis. *J. Am. Chem. Soc.* **2013,** *135* (6), 2013-2036.

160.Yang, S.; Zhi, L.; Tang, K.; Feng, X.; Maier, J.; Müllen, K., Efficient Synthesis of Heteroatom (N Or S)-Doped Graphene Based on Ultrathin Graphene Oxide-Porous Silica Sheets for Oxygen Reduction Reactions. *Adv. Funct.Mater.* **2012,** *22* (17), 3634-3640.

161.Wang, X.; Sun, G.; Routh, P.; Kim, D. H.; Huang, W.; Chen, P., Heteroatom-Doped Graphene Materials: Syntheses, Properties and Applications. *Chem. Soc. Rev.* **2014,** *43* (20), 7067-7098.

162.Zheng, Y.; Jiao, Y.; Ge, L.; Jaroniec, M.; Qiao, S. Z., Two-Step Boron and Nitrogen Doping in Graphene for Enhanced Synergistic Catalysis. *Angew. Chem. Int. Ed .Engl.* **2013,** *52* (11), 3110-3116.

163.Peng, G.; Ellis, J. E.; Xu, G.; Xu, X.; Star, A., In Situ Grown TiO2 Nanospindles Facilitate the Formation of Holey Reduced Graphene Oxide by Photodegradation. *ACS Appl. Mater. Interfaces* **2016,** *8* (11), 7403-7410.

164.Xu, Y.; Lin, Z.; Zhong, X.; Huang, X.; Weiss, N. O.; Huang, Y.; Duan, X., Holey Graphene Frameworks for Highly Efficient Capacitive Energy Storage. *Nat. Commun.* **2014,** *5*, 4554.

165.Lin, Y.; Han, X.; Campbell, C. J.; Kim, J. W.; Zhao, B.; Luo, W.; Dai, J.; Hu, L.; Connell, J. W., Holey Graphene Nanomanufacturing: Structure, Composition, and Electrochemical Properties. *Adv.Funct. Mater.* **2015,** *25* (19), 2920-2927.

166.White, D. L.; Lystrom, L.; He, X.; Burkert, S. C.; Kilin, D. S.; Kilina, S.; Star, A., Synthesis of Holey Graphene Nanoparticle Compounds. *ACS Applied Materials & Interfaces* **2020**.

167.Li, H.; Chavez, A. D.; Li, H.; Li, H.; Dichtel, W. R.; Bredas, J. L., Nucleation and Growth of Covalent Organic Frameworks from Solution: The Example of COF-5. *J. Am. Chem. Soc.* **2017,** *139* (45), 16310-16318.

168.White, D. L.; Burkert, S. C.; Hwang, S. I.; Star, A., Holey Graphene Metal Nanoparticle Composites via Crystalline Polymer Templated Etching. *Nano Lett.* **2019,** *19* (5), 2824-2831.

169.Bepete, G.; Anglaret, E.; Ortolani, L.; Morandi, V.; Huang, K.; Penicaud, A.; Drummond, C., Surfactant-Free Single-Layer Graphene in Water. *Nat. Chem.* **2017,** *9* (4), 347-352.

170.Haar, S. b.; Bruna, M.; Lian, J. X.; Tomarchio, F.; Olivier, Y.; Mazzaro, R.; Morandi, V.; Moran, J.; Ferrari, A. C.; Beljonne, D., Liquid-Phase Exfoliation of Graphite Into Single-and Few-Layer Graphene With α-Functionalized Alkanes. *J. Phys. Chem. Lett.* **2016,** *7* (14), 2714-2721.

171.Henglein, A., Colloidal Silver Nanoparticles: Photochemical Preparation and Interaction with O2, CCl4, and Some Metal Ions. *Chem. Mater.* **1998,** *10* (1), 444-450.

172.Sharma, R.; Baik, J. H.; Perera, C. J.; Strano, M. S., Anomalously Large Reactivity of Single Graphene Layers and Edges Toward Electron Transfer Chemistries. *Nano Lett.* **2010,** *10* (2), 398-405.

173.Raj, M. A.; John, S. A., Assembly of Gold Nanoparticles on Graphene Film Via Electroless Deposition: Spontaneous Reduction of Au 3+ Ions by Graphene Film. *RSC Advances* **2015,** *5* (7), 4964-4971.

174.Briggs, D., Practical Surface Analysis. *Auger and X-Ray Photoelecton Spectroscory* **1990,** *1*, 151-152.

175.Menard, L. D.; Xu, F.; Nuzzo, R. G.; Yang, J. C., Preparation of TiO2-Supported Au Nanoparticle Catalysts From a Au13 Cluster Precursor: Ligand Removal Using Ozone Exposure Versus a Rapid Thermal Treatment. *J. Catal.* **2006,** *243* (1), 64-73.

176.Shichibu, Y.; Konishi, K., HCl-Induced Nuclearity Convergence in Diphosphine-Protected Ultrasmall Gold Clusters: A Novel Synthetic Route to "Magic-Number" Au13 Clusters. *Small* **2010,** *6* (11), 1216-1220.

177.Okumura, M.; Kitagawa, Y.; Kawakami, T.; Haruta, M., Theoretical Investigation of the Hetero-Junction Effect in PVP-Stabilized Au13 Clusters. The Role of PVP in Their Catalytic Activities. *Chem. Phys. Lett.* **2008,** *459* (1-6), 133-136.

178.Larsson, J.; Nolan, M.; Greer, J. C., Interactions Between Thiol Molecular Linkers and the Au13 Nanoparticle. *J. Phys. Chem. B* **2002,** *106* (23), 5931-5937.

179.Gifford, B. J.; Kilina, S.; Htoon, H.; Doorn, S. K.; Tretiak, S., Exciton Localization and Optical Emission in Aryl-Functionalized Carbon Nanotubes. *J. Phys. Chem. C* **2017,** *122* (3), 1828-1838.

180.He, X.; Gifford, B. J.; Hartmann, N. F.; Ihly, R.; Ma, X.; Kilina, S. V.; Luo, Y.; Shayan, K.; Strauf, S.; Blackburn, J. L.; Tretiak, S.; Doorn, S. K.; Htoon, H., Low-Temperature Single Carbon Nanotube Spectroscopy of sp(3) Quantum Defects. *ACS Nano* **2017,** *11* (11), 10785-10796.

181.Saha, A.; Gifford, B. J.; He, X.; Ao, G.; Zheng, M.; Kataura, H.; Htoon, H.; Kilina, S.; Tretiak, S.; Doorn, S. K., Narrow-Band Single-Photon Emission Through Selective Aryl Functionalization of Zigzag Carbon Nanotubes. *Nat. Chem.* **2018,** *10* (11), 1089-1095.

182.Wang, L.; Chen, H.; Daniel, Q.; Duan, L.; Philippe, B.; Yang, Y.; Rensmo, H.; Sun, L., Promoting the Water Oxidation Catalysis by Synergistic Interactions between Ni(OH)2and Carbon Nanotubes. *Adv. Energy Mater.* **2016,** *6* (15), 1600516.

183.Guo, X.; Kong, R.-M.; Zhang, X.; Du, H.; Qu, F., Ni(OH)2 Nanoparticles Embedded in Conductive Microrod Array: An Efficient and Durable Electrocatalyst for Alkaline Oxygen Evolution Reaction. *ACS Catalysis* **2017,** *8* (1), 651-655.

184.McCrory, C. C.; Jung, S.; Peters, J. C.; Jaramillo, T. F., Benchmarking heterogeneous electrocatalysts for the oxygen evolution reaction. *J. Am. Chem. Soc.* **2013,** *135* (45), 16977-16987.

185.Klaus, S.; Cai, Y.; Louie, M. W.; Trotochaud, L.; Bell, A. T., Effects of Fe Electrolyte Impurities on Ni(OH)2/NiOOH Structure and Oxygen Evolution Activity. *J. Phys. Chem. C* **2015,** *119* (13), 7243-7254.

186.Ren, J. T.; Yuan, G. G.; Weng, C. C.; Chen, L.; Yuan, Z. Y., Uniquely Integrated Fe-Doped Ni(OH)2 Nanosheets for Highly Efficient Oxygen and Hydrogen Evolution Reactions. *Nanoscale* **2018,** *10* (22), 10620-10628.

187.Kresse, G.; Hafner, J., Ab Initio Molecular Dynamics For Liquid Metals. *Phys. Rev. B Condens. Matter.* **1993,** *47* (1), 558-561.

188.Kresse, G.; Hafner, J., Ab Initio Molecular-Dynamics Simulation of the Liquid-Metal-Amorphous-Semiconductor Transition in Germanium. *Phys. Rev. B* **1994,** *49* (20), 14251-14269.

189.Kresse, G.; Furthmüller, J., Efficiency of Ab-Initio Total Energy Calculations for Metals and Semiconductors Using a Plane-Wave Basis Set. *Comput. Mater. Sci.* **1996,** *6* (1), 15-50.

190.Perdew, J. P.; Burke, K.; Ernzerhof, M., Generalized Gradient Approximation Made Simple. *Phys. Rev. Lett.* **1996,** *77* (18), 3865-3868.

191.Blochl, P. E., Projector Augmented-Wave Method. *Phys. Rev. B Condens. Matter.* **1994,** *50* (24), 17953-17979.

192.Vanderbilt, D., Soft Self-Consistent Pseudopotentials in a Generalized Eigenvalue Formalism. *Phys. Rev. B* **1990,** *41* (11), 7892-7895.

193.Ellis, J. E.; Star, A., Carbon nanotube based gas sensors toward breath analysis. *ChemPlusChem* **2016,** *81* (12), 1248.

194.Weis, J. G.; Ravnsbæk, J. B.; Mirica, K. A.; Swager, T. M., Employing halogen bonding interactions in chemiresistive gas sensors. *ACS Sensors* **2016,** *1* (2), 115-119.

195.Park, C. H.; Schroeder, V.; Kim, B. J.; Swager, T. M., Ionic liquid-carbon nanotube sensor arrays for human breath related volatile organic compounds. *ACS sensors* **2018,** *3* (11), 2432-2437.

196.Lapointe, F.; Ding, J.; Lefebvre, J., Carbon Nanotube Transistors as Gas Sensors: Response Differentiation Using Polymer Gate Dielectrics. *ACS Applied Polymer Materials* **2019**.

197.Hwang, S. I.; Franconi, N. G.; Rothfuss, M. A.; Bocan, K. N.; Bian, L.; White, D. L.; Burkert, S. C.; Euler, R. W.; Sopher, B. J.; Vinay, M. L., Tetrahydrocannabinol detection using semiconductor-enriched single-walled carbon nanotube chemiresistors. *ACS sensors* **2019,** *4* (8), 2084-2093.

198.Chen, Y.; Mun, S. C.; Kim, J., A wide range conductometric pH sensor made with titanium dioxide/multiwall carbon nanotube/cellulose hybrid nanocomposite. *IEEE Sensors Journal* **2013,** *13* (11), 4157-4162.

199.Li, C. A.; Han, K. N.; Pham, X.-H.; Seong, G. H., A single-walled carbon nanotube thin film-based pH-sensing microfluidic chip. *Analyst* **2014,** *139* (8), 2011-2015.

200.Gou, P.; Kraut, N. D.; Feigel, I. M.; Bai, H.; Morgan, G. J.; Chen, Y.; Tang, Y.; Bocan, K.; Stachel, J.; Berger, L., Carbon nanotube chemiresistor for wireless pH sensing. *Scientific reports* **2014,** *4* (1), 1-6.

201.Kaempgen, M.; Roth, S., Transparent and flexible carbon nanotube/polyaniline pH sensors. *Journal of Electroanalytical Chemistry* **2006,** *586* (1), 72-76.

202.Morton, J.; Havens, N.; Mugweru, A.; Wanekaya, A. K., Detection of trace heavy metal ions using carbon nanotube-modified electrodes. *Electroanalysis: An International Journal Devoted to Fundamental and Practical Aspects of Electroanalysis* **2009,** *21* (14), 1597-1603.

203.Tung, N. T.; Tue, P. T.; Lien, T. T. N.; Ohno, Y.; Maehashi, K.; Matsumoto, K.; Nishigaki, K.; Biyani, M.; Takamura, Y., Peptide aptamer-modified single-walled carbon nanotube-based transistors for high-performance biosensors. *Scientific reports* **2017,** *7* (1), 1-9.

204.Sun, Y.; Peng, Z.; Li, H.; Wang, Z.; Mu, Y.; Zhang, G.; Chen, S.; Liu, S.; Wang, G.; Liu, C., Suspended CNT-Based FET sensor for ultrasensitive and label-free detection of DNA hybridization. *Biosensors and Bioelectronics* **2019,** *137*, 255-262.

205.Viswanathan, S.; Wu, L.-c.; Huang, M.-R.; Ho, J.-a. A., Electrochemical immunosensor for cholera toxin using liposomes and poly (3, 4-ethylenedioxythiophene)-coated carbon nanotubes. *Analytical Chemistry* **2006,** *78* (4), 1115-1121.

206.Sharf, T.; Wang, N.-P.; Kevek, J. W.; Brown, M. A.; Wilson, H.; Heinze, S.; Minot, E. D., Single electron charge sensitivity of liquid-gated carbon nanotube transistors. *Nano letters* **2014,** *14* (9), 4925-4930.

207.Kong, J.; Franklin, N. R.; Zhou, C.; Chapline, M. G.; Peng, S.; Cho, K.; Dai, H., Nanotube molecular wires as chemical sensors. *science* **2000,** *287* (5453), 622-625.

208.Puchades, I.; Lawlor, C. C.; Schauerman, C. M.; Bucossi, A. R.; Rossi, J. E.; Cox, N. D.; Landi, B. J., Mechanism of chemical doping in electronic-type-separated single wall carbon nanotubes towards high electrical conductivity. *Journal of Materials Chemistry C* **2015,** *3* (39), 10256-10266.

209.Kaskela, A.; Nasibulin, A. G.; Timmermans, M. Y.; Aitchison, B.; Papadimitratos, A.; Tian, Y.; Zhu, Z.; Jiang, H.; Brown, D. P.; Zakhidov, A., Aerosol-synthesized SWCNT networks with tunable conductivity and transparency by a dry transfer technique. *Nano letters* **2010,** *10* (11), 4349-4355.

210.Yoon, I.; Eom, G.; Lee, S.; Kim, B. K.; Kim, S. K.; Lee, H. J., A Capacitive Micromachined Ultrasonic Transducer-Based Resonant Sensor Array for Portable Volatile Organic Compound Detection with Wireless Systems. *Sensors* **2019,** *19* (6), 1401.

211.Ouyang, M.; Huang, J.-L.; Lieber, C. M., Fundamental electronic properties and applications of single-walled carbon nanotubes. *Accounts of chemical research* **2002,** *35* (12), 1018-1025.

212.Bekyarova, E.; Itkis, M. E.; Cabrera, N.; Zhao, B.; Yu, A.; Gao, J.; Haddon, R. C., Electronic properties of single-walled carbon nanotube networks. *Journal of the American Chemical Society* **2005,** *127* (16), 5990-5995.

213.Wang, F.; Swager, T. M., Diverse chemiresistors based upon covalently modified multiwalled carbon nanotubes. *Journal of the American Chemical Society* **2011,** *133* (29), 11181-11193.

214.Huang, J.; Ng, A. L.; Piao, Y.; Chen, C.-F.; Green, A. A.; Sun, C.-F.; Hersam, M. C.; Lee, C. S.; Wang, Y., Covalently functionalized double-walled carbon nanotubes combine high sensitivity and selectivity in the electrical detection of small molecules. *Journal of the American Chemical Society* **2013,** *135* (6), 2306-2312.

215.Steuerman, D. W.; Star, A.; Narizzano, R.; Choi, H.; Ries, R. S.; Nicolini, C.; Stoddart, J. F.; Heath, J. R., Interactions between conjugated polymers and single-walled carbon nanotubes. *The Journal of Physical Chemistry B* **2002,** *106* (12), 3124-3130.

216.Tang, B. Z.; Xu, H., Preparation, alignment, and optical properties of soluble poly (phenylacetylene)-wrapped carbon nanotubes. *Macromolecules* **1999,** *32* (8), 2569-2576.

217.Ellis, J. E.; Zeng, Z.; Hwang, S. I.; Li, S.; Luo, T.-Y.; Burkert, S. C.; White, D. L.; Rosi, N. L.; Gassensmith, J. J.; Star, A., Growth of ZIF-8 on molecularly ordered 2-methylimidazole/single-walled carbon nanotubes to form highly porous, electrically conductive composites. *Chemical science* **2019,** *10* (3), 737-742.

218.Day, R. W.; Bediako, D. K.; Rezaee, M.; Parent, L. R.; Skorupskii, G.; Arguilla, M. Q.; Hendon, C. H.; Stassen, I.; Gianneschi, N. C.; Kim, P.; Dincă, M., Single Crystals of Electrically Conductive Two-Dimensional Metal–Organic Frameworks: Structural and Electrical Transport Properties. *ACS Central Science* **2019,** *5* (12), 1959-1964.

219.Hmadeh, M.; Lu, Z.; Liu, Z.; Gándara, F.; Furukawa, H.; Wan, S.; Augustyn, V.; Chang, R.; Liao, L.; Zhou, F.; Perre, E.; Ozolins, V.; Suenaga, K.; Duan, X.; Dunn, B.; Yamamto, Y.; Terasaki, O.; Yaghi, O. M., New Porous Crystals of Extended Metal-Catecholates. *Chemistry of Materials* **2012,** *24* (18), 3511-3513.

220.Xie, L. S.; Skorupskii, G.; Dincă, M., Electrically Conductive Metal–Organic Frameworks. *Chemical Reviews* **2020,** *120* (16), 8536-8580.

221.Hinckley, A. C.; Park, J.; Gomes, J.; Carlson, E.; Bao, Z., Air-Stability and Carrier Type in Conductive M3(Hexaaminobenzene)2, (M = Co, Ni, Cu). *Journal of the American Chemical Society* **2020,** *142* (25), 11123-11130.

222.Ko, M.; Mendecki, L.; Eagleton, A. M.; Durbin, C. G.; Stolz, R. M.; Meng, Z.; Mirica, K. A., Employing Conductive Metal–Organic Frameworks for Voltammetric Detection of Neurochemicals. *Journal of the American Chemical Society* **2020,** *142* (27), 11717-11733.

223.Mähringer, A.; Jakowetz, A. C.; Rotter, J. M.; Bohn, B. J.; Stolarczyk, J. K.; Feldmann, J.; Bein, T.; Medina, D. D., Oriented Thin Films of Electroactive Triphenylene Catecholate-Based Two-Dimensional Metal–Organic Frameworks. *ACS Nano* **2019,** *13* (6), 6711-6719.

224.Li, W. H.; Ding, K.; Tian, H. R.; Yao, M. S.; Nath, B.; Deng, W. H.; Wang, Y.; Xu, G., Conductive metal–organic framework nanowire array electrodes for high-performance solid-state supercapacitors. *Advanced Functional Materials* **2017,** *27* (27), 1702067.

225.Furtado, C. A.; Kim, U. J.; Gutierrez, H. R.; Pan, L.; Dickey, E. C.; Eklund, P. C., Debundling and dissolution of single-walled carbon nanotubes in amide solvents. *Journal of the American Chemical Society* **2004,** *126* (19), 6095-6105.

226.Sarker, B. K.; Shekhar, S.; Khondaker, S. I., Semiconducting enriched carbon nanotube aligned arrays of tunable density and their electrical transport properties. *ACS nano* **2011,** *5* (8), 6297-6305.

227.Dresselhaus, M. S.; Dresselhaus, G.; Saito, R.; Jorio, A., Raman spectroscopy of carbon nanotubes. *Physics reports* **2005,** *409* (2), 47-99.

228.Sasaki, K.-i.; Saito, R.; Dresselhaus, G.; Dresselhaus, M. S.; Farhat, H.; Kong, J., Chirality-dependent frequency shift of radial breathing mode in metallic carbon nanotubes. *Physical Review B* **2008,** *78* (23), 235405.

229.Rubio-Giménez, V.; Galbiati, M.; Castells-Gil, J.; Almora-Barrios, N.; Navarro-Sánchez, J.; Escorcia-Ariza, G.; Mattera, M.; Arnold, T.; Rawle, J.; Tatay, S., Bottom-Up Fabrication of Semiconductive Metal–Organic Framework Ultrathin Films. *Advanced materials* **2018,** *30* (10), 1704291.

230.Walton, K. S.; Snurr, R. Q., Applicability of the BET method for determining surface areas of microporous metal− organic frameworks. *Journal of the American Chemical Society* **2007,** *129* (27), 8552-8556.

231.Chun, K.-Y.; Oh, Y.; Rho, J.; Ahn, J.-H.; Kim, Y.-J.; Choi, H. R.; Baik, S., Highly conductive, printable and stretchable composite films of carbon nanotubes and silver. *Nature nanotechnology* **2010,** *5* (12), 853-857.

232.Lerner, M. B.; Resczenski, J. M.; Amin, A.; Johnson, R. R.; Goldsmith, J. I.; Johnson, A. T. C., Toward quantifying the electrostatic transduction mechanism in carbon nanotube molecular sensors. *Journal of the American Chemical Society* **2012,** *134* (35), 14318-14321.

233.Heller, I.; Chatoor, S.; Männik, J.; Zevenbergen, M. A. G.; Dekker, C.; Lemay, S. G., Influence of electrolyte composition on liquid-gated carbon nanotube and graphene transistors. *Journal of the American Chemical Society* **2010,** *132* (48), 17149-17156.